DEVELOPMENT OF TiAl-BASED ALLOYS USING SUSPENDED DROPLET ALLOYING

UNIVERSITY OF BIRMINGHAM

By

SHICHAO LIU

A thesis submitted to the

University of Birmingham

For the degree of

DOCTOR OF PHILOSOPHY

Department of Metallurgy and Materials

University of Birmingham

April 2017

ABSTRACT

In this project a novel combinatorial synthesis method, Suspended Droplet Alloying (SDA), has been developed for the rapid production of small, bulk alloy samples for the large EU FP7 collaborative project, Accelerated Metallurgy. SDA can produce a discrete mm-sized fully dense alloy button with precise stoichiometry in several minutes. Samples of many different alloy systems have been produced by SDA but this thesis will only present work on the Ti-Al-V, Ti-Al-Fe and Ti-Al-Nb alloy systems. Ti-Al-Nb alloy samples are difficult to make due to the high melting point of Nb, so the SDA process parameters have been optimized in order to make homogeneous Ti-Al-Nb alloys. The fundamentals of the SDA process have been studied in terms of the formation of the droplets and the consistency of the process. Splats deposited by the impact of individual alloy droplets have also been investigated. Finally, SDA has been used to explore the influence of a fourth elemental addition to a Ti-46Al-8Nb alloy. The elements added are V, Hf, Cr and Zr. It has been found that the addition of V can increase the ductility of Ti-46Al-8Nb alloy significantly.

ACKNOWLEDGEMENT

I would like to give my deep appreciation to my supervisors Prof. Moataz Attallah and Dr. Nicholas Adkins, for their professional guidance and kind support through my whole PhD life. I also want to give my genuine thanks to them for the encouragement during my thesis writing.

I also would like to thank Dr. Stephen McCain, Dr. Bastian Hauptstein and Dr. Sheng Li for their help in my project. I appreciated everything they have taught to me. Their creative and energetic research spirit is what I should learn.

My thanks is also given to Dr. David Hu who provide me with the as-casted Ti-46Al-8Nb sample and shared his knowledge about TiAl-based alloys; Mr. Mike Glynn for helping me to HIP the samples; Dr. David Crudden and Mr. Sabin Sulzer from University of Oxford for their help on my ETMT tests; Dr. Mark Ward for lending me the high speed camera and teaching me how to use it; Dr. Noriko Read and Miss Xiqian Wang for their encouragement when I needed it; and all other group members for their help and support in the lab.

I would also like to give my special thanks to my roommates Dr. Minshi Wang and Miss Xinyu Lv for being the best roommates.

In the end, I want to give my deepest thanks to my parents. Their strong and warm support is what makes me carry on.

CONTENTS

CHAPTER 1: INTRODUCTION

1.1. General Introduction

This project is derived from a European project, Accelerated Metallurgy (AccMet). The AccMet project is applying novel combinatorial synthesis techniques to fabricate thousands of samples with unexplored alloy formulations, and test all these samples with a series of high throughput tests, and build up a “Virtual Alloy Library” with all the alloys’ data. The novel combinatorial synthesis technique named as “Suspended Droplet Alloying” (SDA) is based on direct laser fabrication (DLF). Several TiAl-based alloy systems were made using SDA such as Ti-Al-(Fe, V, Nb) and SDA process has been investigated and optimised based on Ti-Al-Nb alloys. Moreover, Ti-Al-Nb alloys with fourth addition elements were made by SDA and investigated. The Accelerated Metallurgy Project and Suspended Droplet Alloying are introduced in this chapter. The aims and objectives of the research were listed at the end.

1.2. Accelerated Metallurgy

AccMet is an EU FP7 project that can be regarded as a Materials Genome project in Europe. The full title of the project is “The Accelerated Discovery of Alloy Formulations using Combinatorial Principles”. The core concept of this project is to deliver an integrated pilot-scale facility for the combinatorial synthesis and the testing of many thousands of unexplored alloy formulations. SDA is a unique combinatorial synthesis method developed for this project. It allows making discrete mm-sized fully-dense alloy button with precise stoichiometry, so that more tests can be operated without the limitation of sample's size. SDA synthesizes large numbers of compositionally-varying alloy samples, and then submits them to high-throughput testing of their structures and properties like superconducting tests and thermoelectric tests. The vast amount of information is recorded in a "Virtual Alloy Library". The most promising alloy formulations among the database will be further explored. The industrial interests for the alloy exploration are mainly focused on 6 directions: (SINTEF. ACCMET. 2011)

- New lightweight fuel-saving alloys (<4.5 g/cm3) for aerospace and automotive applications.
- New higher-temperature alloys (stable>1000 °C) for rockets, gas turbines, jet-engines, nuclear fusion.
- New high-Tc superconductor alloys (>30K) that can be wire-drawn for electrical applications.
- New high-ZT thermoelectric alloys for converting waste heat directly into electricity.
- New magnetic and magnetocaloric alloys for motors and refrigeration.
- New phase-change alloys for high-density memory storage.

AccMet is a large-scale integrating collaborative project. The AccMet has 29 partners, and among them 14 partners are companies like Rolls Royce Plc, Norsk Titanium Components AS, etc. This project is also supported by 9 academic partners (Cardiff University, The University of Sheffield, The University of Cambridge, The University of Birmingham, Universita Degli Studi di Torino, Universite de Rouen Normandie, Technical University of Denmark, Universitaet ULM and Monash University) and 5 experienced research organizations such as Stiftelsen SINTEF, Flamac and others (SINTEF. ACCMET. 2011).

The AccMet project was started in June 2011 and ended in June 2016. With the collaborative works of these partners, thousands of samples were made and examined with a serial high throughput tests. The “Virtual Alloy Library” including all the information of AccMet alloy samples has been established. Progresses on many different alloy formulations have been made (García-Cañadas and Min 2014, Cornide, Calvo-Dahlborg et al. 2015, Jasiewicz, Cieslak et al. 2015, García-Cañadas, Adkins et al. 2016, Mackie, Hatton et al. 2016).

1.3. Suspended Droplet Alloying

SDA is a novel combinatorial synthesis technique developed for AccMet which was patented in May 2012 (PCT/EP2012/059895). It allows making discrete mm-sized fully-dense alloy button with precise stoichiometry in several minutes. The traditional methodology for alloy development takes over 5 years to find one alloy formulation which offers an appropriate balance of properties for a particular application. SDA is more time-efficient and cost saving method compared to these traditional alloy exploration methods. Moreover, unlike other combinatorial methods like thin film deposition and diffusion multiples, which only provides thin layers with 5-15 μm to be tested, SDA samples can be applied on more tests without the extreme limitation of sample’s size.

SDA is developed based on direct laser fabrication. DLF is a laser-based addictive manufacturing process which is a way to fabricate net shape metallic parts. DLF generally use metallic powder as their feedstock. Premixed metallic powder is fed toward a central spot by nozzles with the help of inert gas flow. The metallic powder in the central spot will be melted by the laser beam and form a melting pool. The deposition of the powder is defined by CAD files, and it controls the movement of the central spot (the movement of the nozzles or substrate). With the movement of the melting pool, a layer of deposition can be formed. With the overlay of the deposition layers, a net shape 3-D component can be build up. Compared to DLF, SDA replaces the powder feedstock into wire feedstock and cancels the movement of the substrate (X-Y plane) so the samples can only be build up along the Z-axis. The powder-feed system is abandoned because SDA need to make samples rapidly with target compositions and the powder-feed system cannot satisfy this requirement. The comparison between wire-feed system and powder-feed system is shown below in Table 1.1.

Table 1.1 The comparison between wire-feed system and powder-feed system

DLF powder-feed system	SDA wire-feed system
Waste of materials (usually 10-50% of the powder does not end up in the samples)	100% of the materials can be fed into the melting pool
Extra effort required to manage the oversprayed powder	Environmental friendly
Complicate system	Simple system
Expensive raw materials	Cheaper wires
Wide range of elemental powder available	Limited range of wire compositions available

Since the feed system is changed into wires completely, the formation of the melting pool is also changed in order to guarantee the wires are melted and deposited into the melting pool properly. According to my previous research as an undergraduate student, it is found that wires cannot melt properly if it feed into the melting pool directly. Therefore, the wires will be melted by the laser beam at the end of the wires above the melting pool. The wires hold an alloyed droplet, and the wires will feed into it and get mixed. Then the alloyed droplets will fell into the meting pool directly. The melting pool is fixed in the centre and raised up as the alloyed droplets keep falling into it. The alloyed metal buttons are built up like this. More details of the SDA process will be demonstrated in this thesis.

1.4. Project Aims, Objectives & Approach

The aim of this project is to develop the SDA process to make samples rapidly and successfully and use SDA to explore TiAl-based alloys.

The objectives of the project are:

- Validate the SDA technique as a promising combinatorial synthesis method to make AccMet samples.
- Understand the influence of the SDA process parameters and produce homogeneous Ti-Al-Nb AccMet samples.
- Investigate the influence of the addition of fourth element in Ti-Al-Nb alloys

As the project moved along, a new type of the AccMet sample was developed which is a splat formed with the deposition of a single alloyed droplet.

Ti-Al-V, Ti-Al-Fe and Ti-Al-Nb ternary alloy systems made by SDA were examined in terms of compositions and microstructure to check the homogeneity of these samples. The performance of these samples indicates the potential of SDA technique. A microscope camera and a high speed camera were used during the fabrication of AccMet samples to study the SDA process. The additions of V, Hf, Co, Zr based on Ti-46Al-8Nb were studied to explore the influence of the fourth element on Ti-Al-Nb alloys.

1.5. References

SINTEF. ACCMET. 2011 [Online]. Available: https://www.sintef.no/en/projects/accmet-accelerated-metallurgy-the-accelerated-disc/

Cornide, J., et al. (2015). "Combined atom probe tomography and TEM investigations of CoCrFeNi, CoCrFeNi-Pdx (x= 0.5, 1.0, 1.5) and CoCrFeNi-Sn." Acta Physica Polonica A **128**(4): 557-560.

García-Cañadas, J., et al. (2016). "Accelerated discovery of thermoelectric materials: combinatorial facility and high-throughput measurement of thermoelectric power factor." ACS combinatorial science **18**(6): 314-319.

García-Cañadas, J. and G. Min (2014). "Multifunctional probes for high-throughput measurement of Seebeck coefficient and electrical conductivity at room temperature." Review of Scientific Instruments **85**(4): 043906.

Jasiewicz, K., et al. (2015). "Relative crystal stability of Al x FeNiCrCo high entropy alloys from XRD analysis and formation energy calculation." Journal of Alloys and Compounds **648**: 307-312.

Mackie, A. J., et al. (2016). "Carbon uptake and distribution in spark plasma sintering (SPS) processed Sm (Co, Fe, Cu, Zr) z." Materials Letters **171**: 14-17.

CHAPTER 2: LITERATURE REVIEW

The Accelerate Metallurgy project is mainly focused on alloy exploration. Since the traditional methodology for alloy development is time-consuming, combinatorial methods are widely used for alloy development at present. This review provides a brief introduction about combinatorial methods and the alloy development works applied different combinatorial synthesises.

Unlike other combinatorial synthesises, the novel technique applied in this project is based on Direct Laser Deposition. DLD is a manufacturing technique that allows the fabrication of 3-D near net shape and fully dense components from metal powders. A simple background of DLD is presented in the review. Also, the process parameters that influence the products are covered in this review.

In the thesis, the new combinatorial synthesis method is used to study TiAl-based alloys. Therefore, a review of TiAl-based alloys is provided. The phases in the alloys, the performance and applications of the TiAl alloy are included in this review. Different element's influences on the TiAl alloys are also studied. Moreover, since a part of the works in the project is based on the commercial TiAl alloy Ti-46Al-8Nb, an introduction to this alloy is also presented.

2.1 Combinatorial synthesises

2.1.1 Introduction of combinatorial synthesises

Combinatorial materials science derives from combinatorial chemistry which uses chemical synthetic methods to prepare large number of compounds and identify useful components among these compound libraries. Originally, scientists got this idea from the human body. The human immune system can generate 10^{14} antibodies to fight with virus invasions. These antibodies are screened and the specific antibody is found to react with the correspondent virus so the virus become a harmless compound (Xiang 1999).

Combinatorial chemistry has been widely developed since the 1990s, and is based on the synthetic approach to polypeptide selection investigated by Merrifield in the 1960s (Merrifield 1963). In combinatorial chemistry, firstly a very large number of compounds are prepared by different synthetic methods like one-bead one-compound combinatorial library method and parallel synthesis (Fenniri 2000). The collections of synthesised compounds are called libraries, and then the useful components are identified among these libraries. Combinatorial chemistry has become a valuable tool in drug discovery and optimization (Gallop, Barrett et al. 1994, Gordon, Barrett et al. 1994), and increasingly combinatorial methods are being applied to material science.

Combinatorial materials science consists of three important aspects: systematic synthesis to prepare libraries, high-throughput screening for properties (characterization) and data storage and analysis (computational tool) (Maier, Stöwe et al. 2007). Unlike combinatorial chemistry's development which is based on molecular structure and their variation, combinatorial material science's development is depend on materials composition, process parameters and characterization methods. All these parts rely on novel techniques and equipment. Metallurgists actually started to explore combinatorial synthesis in the late 1960s (Hanak 1970), however it was limited by the equipment at that time, and the research stopped and restarted in the 1990s (Xiang and Takeuchi 2003). It is therefore a relatively new field that uses combinatorial methods to identify important new materials for use in engineering applications. The technique has been applied for shape-memory alloys (Famodu, Hattrick-Simpers et al. 2004), superconductors (Xiang, Sun et al. 1995), electrodes (Fleischauer, Topple et al. 2005), catalyst (Potyrailo 2004), and many other fields.

Combinatorial methods not only are useful in discovering new alloys but also optimizing existing alloys. Because of the time and expense of qualifying engineering materials, the industrial approach is often to modify existing alloys to improve their properties rather than to develop new alloys (Pharr, George et al. 2005).

2.1.2 Different combinatorial synthesises applied on materials development

i. Thin film deposition

Thin film with continuous composition spreads can be produced using different techniques like pulsed-laser deposition, magnetron sputtering and electron beam evaporation. Thin film deposition can be divided into two types depending on the need for post-annealing.

For the thin films made by co-sputtering in a magnetron sputtering system there is no need for post-deposition annealing, because the alloying is taken place automatically during the film deposition. The alloy film was deposited onto a 100 mm diameter sapphire substrate using an RF magnetron sputtering system (shown in Figure 2.1). Continuous composition variation in the film is introduced by the varying distance from the sputtering sources to different positions on the substrate. The rapid process generates a pseudoternary phase diagram on the film, thus making this approach access to a variety of non-equilibrium phases with unique structures and properties. However the disadvantage of the technique is only a limited range of the ternary composition can be explored in one thin film because of the geometric restriction of the sputtering system (Pharr, George et al. 2005, Maier, Stöwe et al. 2007). E.D. Specht used this technique to study nonequilibrium structures in Cr-Fe-Ni films (Specht, Rack et al. 2003).

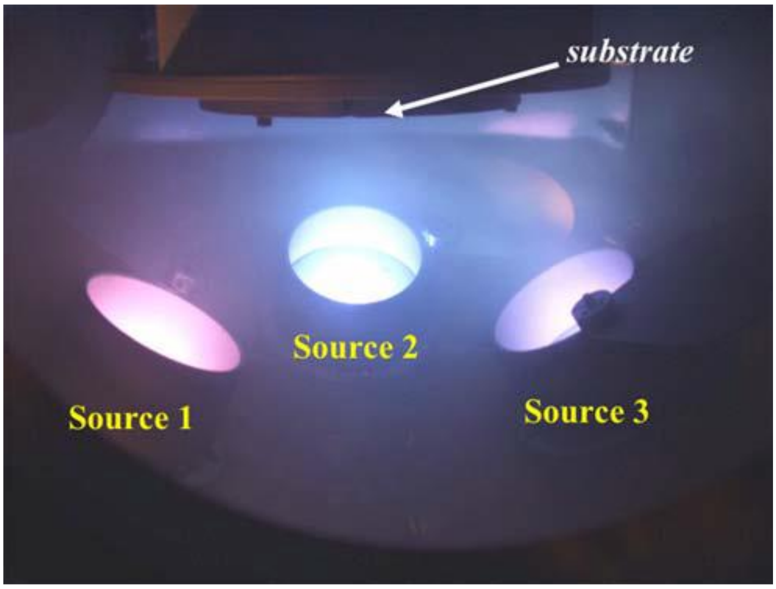

Figure 2.1 Three-source Fe-Cr-Ni sputter deposition system. Each source was 51-mm-diam, and the sources centers were 16.5 cm from the substrate center and were tilted at 32° relative to the substrat. The iron and nickel sources were 180° apart, with the chromium source 90° from both the iron and the nickel (Specht, Rack et al. 2003).

Another alloy libraries preparation method is based on thin film deposition and interdiffusion. The component materials were deposited onto the substrate as discrete layers and interdiffused together after annealing. The materials were deposited in sequence and the distribution of each component (the thickness of each layer) was controlled by a shutter. The overlay of all the layers can make the film produce a continuous phase diagram. For example, G.M. Pharr used an electron beam evaporation system to deposit Fe-Ni-Cr films. (Figure 2.2) The Fe, Ni and Cr layers were deposited onto the substrate with a thickness gradient created by a sliding shutter. The shutter was moved at a constant rate to make the thickness change linearly in terms of position. The sample was rotated by 120° around the centre after a layer was deposited, and then another component layer was deposited (Pharr, George et al. 2005).

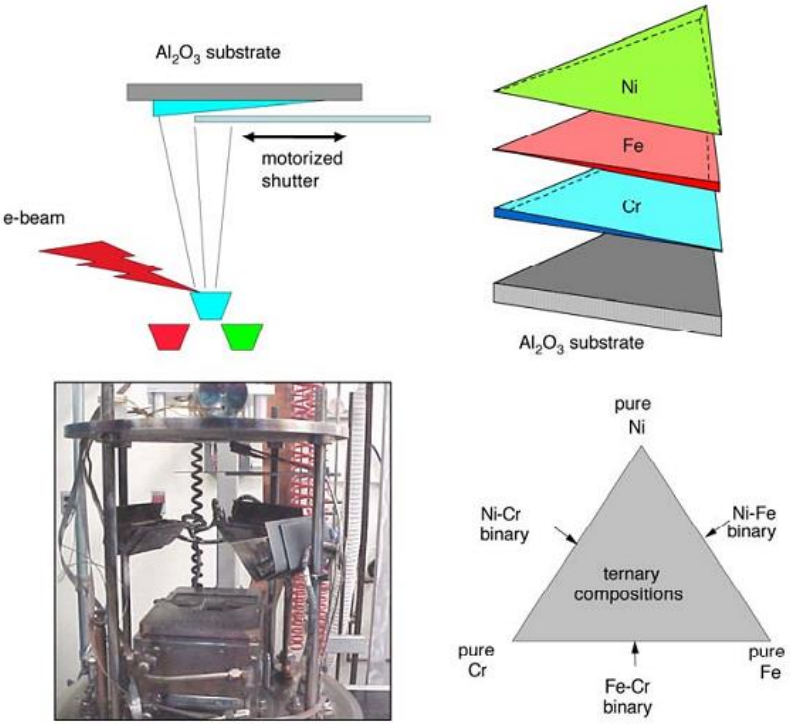

Figure 2.2 A schematic diagram of the deposition process used to make thin film libraries by thin film deposition and annealing (Pharr, George et al. 2005)

After deposition, the layers were interdiffused together by annealing. The annealing time had a huge influence on the roughness and porosity of Fe-Ni-Cr film (shown in Figure 2.3). Compared to the co-deposition method, this approach can cover all possible ternary compositions and match with the ternary phase equilibria (Pharr, George et al. 2005).

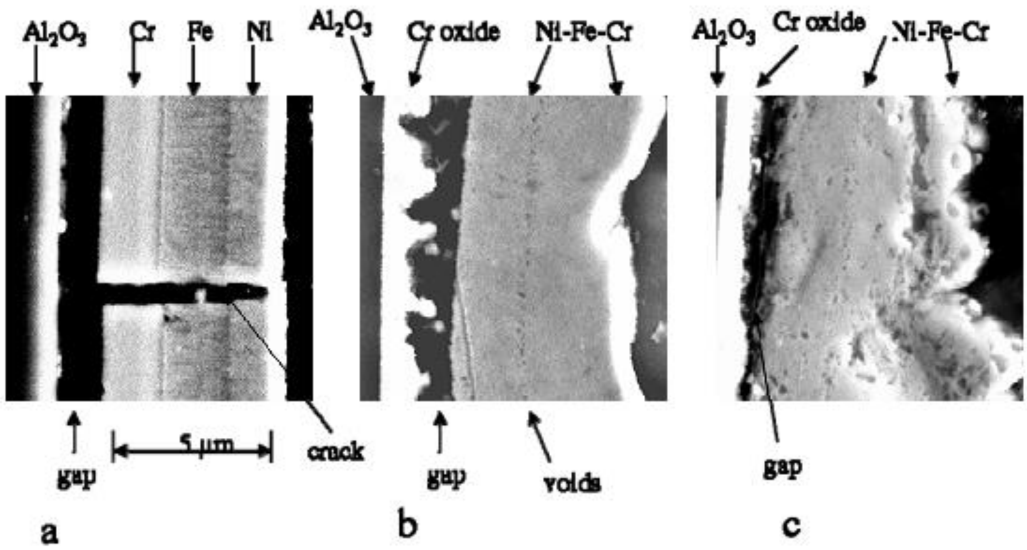

Figure 2.3 Cross-sectional SEM images of Fe-Ni-Cr sample: (a) as deposited; (b) after annealing in vacuum at 825°C for 2 h 10 min; (c) after annealing in vacuum at 19 h 30 min (Pharr, George et al. 2005).

Xiang used a similar approach to make continuous phase diagram and also applied an integrated materials chip approach to study functional materials (Xiang 1999, Xiang 2002, Xiang 2004). For this method, multiple layer deposition and post-annealing were also needed. The main difference was several masks were used instead of the moving shutter. Masks were either physical shadow masks or photolithographic lift-offs, and the different patterns of masks were shown in Figure 2.4. Each mask was used for up to four sequential depositions, and after each deposition the mask was rotated by 90°. This approach can synthesis 4^n different compositions with only 4n deposition steps and n masks.

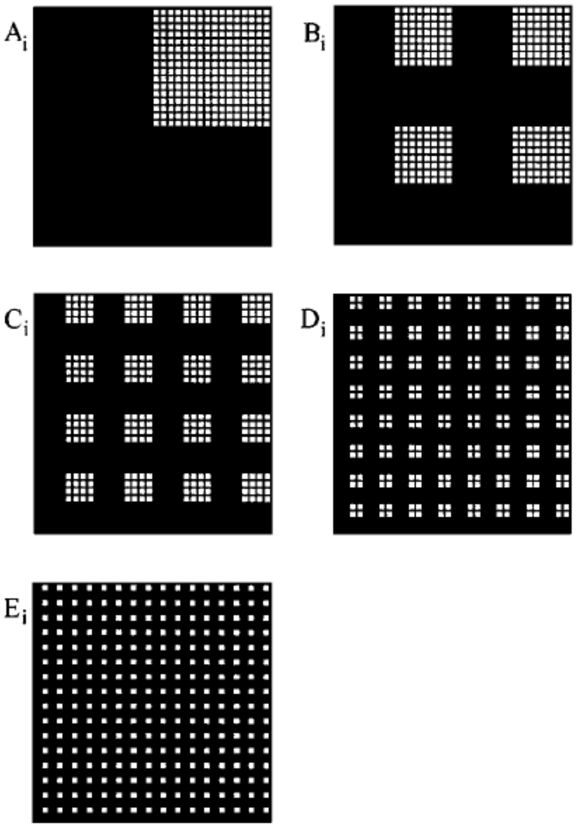

Figure 2.4 Masks for generating the quaternary library: A_i, B_i, C_i, D_i, and E_i represent a deposition step with mask X rotated counterclockwise by (i - 1) × 90° (Xiang 1999)

ii. Diffusion Multiples

The diffusion multiples approach is capable of producing a large number of phases and compositions for efficient mapping of phase diagrams, phase properties and kinetics based on the composition gradients and intermetallic phases created by the long-term annealing of three or more phases/alloys (Zhao 2005). Zhao have developed this method by assembling three or more metal blocks that are contacted with each other at their interface, and subjected to a demanded high temperature to allow thermal interdiffusion to form solid–solution compositions and intermetallic compounds. An example of the Pd-Pt-Rh-Ru-Cr system is shown in Figure 2.5. The diffusion multiple need to be annealed at 1200°C for 40 hours (Zhao 2006).

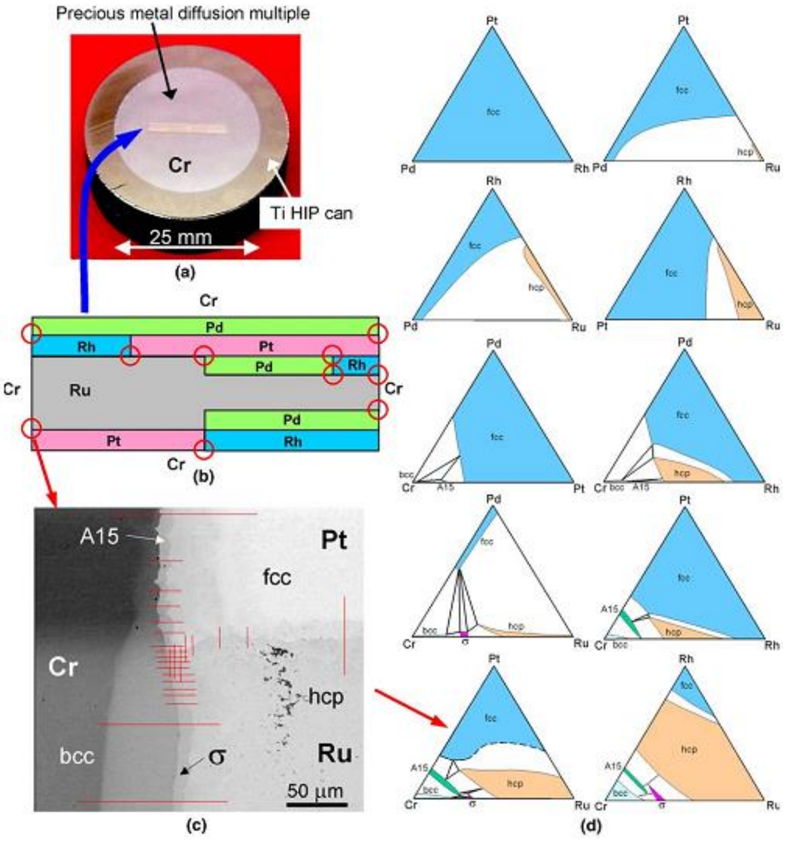

Figure 2.5 A diffusion multiple for rapid mapping of ternary phase diagrams in the Pd–Pt–Rh–Ru–Cr system (Zhao 2006)

Not only phase diagrams, but also diffusion coefficients, precipitation kinetics, and solution-strengthening and precipitation-strengthening effects can be evaluated by this method (Maier, Stöwe et al. 2007). The diffusion multiples approach is summarized in Figure 2.6 (Zhao, Zheng et al. 2005).

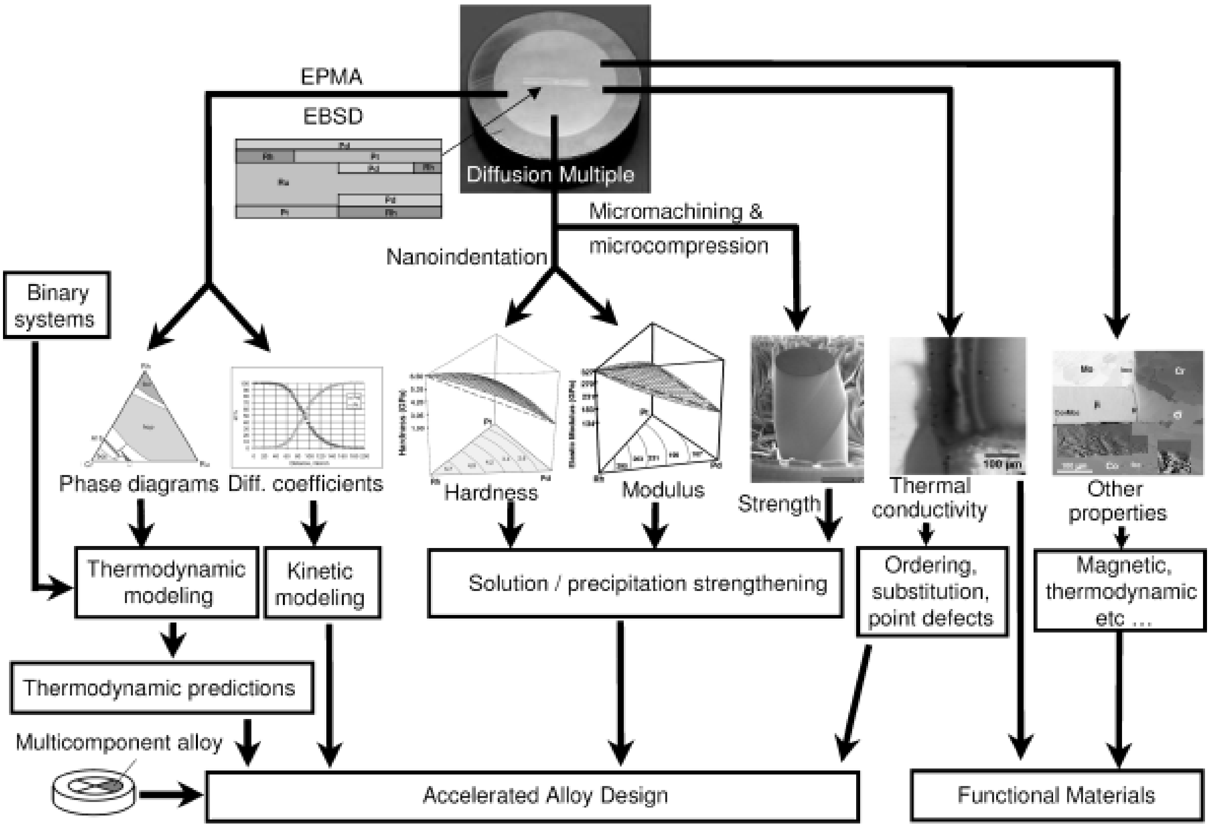

Figure 2.6 Diffusion multiple approach to high-throughput materials research (Zhao 2006)

iii. Electron Beam Melting

G. M. Pharr also tried to prepare the alloy library of binary alloy system Ni-Cr using electron beam melting. As shown in Figure 2.7, the alloy library was prepared by vapor-depositing thin-wedge film of Cr on Ni as substrate, and alloyed by local melting with a focused EB welding system. A compositional gradient can be formed by the EB welding. Unlike high temperature diffusion, this method is more time efficient and the sample it made have a non-equilibrium state that is similar to conventional casting alloys (Pharr, George et al. 2005).

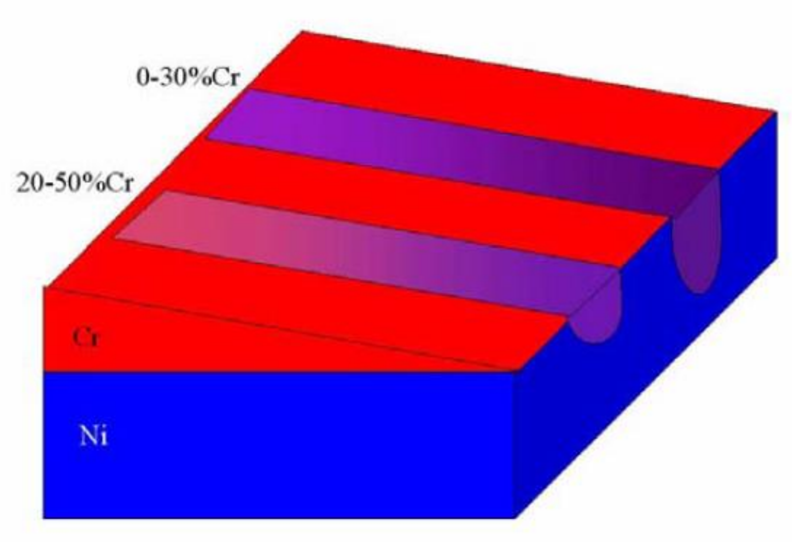

Figure 2.7 Schematic of a Ni-Cr alloy library prepared by Electron Beam Melting (Pharr, George et al. 2005)

Table 2.1 lists the limitations of each combinatorial synthesis method mentioned above, and all of these methods cannot make bulk samples.

Table 2.1 The limitations of combinatorial synthesis methods

Combinatorial synthesis methods	Limitations
Thin film deposition	Some of them need a post heat treatment; limited volume of phases; limited alloy formulations formed at a time
Diffusion multiples	Long-time heat treatment for diffusion; limited volume of phases
Electron Beam Melting	Limited element combinations; limited volume of phases

2.2 Direct Laser Deposition (DLD)

2.2.1 Introduction of DLD

Direct Laser Deposition is a laser-based addictive manufacturing process. It is a way to fabricate net shape metallic parts. Compared to Selective Laser Melting, which has a metal powder bed and the powder is ‘selectively’ melted by laser, In DLD metal powder is directed into a melt pool produced by a focused laser beam (Shamsaei, Yadollahi et al. 2015).The material is deposited to the certain spot directly and formed with the help of a laser beam. DLD has a wide application field. It can be used to build functional graded as well as pure metal parts, and it can also be applied for laser cladding/repair (Pei and De Hosson 2000, Islam, Xue et al. 2001, Traini, Mangano et al. 2008). Due to the great potential of DLD, lots of researches based on DLD have been undertaken (Xue, Chen et al. 2000, Ensz, Griffith et al. 2002, Collins, Banerjee et al. 2003, Kobryn and Semiatin 2003, Wu, Liang et al. 2011). Various DLD technologies have emerged like Direct Metal Deposition (Mazumder, Choi et al. 1997), Direct Light Fabrication (Wu, Liang et al. 2004), and Laser Engineered Net Shaping (Griffith, Keicher et al. 1996). Powder feedstock can be replaced by wire feedstock which increases process efficiency for its better control on the deposition (Wang, Mei et al. 2007). Nozzles in DLD system also developed from single nozzle to multiple nozzles (Jeantette, Keicher et al. 2000). Some common materials that are compatible with the DLD process are investigated: titanium alloys (Wu, Liang et al. 2004, Wang, Mei et al. 2007, Dicks, Wang et al. 2009), steel (Mazumder, Choi et al. 1997), nickel based superalloys (Wu, Liang et al. 2011), cobalt based alloys (Ram, Esplin et al. 2008).

2.2.2 DLD Process

A schematic of DLD system is shown in Figure 2.8. During the process, powder is fed towards the focused laser at a controlled speed and a fixed angle through the nozzles. The high powered laser creates a melting pool on the substrate where the powder is incorporated into the build. The deposition path is defined by a CAD file of a component. This CAD file controls the movement of the positioning table in X-Y plane and the movement of the laser in Z direction. Once the deposition of a single layer is completed, the focused laser and powder feed nozzle move upward along the Z direction with an increment of a layer thickness, and then a new layer will be deposited on the previous layer along CNC controlled path. With the repeat of these deposition steps, metallic parts can be built up.

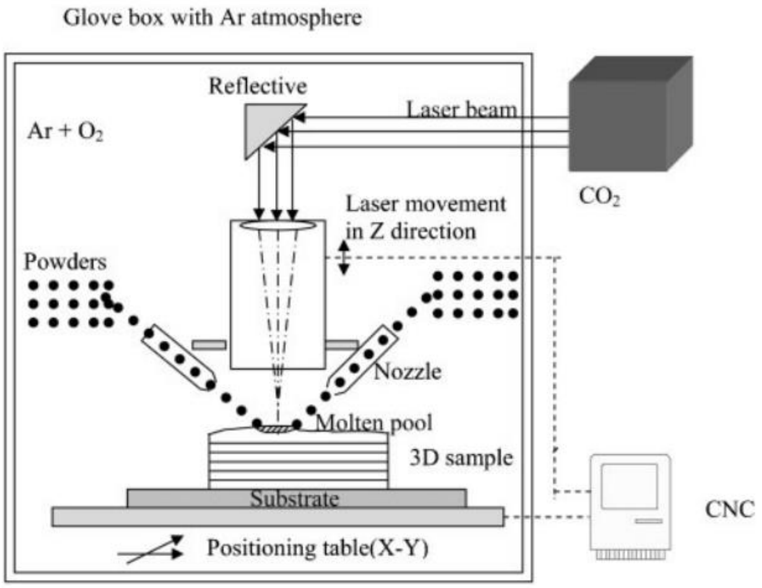

Figure 2.8 A schematic of DLD process (Wu 2007)

2.2.3 DLD Key process variables

DLD has many process parameters that can influence the microstructure and performances of the products, such as: powder feed rate, laser power, laser/substrate relative traverse speed (laser scan speed), laser scanning strategy, and the powder's injection position (laser scanning direction). All these parameters can affect the melting pool and the incident energy, and then change the cooling rate and local thermal gradient which is important to the microstructure of the part produced.

i. Powder feed rate

Powder feed rate can change the deposited mass flow rate which is the distribution of powder density in the melting pool. Generally, a higher powder feed rate is more likely to deposit more materials into the melting pool. The layer thickness generally increases linearly with an increase of powder feed rate (Li, Yang et al. 2003). However build rate is a combination of the powder feed rate and the powder capture efficiency. The powder capture efficiency is never 100% as some powder is not transferred into the melting pool.

ii. Laser power and laser scan speed

Higher laser power and lower laser scan speed lead to a higher incident energy which generally make the product have a coarser microstructure due to lower cooling rates. On the contrary, a decreasing laser power and an increasing laser scan speed result in a higher cooling rate and therefore a finer microstructure can be achieved (Selcuk 2011).

iii. Powder injection point

For a fixed powder feed rate, the amount of powder fed into the melting pool is influenced by the position relationship between powder injection point and laser beam. Figure 2.9 shows the three situations of the position relationship between powder injection point and laser beam. When the powder stream is behind the laser spot, more powder was fed into the melting pool than the other two situations (Li, Yang et al. 2003).

In order to keep a constant deposited mass flow rate, the powder feed rate and laser scanning speed need adjustment according to the scan direction and the distance between laser beam and powder nozzle (Shamsaei, Yadollahi et al. 2015).

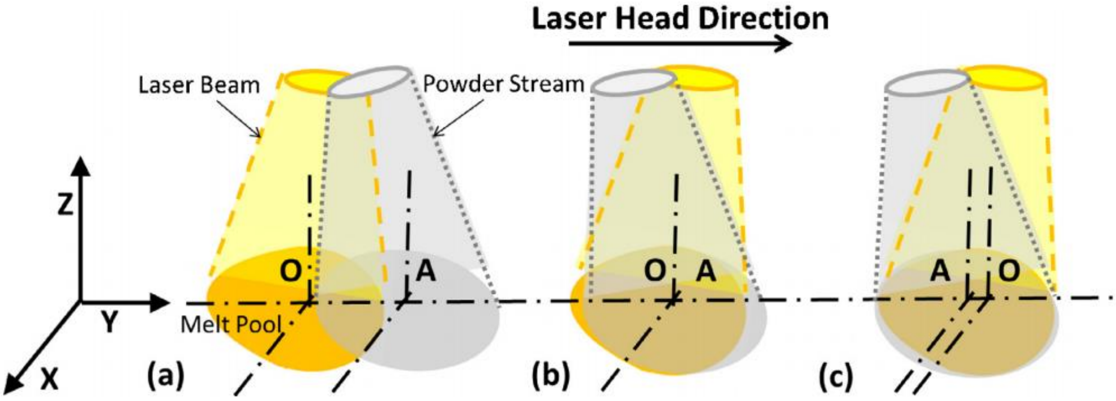

Figure 2.9 The position relationships between powder injection point and laser beam: O is the centre of the laser spot, and A is the centre of powder stream (Shamsaei, Yadollahi et al. 2015)

iv. Deposition pattern

Generally, there are five main laser scanning strategies in Addictive Manufacturing as shown in Figure 2.10 (Dai and Shaw 2002, Yu, Lin et al. 2011). They are raster, bi-directional, offset from the inside to the outside (offset-in), offset from the outside to the inside (offset-out) and fractal. Different laser scanning patterns have significant influence on the geometric and mechanical properties of products. Suitable laser scanning pattern can reduce the residual stress in the products. The raster pattern is most widely used because of its easy mode. The fractal and offset patterns have better geometric accuracy and consume less energy (Shamsaei, Yadollahi et al. 2015). Nickel discovered that fractal and offset-out patterns get the smallest substrate deformations (Nickel, Barnett et al. 2001).

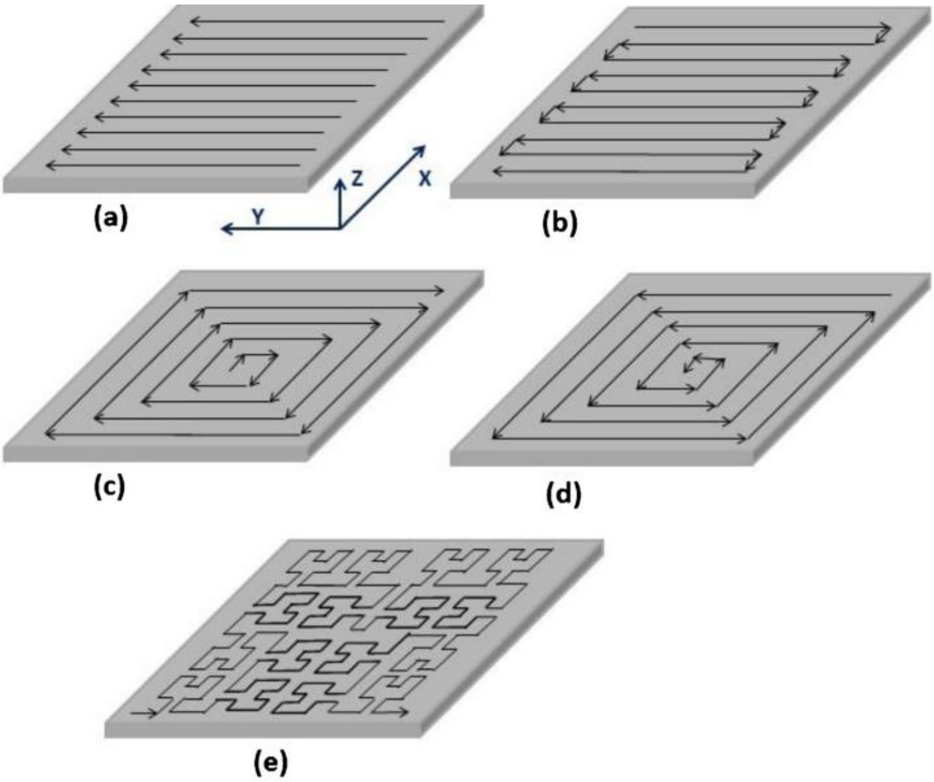

Figure 2.10 Four laser scanning pattern: (a) raster, (b) bi-directional, (c) offset-out, (d) offset-in, and (e) fractal (Dai and Shaw 2002)

2.2.4 Wire feed system

The wire feed system is quite similar to the traditional welding, while the wire adding material is melted by laser beam in the region to be build (Megahed, Mindt et al. 2016). The wire feed system requires more laser power to make fully dense samples than the powder feed system (Wang, Mei et al. 2007). Generally speaking, wire feed system is suitable for high deposition rate processing and have large build volumes. However, the final product made by the wire feed system has a rough surface and needs more post machining than the powder system does (Frazier 2014).

The wire feed system can be also combined with powder system to make compositionally graded samples. Wang used it to make functionally graded samples using a Ti–25V–15Cr–2Al–0.2C powder and a Ti–6Al–4V wire by changing the ratio of powder to wire by varying the powder feed rate while keep a constant wire feed rate (Wang, Mei et al. 2007). With the change of the wire or powder feed rate, the composition of the samples can be changed instantaneously.

2.3 Multiple-wire welding

In submerged arc welding, multiple-wire welding is investigated to increase welding efficiency. It started with twin-wire welding by Ashton in 1954 using twin-electrode (T.Ashton. 1954). In multiple-wire welding, all wires are fed with the same speed simultaneously through a joint contact tube. The wires can be arranged either to be parallel or to be an optional triangle with the regard to the welding direction and merged into the weld pool. This method can increase the deposition rate and productivity, reduce the consumption of shielding flux, and improve arc efficiency (J. Tušek, & M. Suban. 2003).

Despite the multiple arc melding in submerged arc welding, Pickin presented a tandem weld process that can generate different weld element compositions with different aluminium filler wires. Aluminium alloy was used as the base material and binary Al-Cu and Al-Mg were the based filler wires. The composition is determined by the filer wires input parameters, but weld dilution with the base material also need to be considered. In two filler system, Cu alloyed filler's feed rate was constant, and Mg alloyed filler varied to control the Mg content. The Cu content would decrease as the Mg content increases because of the volume dilution (Pickin, et al. 2009). However, in three fillers system, CuSi3 filler was used to control the Cu content. All the filler wires were deposited into the weld pool directly as Figure 2.11 shows. Because almost all the fillers and base material are Al-based alloys, they are easier to get mixed than mixing different elements together. The composition of the weld bead has only around 1 wt. % difference compared to the target composition (Pickin, et al. 2010).

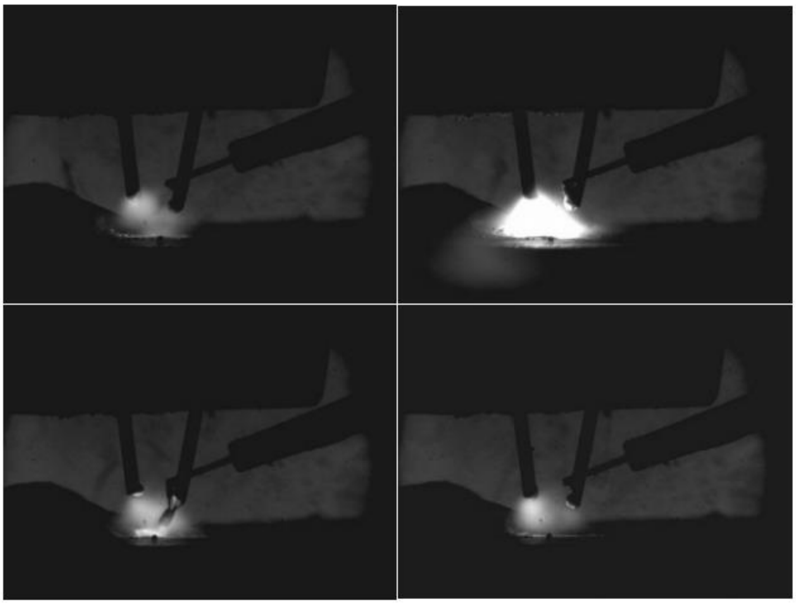

Figure 2.11 High speed images of three wires weld process (Pickin, et al. 2010)

2.4 Metallurgy of TiAl-based alloys

TiAl alloys have many attractive properties such as low density, high temperature strength, high specific strength, high specific stiffness and good oxidation, corrosion resistance. It is regarded as a promising material for automotive applications like turbochargers and valves.

2.4.1 Phases in TiAl-based alloys

Alloying elements in Ti can normally be divided into two types: α or β stabilizers. Some elements increase the α/β transformation temperature of pure Ti and some elements decrease it. Different alloying elements have different effect on phase diagrams of Ti alloys (as shown in Figure 2.12) (Lütjering and Williams 2003).

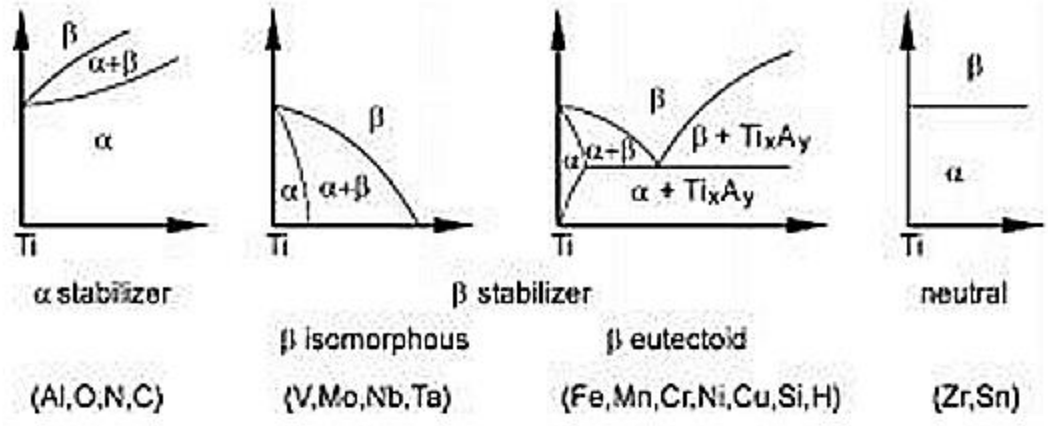

Figure 2.12 Effect of alloying elements on phase diagrams of Ti alloys (Lütjering and Williams 2003)

Al as a strong α stabilizer is the most widely used alloying element in Ti alloys. TiAl based alloys are quite popular and highly developed. TiAl binary phase diagram (Figure 2.13) is the basis for all these TiAl alloys. With the increase of Al content, four intermetallic compounds are formed, which are Ti_3Al (α_2), TiAl (γ), $TiAl_2$ and $TiAl_3$.The first two compounds shows good potential for industrial applications, while the other compounds showing unsatisfactory properties (Djanarthany, Viala et al. 2001).

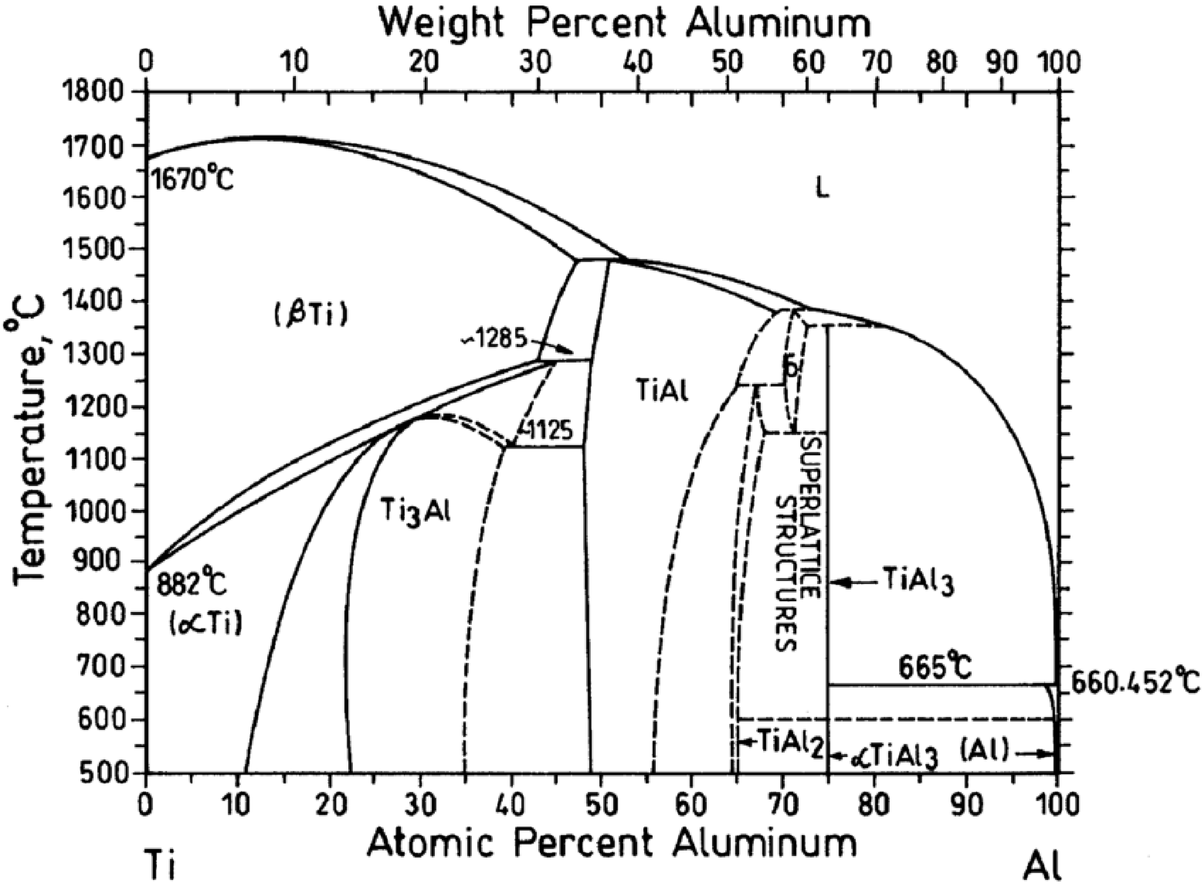

Figure 2.13 Ti-Al binary phase diagram accessed by Murray (Murray 1987)

2.4.2 Properties of TiAl-based alloys

Wu have summarised several properties of TiAl-based alloys and compared with other materials in Figure 2.14 (Wu 2006). Figure 2.14 shows good tensile properties of TiAl-based alloys than Ni-based alloy and steel. However, TiAl-based alloys have a low ductility at room temperature.

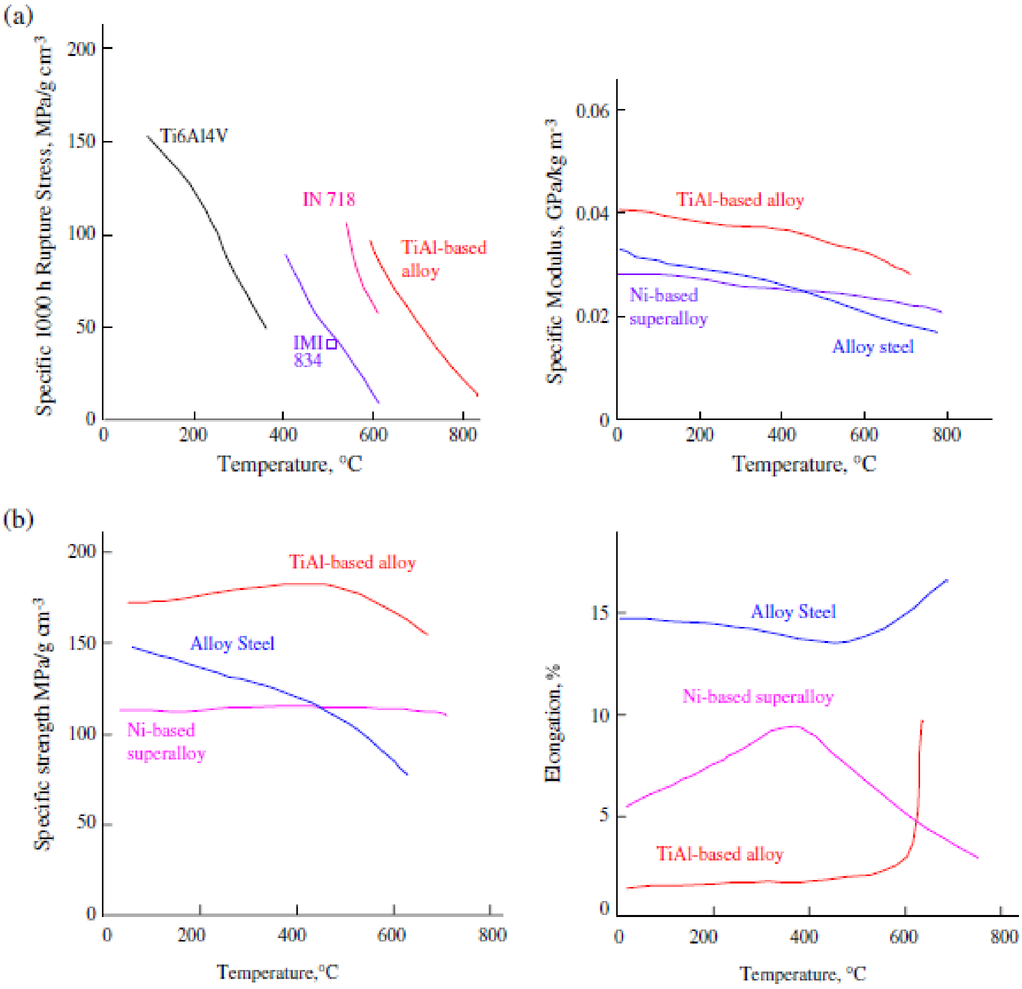

Figure 2.14 (a) 1000 h rupture strength as function of temperature for a TiAl-based alloy, for Ti834, IN 718 and Ti6Al4V and (b) specific strength and ductility as function of temperature for an alloy steel, a Ni-based alloy and a TiAl-based alloy (Wu 2006)

2.4.3 Different element's impact on TiAl γ alloys

The TiAl γ alloys are regarded as a class of TiAl alloys with great potential because of their high temperature performances (Lütjering and Williams 2003). However, the TiAl γ phase is a quite brittle intermetallic compound, and TiAl γ alloys also have a limited plasticity. Therefore there has been a large amount of researches to improve TiAl alloys' ductility. Third alloying elements can help with this problem. Many investigations were focused on alloys with Al-contents between 44 and 48 at.%. Figure 2.15 shows a part of Ti-Al phase diagram, and the movement of phase boundaries due to the addition of alloying elements (Wu 2006).

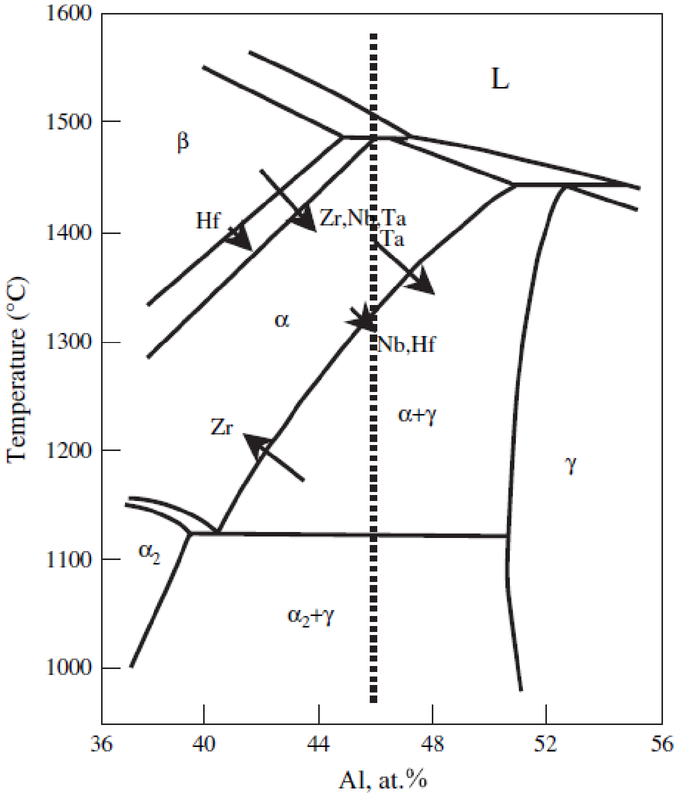

Figure 2.15 Section of the TiAl phase diagram. The arrows indicate the sense of movement of the phase boundaries for ternary alloying additions with the length of the arrow indicating the potency of each element

The effects of different additional alloying elements on TiAl-based alloys are listed below (Huang and Hall 1991, Maki, Shioda et al. 1992, Tsujimoto, Hashimoto et al. 1992, Kawabata, Tamura et al. 1993, Tian and Nemoto 1997, Kawabata, Fukai et al. 1998, Hu 2001, Hu 2002, Lütjering and Williams 2003, Wu 2006, QIU, Yong et al. 2012).

V: The addition of V can enhance the material’s ductility at room temperature. It can also refine the grain size.

Cr: The addition of Cr increases the tensile ductility, and refines the grain size as well.

Mn: The addition of Mn raises the ductility.

Mo: Mo is a more efficient alloying element to improve the ductility rather than Cr or Mn.

Nb: The addition of Nb improves oxidation resistance and strength.

W: The addition of W increases creep resistance and oxidation resistance and strength, however it lowers the ductility.

Ta: Ta can increase the oxidation resistance and strength.

B: B addition can refine the microstructure and have a positive effect on room temperature ductility.

C: C increases the creep resistance.

Nb is the most common alloying addition, while other elements are also added into the alloys in small amounts with specific benefits.

2.4.4 Specific Metallurgy about Ti-46Al-8Nb

Although research has shown that Al content should be as low as 42 at.% in TiAl alloys to get a better behaviour in hot working, many other investigations proved that Al content is required to be close to 46 at.% to achieve high temperature strength (Tetsui, Shindo et al. 2005, Wu 2007). The formulation Ti-(45-46)Al-(4-8)Nb with minor additions (like C or B) is widely accepted as the alloy that can offer best balanced performance among all those TiAl alloys with low ductility (Wu 2007). Ti-46Al-8Nb alloy is developed within the European funded FP6 IMPRESS project, and it is one of the advanced materials for gas-burning power-generation plants and turbines of aircraft engines in terms of its lightweight and good creep resistance to high temperature (800°C) (Jarvis and Voss 2005).

i. Microstructure and phase transformation of Ti-46Al-8Nb

According to the Ti-Al-Nb phase diagram with 8 at.% Nb (shown in Figure 2.16), the equilibrium solidification sequence of Ti-46Al-8Nb should be as following: (Kartavykh, Ginkin et al. 2011)

Liquid L → Liquid L + β-Ti → β-Ti → β-Ti + α-Ti → α-Ti + γ → α_2-Ti/γ + γ

Therefore, the final phases in Ti-46Al-8Nb at room temperature are α_2 and γ.

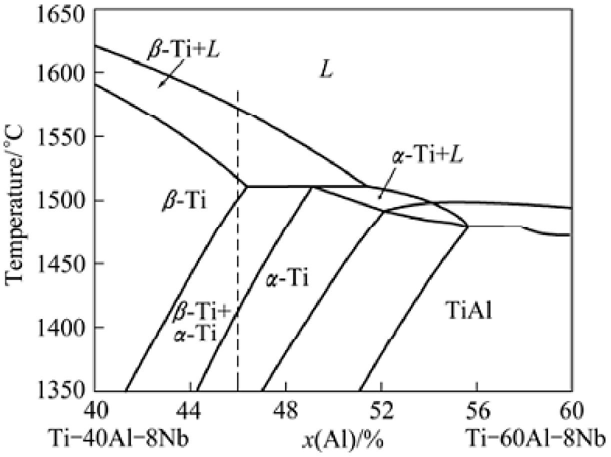

Figure 2.16 Calculated partial isopleth diagram of Ti-Al-Nb ternary system with 8 at.% Nb (Liu, G. H., et al. 2012).

However, different cooling rates lead to different microstructures. If the cooling rate is slow enough, the alloy is cooled from the single phase α field into the ($\alpha_2 + \gamma$) phase field, and then a fully lamellar phase will appear as Figure 2.17 shows (Hu 2002, Lütjering and Williams 2003).

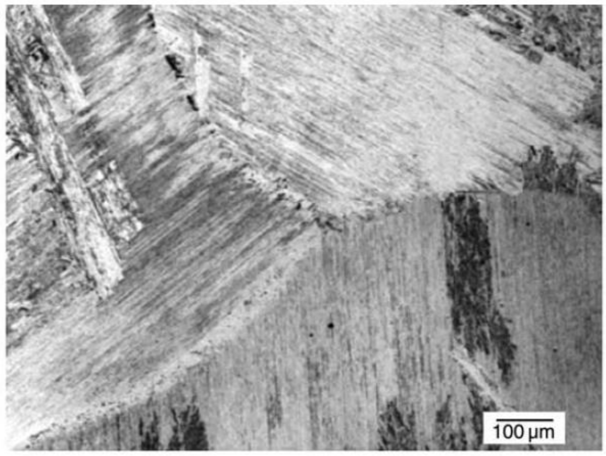

Figure 2.17 Optical microstructures in ingot cast Ti–46Al–8Nb. The sample was subjected to a solution treatment of 1360 8C/1 h (Hu 2002).

The typical microstructures in Ti-46Al-8Nb after Jominy end quenching also shows in Figure 2.18 (Hu, Huang et al. 2007).

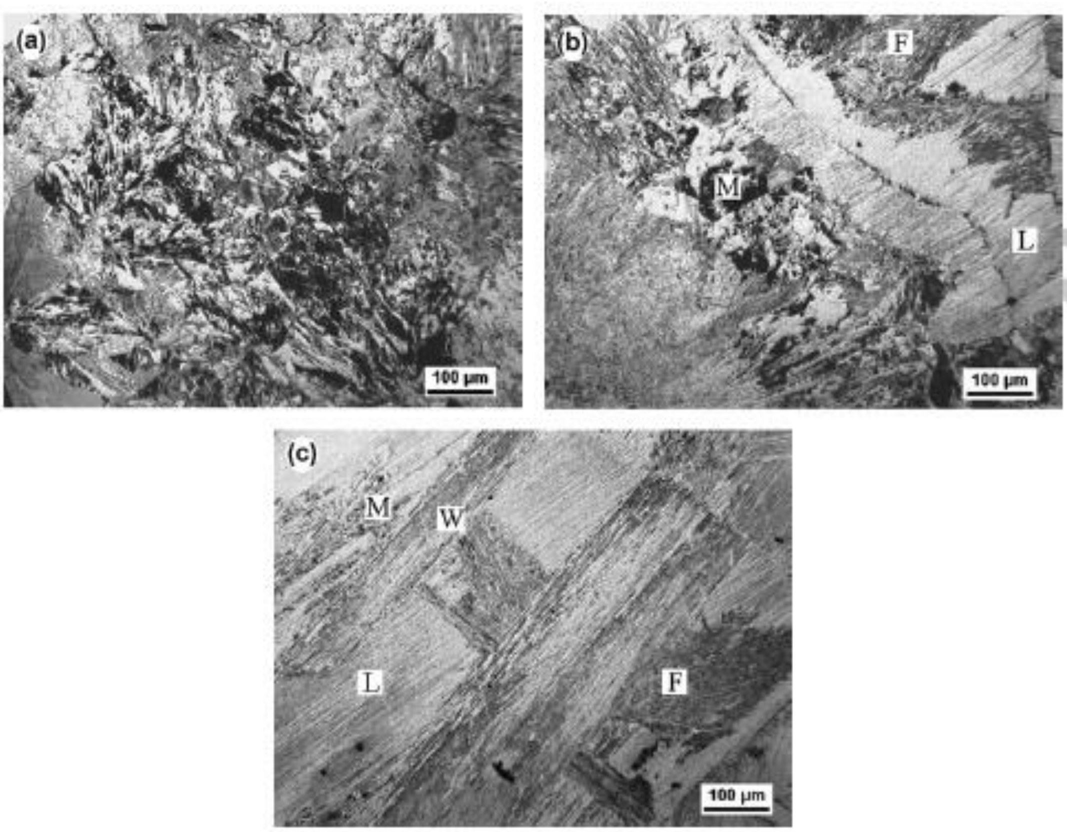

Figure 2.18 Typical optical microstructures in continuously cooled Ti-46Al-8Nb from 1360 °C (alpha phase field). (a) Fully massive γ obtained at a cooling rate of 180 °C s^{-1}, (b) a mixture of massive γ + feathery + lamellar microstructures obtained at a cooling rate of 25 °C s^{-}1 and (c) a mixture of feathery γ + Widmanstätten + lamellar microstructures obtained at a cooling rate of 10 °C s^{-1} (there is still a tiny fraction of massive γ at this cooling rate). Letters M, F, Wand L stand for massive, feathery, Widmanstätten and lamellar microstructures, respectively (Hu, Huang et al. 2007).

ii. Mechanical properties of Ti-46Al-8Nb

The fully lamellar microstructure materials have low room temperature strength and ductility but good creep resistance (Griffith, Keicher et al. 1996). The fraction of lamellar microstructure in TiAl alloys has significant influence on the performance of the alloys. Ti-46Al-8Nb with two different heat treatments is compared in terms of microstructures (shows in Figure 2.19) and tensile properties (shows in Table 2.2) (Huang, Hu et al. 2007).

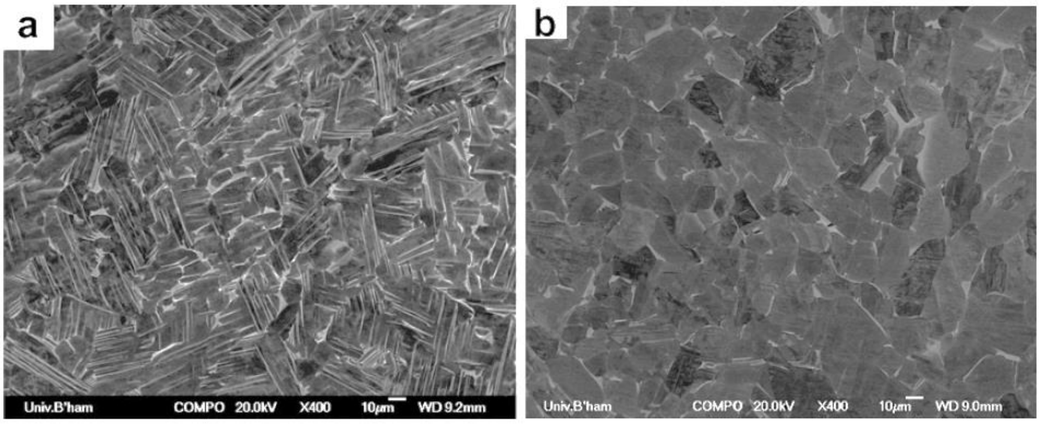

Figure 2.19 Backscattered scanning electron micrographs of massively transformed Ti–46Al–8Nb (a) HIPped for 4 h at 1280 °C and then annealed in vacuum for 2 h at 1280 °C and (b) HIPped for 6 h at 1280 °C and 150 MPa. Samples were cooled at 10 °C min^{-1} after annealing or HIPping (Huang, Hu et al. 2007).

Table 2.2 Tensile properties of massively transformed Ti–46Al–8Nb with different heat treatment (Huang, Hu et al. 2007)

Treatment	0.2% proof stress (MPa)	UTS (MPa)	Ductility (%)
HIPped for 6 h at 1280 °C and 150 MPa; cooled at 10 °C min^{-1}	345	436	0.8
HIPped for 4 h at 1280 °C and then annealed in vacuum for 2 h at 1280 °C; cooled at 10 °C min^{-1}	550	622	0.8

2.5 Summary of Literature

This literature review covers the following topics:

- Combinatorial materials science is an efficient way to explore new materials and improve material properties. Combinatorial materials science consists of three important aspects: systematic synthesis to prepare libraries, high-throughput screening for properties (characterization) and data storage and analysis. Systematic synthesis and high-throughput screening allow the whole exploration take less time than the conventional methods.

  Several methods were developed to make alloy libraries including depositing thin films consecutively together on the substrate using electron beam evaporation system and heat treat them to homogenize; depositing three different elements to the substrate from three corners at the same time by magnetron sputtering; and melting two different metal blocks with a deliberate thickness gradient together by focused electron-beam welding (EBW). Each of the techniques was found to have its own advantages and disadvantages, and none could produce a bulk sample (mm in size).

- Direct Laser Deposition is one of the laser-based addictive manufacturing processes that can fabricate net shape metallic parts. Metal powders are fed directly into the focused laser beam and get melted. CAD files can guide the deposit pattern, and with the overlay of layers a 3D net shape part can be build.

  There are many DLD process parameters that can influence the performance of DLD's final products. They are listed as: powder feed rate, laser power, laser/substrate relative traverse speed (laser scan speed), laser scanning strategy, and even powder's injection position (laser scanning direction).

- TiAl-based alloys are one kind of advanced materials that is quite attractive to the industries due to its low density, high temperature strength, high specific strength, high specific stiffness and good oxidation, corrosion resistance.

  However, with all these good properties, TiAl-based alloys have low room temperature ductility. The third additional alloying element can help to balance the properties of the alloys. The formulation Ti-(45-46)Al-(4-8)Nb with minor additions (like C or B) is widely accepted as the alloy that can offer best balanced performance among all those TiAl alloys with low ductility.

  Ti-46Al-8Nb alloy is developed within the Europe IMPRESS project, and it is one of the advanced materials for gas-burning power-generation plants and turbines of aircraft engines in terms of its lightweight and good creep resistance to high temperature (800°C). Some studies have been done to investigate the microstructure of the material and improve its performances.

This literature review provides the guidance in the study on several aspects:

- Combinatorial materials science is the suitable method for the AccMet project to explore the new alloys.
- DLD technique can be modified as a novel combinatorial synthesis to make bulk samples rapidly.
- More explorations of TiAl-based alloys can be undertaken by applying the modified DLD technique.

2.6 References

Collins, P., et al. (2003). "Laser deposition of compositionally graded titanium–vanadium and titanium–molybdenum alloys." Materials Science and Engineering: A **352**(1): 118-128.

Dai, K. and L. Shaw (2002). "Distortion minimization of laser-processed components through control of laser scanning patterns." Rapid Prototyping Journal **8**(5): 270-276.

Dicks, R., et al. (2009). "The manufacture of a niobium/niobium-silicide-based alloy using direct laser fabrication." Journal of Materials Processing Technology **209**(4): 1752-1757.

Djanarthany, S., et al. (2001). "An overview of monolithic titanium aluminides based on Ti 3 Al and TiAl." Materials Chemistry and Physics **72**(3): 301-319.

Ensz, M. T., et al. (2002). Critical Issues for Functionally Graded Material Deposition by Laser Engineered Net Shaping LENS. Proceedings of the 2002 MPIF Laser Metal Deposition Conference, San Antonio: TX.

Famodu, O. O., et al. (2004). "Combinatorial investigation of ferromagnetic shape-memory alloys in the Ni-Mn-Al ternary system using a composition spread technique." Materials Transactions **45**(2): 173-177.

Fenniri, H. (2000). "Combinatorial Chemistry." Combinatorial Chemistry.

Fleischauer, M., et al. (2005). "Combinatorial investigations of Si-M (M= Cr+ Ni, Fe, Mn) thin film negative electrode materials." Electrochemical and Solid-State Letters **8**(2): A137-A140.

Frazier, W. E. (2014). "Metal additive manufacturing: a review." Journal of Materials Engineering and Performance **23**(6): 1917-1928.

Gallop, M. A., et al. (1994). "Applications of combinatorial technologies to drug discovery. 1. Background and peptide combinatorial libraries." Journal of medicinal chemistry **37**(9): 1233-1251.

Gordon, E. M., et al. (1994). "Applications of combinatorial technologies to drug discovery. 2. Combinatorial organic synthesis, library screening strategies, and future directions." Journal of medicinal chemistry **37**(10): 1385-1401.

Griffith, M., et al. (1996). Free form fabrication of metallic components using laser engineered net shaping (LENS). Proceedings of the Solid Freeform Fabrication Symposium, University of Texas at Austin Austin, TX.

Hanak, J. J. (1970). "The “multiple-sample concept” in materials research: Synthesis, compositional analysis and testing of entire multicomponent systems." Journal of Materials Science **5**(11): 964-971.

Hu, D. (2001). "Effect of composition on grain refinement in TiAl-based alloys." Intermetallics **9**(12): 1037-1043.

Hu, D. (2002). "Effect of boron addition on tensile ductility in lamellar TiAl alloys." Intermetallics **10**(9): 851-858.

Hu, D., et al. (2007). "On the massive phase transformation regime in TiAl alloys: The alloying effect on massive/lamellar competition." Intermetallics **15**(3): 327-332.

Huang, A., et al. (2007). "The influence of pressure on solid-state transformations in Ti–46Al–8Nb." Scripta Materialia **56**(4): 253-256.

Huang, S.-C. and E. Hall (1991). "Characterization of the effect of vanadium additions to TiAl base alloys." Acta Metallurgica Et Materialia **39**(6): 1053-1060.

Islam, M. U., et al. (2001). Process for manufacturing or repairing turbine engine or compressor components, Google Patents.

Jarvis, D. and D. Voss (2005). "IMPRESS Integrated Project—an overview paper." Materials Science and Engineering: A **413**: 583-591.

Jeantette, F. P., et al. (2000). Method and system for producing complex-shape objects, Google Patents.

J. Tušek, & M. Suban. (2003). "High-productivity multiple-wire submerged-arc welding and cladding with metal-powder addition". Journal of Materials Processing Technology, **133**(1–2), 207-213.

Kartavykh, A., et al. (2011). "Convection-induced peritectic macro-segregation proceeding at the directional solidification of Ti–46Al–8Nb intermetallic alloy." Materials Chemistry and Physics **126**(1): 200-206.

Kawabata, T., et al. (1998). "Effect of ternary additions on mechanical properties of TiAl." Acta Materialia **46**(6): 2185-2194.

Kawabata, T., et al. (1993). "Effect of Ti/Al ratio and Cr, Nb, and Hf additions on material factors and mechanical properties in TiAl." Metallurgical Transactions A **24**(1): 141-150.

Kobryn, P. A. and S. Semiatin (2003). "Microstructure and texture evolution during solidification processing of Ti–6Al–4V." Journal of Materials Processing Technology **135**(2): 330-339.

Li, Y., et al. (2003). "The influences of processing parameters on forming characterizations during laser rapid forming." Materials Science and Engineering: A **360**(1): 18-25.

Liu, G. H., et al. (2012). "Microstructure and microsegregation in directionally solidified Ti–46Al–8Nb alloy." Transactions of Nonferrous Metals Society of China **22**(6): 1342–1349.

Lütjering, G. and J. C. Williams (2003). Titanium, Springer.

Maier, W. F., et al. (2007). "Combinatorial and high-throughput materials science." Angewandte chemie international edition **46**(32): 6016-6067.

Maki, K., et al. (1992). "Effect of silicon and niobium on oxidation resistance of TiAl intermetallics." Materials Science and Engineering: A **153**(1-2): 591-596.

Mazumder, J., et al. (1997). "The direct metal deposition of H13 tool steel for 3-D components." JOM **49**(5): 55-60.

Megahed, M., et al. (2016). "Metal additive-manufacturing process and residual stress modeling." Integrating Materials and Manufacturing Innovation **5**(1): 4.

Merrifield, R. B. (1963). "Solid phase peptide synthesis. I. The synthesis of a tetrapeptide." Journal of the American Chemical Society **85**(14): 2149-2154.

Murray, J. L. (1987). "Phase diagrams of binary titanium alloys." ASM International, 1987: 354.

Nickel, A., et al. (2001). "Thermal stresses and deposition patterns in layered manufacturing." Materials Science and Engineering: A **317**(1): 59-64.

Pei, Y. T. and J. T. M. De Hosson (2000). "Functionally graded materials produced by laser cladding." Acta Materialia **48**(10): 2617-2624.

Pharr, G. M., et al. (2005). Development of Combinatorial Methods for Alloy Design and Optimization, University of Tennessee, Knoxville, TN.

Pickin, C. G., Williams, S. W., Prangnell, P. B., Robson, J., & Lunt, M. (2009). Control of weld composition when welding high strength aluminium alloy using the tandem process. Science & Technology of Welding & Joining, 14(8), 734-739.

Pickin, C. G., Williams, S. W., Prangnell, P., Derry, C., & Lunt, M. (2010). Control of weld composition when arc welding high strength aluminium alloys using multiple filler wires. Science & Technology of Welding & Joining, 15(6), 491-496.

Potyrailo, R. A. (2004). Combinatorial and artificial intelligence methods in materials science II, Materials Research Society.

QIU, C.-z., et al. (2012). "Effect of Fe and Mo additions on microstructure and mechanical properties of TiAl intermetallics." Transactions of Nonferrous Metals Society of China **22**(3): 521-527.

Ram, G. J., et al. (2008). "Microstructure and wear properties of LENS® deposited medical grade CoCrMo." Journal of Materials Science: Materials in Medicine **19**(5): 2105-2111.

Selcuk, C. (2011). "Laser metal deposition for powder metallurgy parts." Powder Metallurgy **54**(2): 94-99.

Shamsaei, N., et al. (2015). "An overview of Direct Laser Deposition for additive manufacturing; Part II: Mechanical behavior, process parameter optimization and control." Additive Manufacturing **8**: 12-35.

Specht, E., et al. (2003). "Nonequilibrium Structures in Codeposited Cr-Fe-Ni Films". MRS Proceedings, Cambridge Univ Press.

T.Ashton. (1954). "Twin-arc Submerged Arc Welding". Welding Journal **33**(4): 350-355.

Tetsui, T., et al. (2005). "Fabrication of TiAl components by means of hot forging and machining." Intermetallics **13**(9): 971-978.

Tian, W. and M. Nemoto (1997). "Effect of carbon addition on the microstructures and mechanical properties of γ-TiAl alloys." Intermetallics **5**(3): 237-244.

Traini, T., et al. (2008). "Direct laser metal sintering as a new approach to fabrication of an isoelastic functionally graded material for manufacture of porous titanium dental implants." Dental materials **24**(11): 1525-1533.

Tsujimoto, T., et al. (1992). "Alloy design for improvement of ductility and workability of alloys based on intermetallic compound TiAl." Materials Transactions, JIM **33**(11): 989-1003.

Wang, F., et al. (2007). "Compositionally graded Ti6Al4V+ TiC made by direct laser fabrication using powder and wire." Materials & design **28**(7): 2040-2046.

Wu, D., et al. (2011). "Laser rapid manufacturing of stainless steel 316L/Inconel718 functionally graded materials: microstructure evolution and mechanical properties." International Journal of Optics **2010**.

Wu, X. (2006). "Review of alloy and process development of TiAl alloys." Intermetallics **14**(10–11): 1114-1122.

Wu, X. (2007). "A review of laser fabrication of metallic engineering components and of materials." Materials science and technology **23**(6): 631-640.

Wu, X., et al. (2004). "Microstructures of laser-deposited Ti–6Al–4V." Materials & design **25**(2): 137-144.

Xiang, X.-D. (1999). "Combinatorial materials synthesis and screening: an integrated materials chip approach to discovery and optimization of functional materials." Annual Review of Materials Science **29**(1): 149-171.

Xiang, X.-D. (2002). "Mapping of physical properties–composition phase diagrams of complex material systems using continuous composition material chips." Applied surface science **189**(3): 188-195.

Xiang, X.-D. (2004). "High throughput synthesis and screening for functional materials." Applied surface science **223**(1): 54-61.

Xiang, X.-D. and I. Takeuchi (2003). Combinatorial materials synthesis, CRC Press.

Xiang, X., et al. (1995). "A combinatorial approach to materials discovery." Science **268**(5218): 1738.

Xue, L., et al. (2000). Laser consolidation of Ni-base IN-738 superalloy for repairing gas turbine blades. ICALEO 2000: Laser Materials Processing Conference.

Yu, J., et al. (2011). "Influence of laser deposition patterns on part distortion, interior quality and mechanical properties by laser solid forming (LSF)." Materials Science and Engineering: A **528**(3): 1094-1104.

Zhao, J.-C. (2005). "The diffusion-multiple approach to designing alloys." Annu. Rev. Mater. Res. **35**: 51-73.

Zhao, J.-C. (2006). "Combinatorial approaches as effective tools in the study of phase diagrams and composition–structure–property relationships." Progress in Materials Science **51**(5): 557-631.

Zhao, J.-C., et al. (2005). "High-throughput diffusion multiples." Materials Today **8**(10): 28-37.

CHAPTER 3: Materials & Experimental Methods

3.1 Materials

In this study, most of the samples were made by laser melting using different elemental metal wires. The original materials are close to 100% purity metal wires. The wires suppliers and its diameters are listed in Table 3.1.

Table 3.1 Elemental metal wires used in the project

Element	Supplier	Sizes(Diameter in mm)
Ti	Advent	1 and 0.5
Al	Advent	1 and 0.5
Nb	Plansee	0.5
V	Goodfellow	1
Co	Ronglu	0.5
Hf	Ronglu	0.7
Zr	Ronglu	0.5

Moreover, an as-casted Ti-46Al-8Nb alloy cube was provided by Dr. David Hu. It was Hot Isostatically Pressed (HIP) at 1280 ^{0}C and 150 MPa for 4 hours. This heat treatment was performed to maintain the as-casted microstructure.

3.2 Suspended Droplet Alloying (SDA)

Suspended Droplet Alloying is a novel technique based on modified version of Direct Laser Fabrication (DLF). It allows researchers to rapidly make samples with an accurate composition using wire feedstock.

3.2.1 The SDA Process

The SDA process is a simplified version of DLF and does not produce a net-shape component. Therefore, unlike the traditional DLF process there is no need to prepare CAD files to create a tool path. The positioning table (horizontal) is stable as the X-axis and Y-axis are fixed. Only the Z-axis (vertical) is controlled manually to adjust to the specimens’ height as more materials are deposited onto the substrate.

Developed as a tool for combinatorial metallurgy where a large number of compositionally-varying alloy samples are needed, the process has been designed to make a sample with a target composition rapidly and with a good compositional accuracy. The traditional DLF process cannot meet the requirement; the feeding of powder feedstock is difficult to do accurately with good reproducibility over a wide range of addition rates. The powder capture rate during the DLF process is also far from 100% with powders with different morphologies or densities being delivered with a range of accuracy. Therefore, in the SDA process, powder feedstock is replaced by elemental wire. Since the composition of the sample is determined by the amount of wires that are fed together, by controlling the feeding speed of the wires, a sample with target composition can be achieved. 100% of the fed wire is incorporated in the sample.

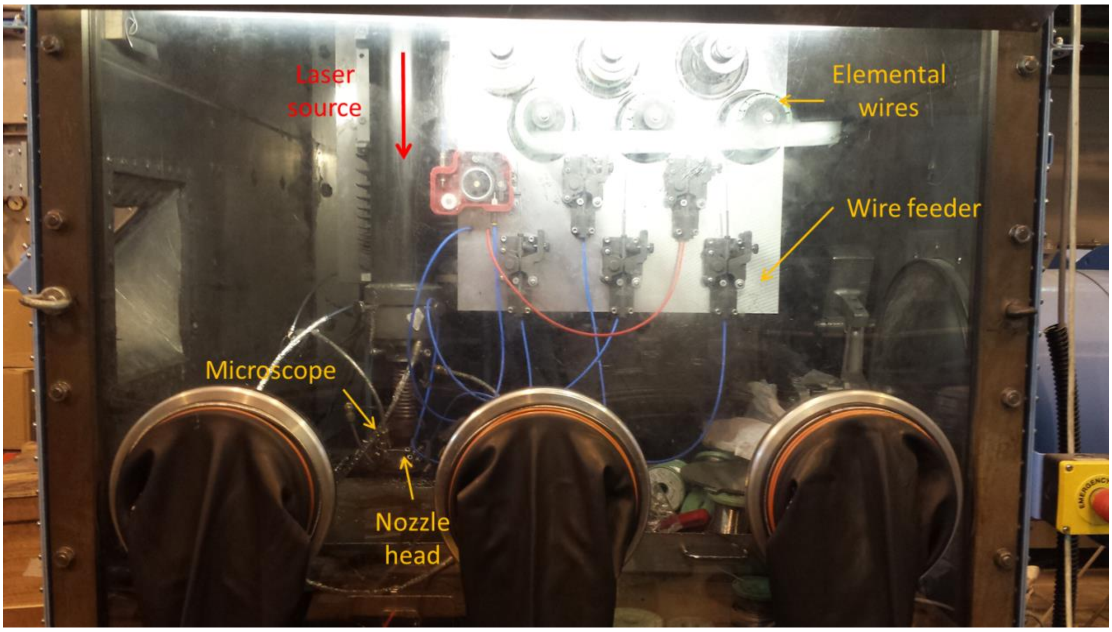

Figure 3.1 The SDA system

Figure 3.1 shows the SDA system which is in a large argon filled glove box. The laser source in the system is a Rofin Sinar Triagon CO_2 laser with a wavelength of 10.6 μm, and the maximum laser power is 1972 W. There are six wire feeders in the system currently so an alloy with up to six elements can readily be made. Even more elements can be added into the alloy if pre-alloyed wires are used. The feeding rollers in wire feeder has two grooves, and the widths of the grooves are 0.6 mm and 0.8-0.9 mm. Therefore wires cannot be too thin or thick; otherwise the feeder can’t feed it properly. The range of the wire’s diameter should be 0.5-1.2 mm.

The laser generator was placed outside the chamber. The beam was introduced into the chamber horizontally through a ZnSe window and redirected downwards along the Z-axis by a gold coated water cooled mirror. A focus lens and a copper nozzle are mounted on the Z-axis as shown in Figure3.2, and their relative distance does not vary as the nozzle move along the Z-axis. It can keep the focus position at the same point relative to the nozzle. The focus distance is determined by the lens and the distance between the lens and the nozzle. A stream of Argon gas flows from the lens to the nozzle. The gas can protect the lens from dust (metal fume) which if it contaminates the lens tends to lead to breakage. The gas can also cool the processed material and the nozzle, although the Cu nozzle is mainly cooled by water.

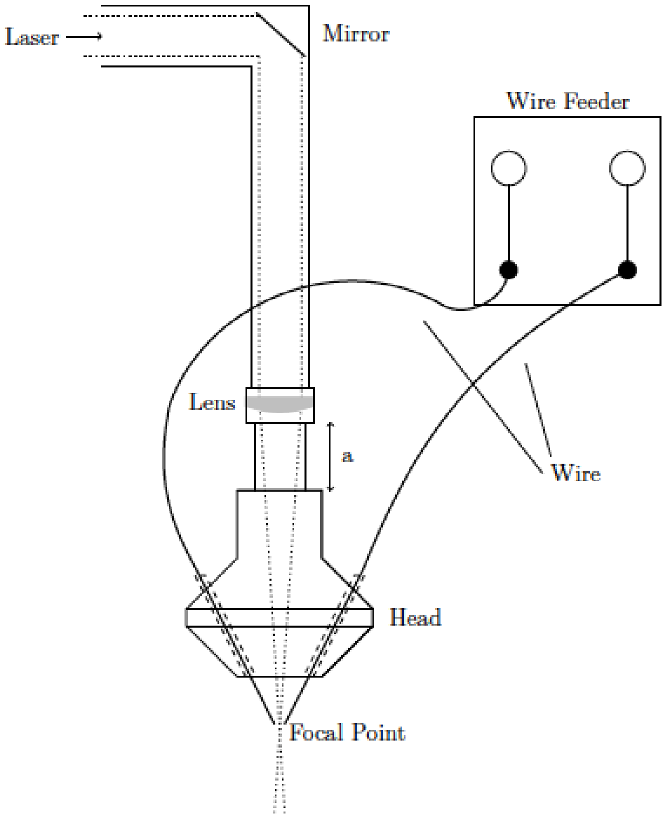

Figure 3.2 The "modified" SDA Accelerated Metallurgy setup (not to scale) (Hauptstein, B 2014)

In the SDA process the wires are firstly fed into individual holes in the nozzle head. The wires meet with each other under the focus of the laser beam, and get melted together. The initial alloy metal ball starts to grow at the end of the wires, with only surface tension suspending the droplet in the path of the laser beam. As the wires keep feeding, more and more material is melted into the suspended alloy ball. The ball continues to grow until the mass becomes too large for the surface tension to hold it anymore. Then the alloyed droplet deposits on the substrate.

The first droplet deposits on the substrate and create a melting pool. The following droplets fall into the melting pool directly and undergo further mixing. The melting pool is at the top of the sample at the bottom of the laser beam path. The melting pool moves upward with the overlay of droplets and the bottom of the melting pool solidifies gradually. A cylinder-like alloyed sample can be made in a few minutes (shown in Figure 3.3).

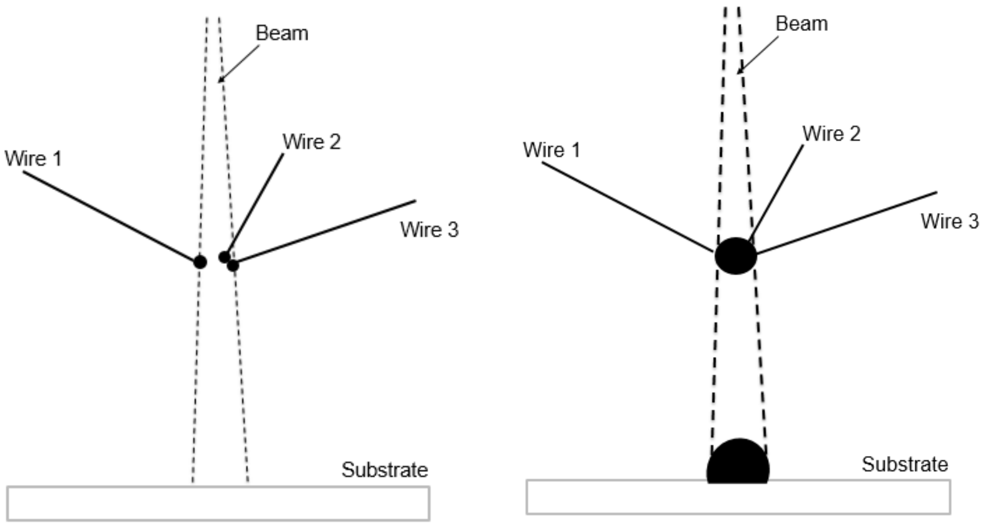

a

b

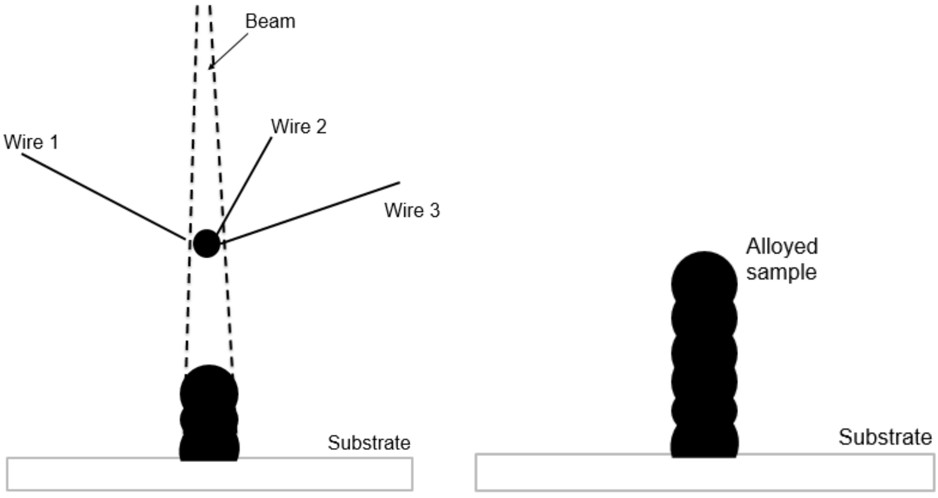

c d

Figure 3.3 Schematics of SDA process

3.2.2 CNC controlled wire-feed system

The wire feeding rate is controlled by the CNC controlled system. The system consists of three parts: software, control boards and step motors. The software Modcom Version 5.6 is used to send commands to the control board (from Weeder Technology) which then control the step motor rotation.

The step motor has 400 steps that can move 0.9° with each step. The circumference of the drive wheel is 93mm which means wire can feed 0.2325mm per step. However, the size of these steps can be decreased via microstepping. The control board has a number of microstepping settings as Table 3.2 shows.

Table 3.2 Modes of microstepping

Mode	1	2	4	8	16	32	64
Moving angle	0.9°	0.45°	0.225°	0.1125°	0.0563°	0.0281°	0.0141°
Feeding speed (mm/min)	697.5	348.8	174.4	87.2	43.6	21.8	10.9

As the software interface shows (Figure 3.4), the wire feeding rate is determined by two factors: the microstepping mode selected and number of pulses sent to the motor per second (limited to multiples of 50 by the software). Therefore, the wire feeder cannot realise all particular feeding speeds. The feeding rate is adjusted with the other elements' wire feeding rate to get the target composition.

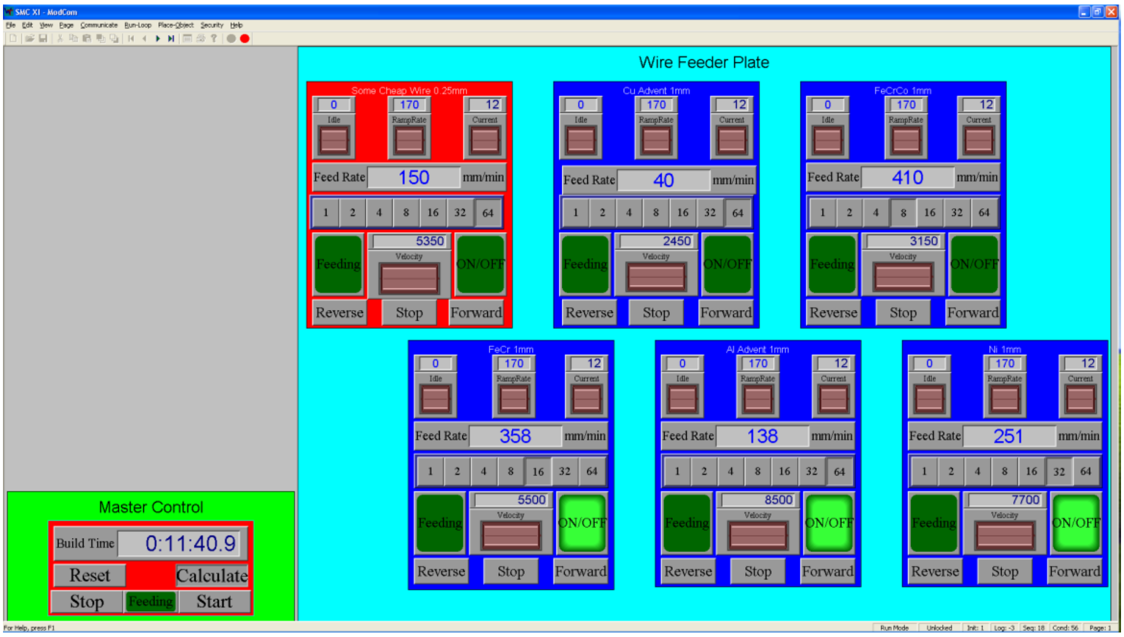

SMC XI - ModCom

Wire Feeder Plate

Some Cheap Wire 0.25mm
Idle 0 | RampRate 170 | Current 12
Feed Rate 150 mm/min
Velocity 5350

Cu Advent 1mm
Idle 0 | RampRate 170 | Current 12
Feed Rate 40 mm/min
Velocity 2450

FeCrCo 1mm
Idle 0 | RampRate 170 | Current 12
Feed Rate 410 mm/min
Velocity 3150

FeCr 1mm
Idle 0 | RampRate 170 | Current 12
Feed Rate 358 mm/min
Velocity 5500

Al Advent 1mm
Idle 0 | RampRate 170 | Current 12
Feed Rate 138 mm/min
Velocity 8500

Ni 1mm
Idle 0 | RampRate 170 | Current 12
Feed Rate 251 mm/min
Velocity 7700

Master Control
Build Time 0:11:40.9

For Help, press F1

Figure 3.4 Modcom software interface

3.2.3 Feeding rate calculation

Wires' feeding rates are controlled to make samples with target composition. Software FileMaker Pro has been developed not only to construct the database for all the fabricated SDA samples, but can also help the researcher find the wires' feeding rate for a given composition. An algorithm is introduced in the software to calculate the composition for given wires' feeding rate.

For example if Wire 1, 2 and 3 are fed together in a given speed v_1, v_2, v_3, then in this ternary alloy element 1's atomic fraction $N_1 = (100\times(n_1\times v_1))/N_{sum}$,where n_1 is Wire 1's molecule number per length and N_{sum} is the total molecule number. $N_{sum} = (n_1\times v_1) + (n_2\times v_2) + (n_3\times v_3) + (n_4\times v_4) + (n_5\times v_5)$. Wire 4 and 5 have not fed, and then v_4 and v_5 are 0. Element 2 and 3 have the similar equations as N_1. The weight fraction of each element can also be calculated in the same way. Figure 3.5 shows the panel of FileMaker, and there is a record of Ti-46Al-8Nb on it. As the figure shows, Ti, Al and Nb's feeding rate are typed in and the software returns the corresponding composition.

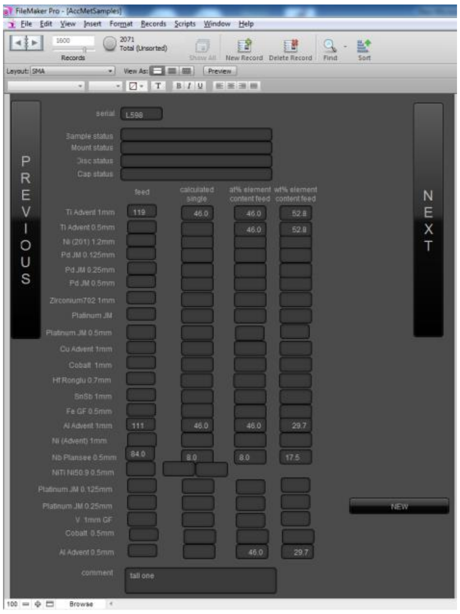

serial L598

Sample status

Mount status

Disc status

Cap status

	feed	calculated single	at% element content feed	wt% element content feed
Ti Advent 1mm	119	46.0	46.0	52.8
Ti Advent 0.5mm			46.0	52.8
Ni (201) 1.2mm				
Pd JM 0.125mm				
Pd JM 0.25mm				
Pd JM 0.5mm				
Zirconium702 1mm				
Platinum JM				
Platinum JM 0.5mm				
Cu Advent 1mm				
Cobalt 1mm				
Hf Ronglu 0.7mm				
SnSb 1mm				
Fe GF 0.5mm				
Al Advent 1mm	111	46.0	46.0	29.7
Ni (Advent) 1mm				
Nb Plansee 0.5mm	84.0	8.0	8.0	17.5
NiTi Ni50.9 0.5mm				
Platinum JM 0.125mm				
Platinum JM 0.25mm				
V 1mm GF				
Cobalt 0.5mm				
Al Advent 0.5mm			46.0	29.7

comment tall one

Figure 3.5 FileMaker's fabrication panel

For every new wire added into the database, its weight per length and molecule number per length need to be calculated. Three different lengths of the wire are weighing using electronic balance, and the lengths are measured as well. An average weight per length and molecule number per length of the wire can be known. For the wires used in this study, the relevant information is shown in Table 3.3.

Table 3.3 Data for wires of interest

Wire	Weight per length (g/m)	Moles per length (mol/m)
0.5 mm Ti	0.86317	0.01827
1 mm Ti	3.47541	0.07261
0.5 mm Al	0.5244	0.01944
1 mm Al	2.09647	0.0777
0.5 mm Nb	1.6283	0.01784
1 mm V	4.84583	0.09513
0.5 mm Zr	1.27545	0.01383
0.5 mm Co	2.9369	0.04983
0.7 mm Hf	6.7406	0.03776

3.2.4 Samples made by SDA

Most of the samples in the AccMet project were ternary alloys, with some simple TiAl-based alloy systems were made early in the project, like Ti-Al-Fe & Ti-Al-V. Then in this study, the research was focused on the higher temperature Ti-Al-Nb system with its potential in industrial applications. The range of samples in each ternary system has target compositions dispersed uniformly across the whole phase diagram. Each sample has a 10% compositional difference compared to the next one. For example, Figure 3.6 shows the samples with target compositions in Ti-Al-Nb ternary system.

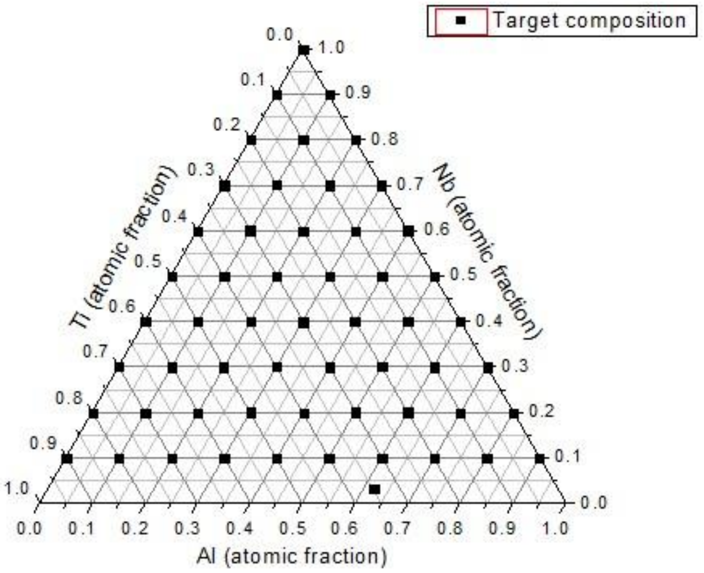

Figure 3.6 Ti-Al-Nb samples with different composition formulations spread across the ternary diagram

Among all these Ti-Al-Nb samples, Ti-46Al-8Nb was selected for further research. Ti-46Al-8Nb samples were made using different SDA parameters in order to optimize the process parameters. Moreover, the fourth element was added based on Ti-46Al-8Nb to investigate the development potential of Ti-Al-Nb alloys. With the addition of the fourth element, the following samples were made: Ti-46Al-4Nb-4V, Ti-46Al-4Nb-4Hf, Ti-46Al-4Nb-4Zr, Ti-46Al-4Nb-4Co. Ti-46Al-8Hf samples were also made for comparison.

Theoretically there is no limit for the number of alloy droplets the machine can produce, so a sample can be built as high as it required. Generally samples are made in three different sizes. The first one is a splat formed by one single droplet. The standard sample's height is around 12 mm (including the thickness of the substrate – 2 mm). The last size is around 50 mm, and these tall samples were used for tensile tests. The splats are deposited on a large copper plate but the other samples were generally made on 20 mm diameter stainless steel substrates. Different numbers are laser-marked on the back of each substrate so that once a sample has been made it will have a unique number.

3.3 Sample Preparations

Since there are a large amount of samples in the project, the preparation process was streamlined to improve efficiency.

3.3.1 Cutting

A Cut 20 EDM (ectric discharge) machine from AgieCharmilles is used to cut the samples. Two different types of samples were cut on the machine.

a. Standard samples

For a standard sample, the height was selected to be 8 mm (plus the 2mm thick substrate). Firstly the sample's top was removed; leaving the height of sample 9.25 mm. Then, a 1 mm thick disc was cut from it, leaving the height of sample 8 mm. The cutting wire has a diameter of 0.25 mm, which needs to be considered during the setup of cutting position and path. The 1 mm disc was used for experiments like Differential Scanning Calorimetry (DSC), superconductivity testing and so on. The remaining 8 mm tall bottom part then was mounted and polished and then characterised for microstructure (shown in Figure 3.7).

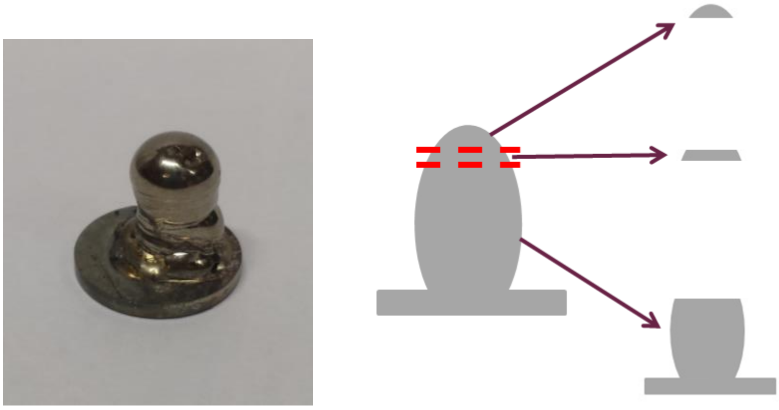

Figure 3.7 Sample's cutting requirement

A sample needs two cuts to be divided into three parts: a cap, a disc and the base. As there were many samples to be processed it was more efficient to cut several samples at one time. An Al bar was used to hold the samples on the operation table. 10 magnets were drilled into the Al bar. The samples can be stuck on the magnets, because their substrate was selected to be martensitic stainless steel (410). Thus, 10 samples could be fixed in a row and cut at one time.

b. Tensile samples

The tensile sample in Electrothermal Mechanical Testing System (ETMT) is much smaller than the standard ones. The size of ETMT sample is shown in Figure 3.8. This test specimen was cut from the SDA tall samples by EDM.

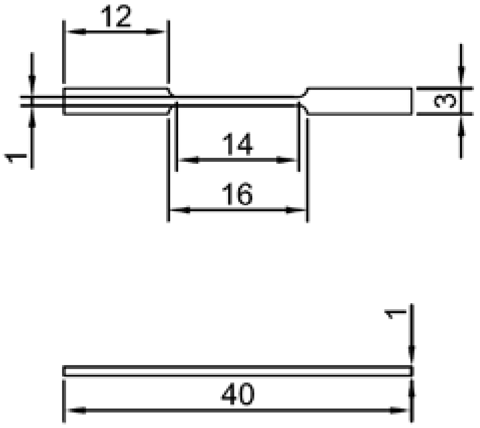

Figure 3.8 ETMT Test Specimen Dimensions (mm)

3.3.2 Mounting

For standard AccMet samples, cold mounting was chosen instead of hot mounting as it can mount more than one sample at a time, taking less time. Cold mounting uses self-curing resin - VersoCit-2 Powder mixed with VersoCit-2 Liquid. The mixing ratio is 2 parts of powder with 1 part of liquid by volume. The curing time is around 10 min. The resin has no colour; however Struers AcryDye can be added to change the colour of the resin. There are yellow, blue and red basic colours, so a lot of different colours can be produced by mixing. Samples with different colour can help to distinguish different alloy systems. The PTFE moulds from Kemet have a diameter of 20 mm (shown in

Figure 3.9), which is the size selected for the AccMet samples. The base of the mounted sample is stainless steel substrate, so the sample is still conductive from bottom to top. Extra silver paint is not needed for Scanning Electron Microscopy.

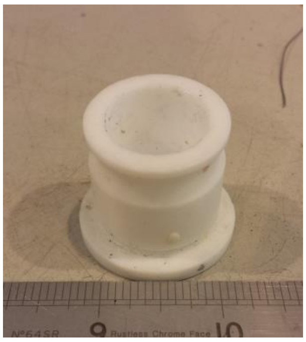

Figure 3.9 Kemet 20 mm mold

The other samples were hot mounted by OPAL 400/460 using conductive Bakelite. The diameter of the mounted sample is 25 mm. It takes around 15 min to mount a sample.

3.3.3 Polishing

The samples were polished using Struers Tegramin-25. This machine can be equipped with a holder for 20 mm samples. The holder can fix 12 samples on it (shown in Figure 3.10), so 12 samples can be polished at the same time. The samples were ground to 1200 grade-SiC paper, then polished using 6, 3 and 1 µm diamond suspensions, and finished with OP-U suspension (colloidal silica suspension for final polishing).

Figure 3.10 Sample holder on Struers Tegramin-25

3.4 Optical and Scanning Electron Microscopy (SEM)

Metallographic study was carried out to check the defects in the samples and their homogeneity. Optical images of polished samples were taken to check the cracks and porosity in the samples. Optical images of samples after etching were also taken to exam the grain size and the inclusions in it. Zeiss Axioskop 2 equipped with AxioVision software was used to take optical images. Ti-Al-Nb samples' diameter is normally 12-16 mm, and the entire sample need to be checked, so mosaic mode in AxioVision was applied. In mosaic mode, and under the lowest magnification (50x), near 10 X 10 optical images across the whole sample can be taken automatically once been set up. Then these 100 images are stitched together to give a complete optical image of a big sample. The polished samples were etched using Kroll's Reagent (2 ml HF, 6 ml HNO3, and 92 ml distilled water). Kroll's Reagent is effective for titanium and alloys, and all the samples in this study are Ti-Al based alloys. The samples were immersed in Kroll's Reagent for 15-30 seconds at room temperature for etching.

Two SEMs have been used to characterize the samples. First, all the polished samples back-scattered images (BSE) and energy dispersive X-ray spectroscopy (EDX) mapping was performed on a Hitachi TM3000. The TM3000 is a low cost, benchtop SEM which although it only has an analysis voltage of 15kV, it is convenient for checking the homogeneity of the samples. Further SEM work were performed on a Jeol 7000 equipped with an Oxford instruments Inca 300 EDS system as it can provide a more accurate result than TM3000. The working voltage on Jeol 7000 was 20kV.

Compositional contours were also operated on Jeol 7000. EDX was used to do area analysis for the whole image with a magnification of 1000X, and each area has a distance of 1 mm until it covers the whole surface of the sample. Then the compositional contour was made out by Origin Pro based on the EDX data. The compositional contour can show the distribution of each element across the whole sample directly.

3.5 Microhardness tests

The hardness contour was operated by automated Struers Dura Scan-50 microhardness machine. The load used was 1kg, and the points' distance in the matrix was 1 mm. The microhardness tests were performed on the CSM micro-indentation tester with high resolution camera in conjunction with Indentation software (see in Figure3.11). The software can control indentation parameters, real time display and record force and depth data during the indentation and calculate hardness and elastic modulus automatically. The Vickers indenter's contact force was 10 mN, and the maximum load was 10 N. The loading was linear, and both loading and unloading rate were 20 N/min.

The maximum load would hold for 10 s once it reached 10 N. The measurement’s acquisition rate was 10 Hz. The indents were aligned on a central axis (as shown in Figure 4.18), with spacing on 1mm. Each sample had 8-9 indents depend on the size of the sample. The hardness contour was operated by automated Struers Dura Scan-50 microhardness machine. The load used was 1kg, and the points’ distance in the matrix was 1 mm (see in Figure 4.20).

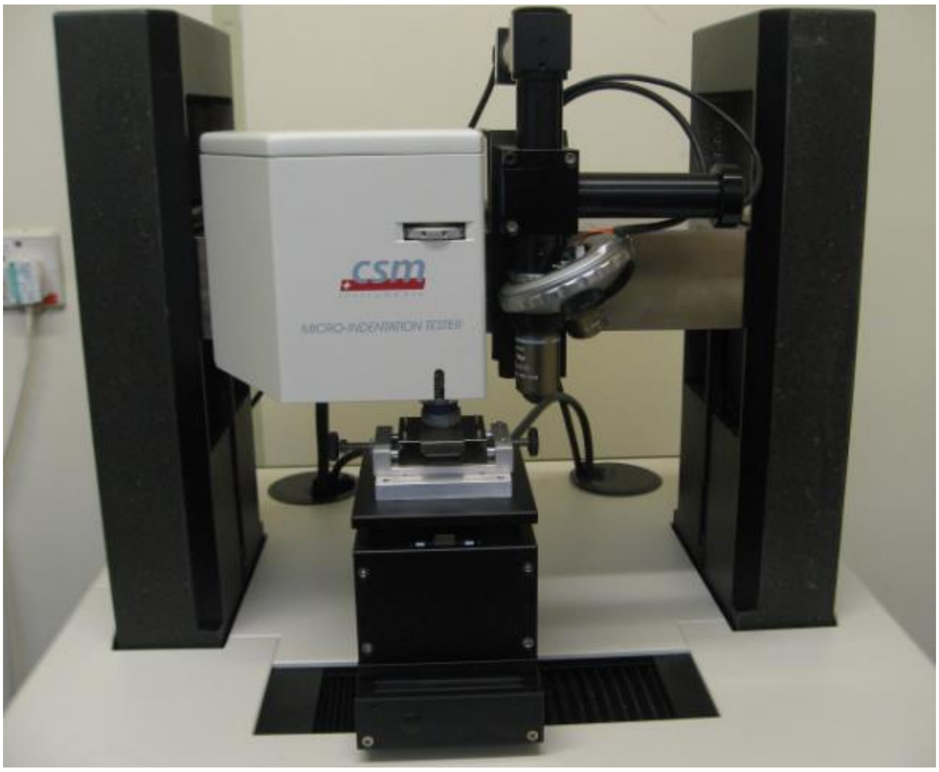

Figure3.11 The CSM micro-indentation tester

3.6 Electrothermal Mechanical Testing System (ETMT)

SDA samples’ size is limited by the materials, the laser power and the number of feeding wires. For Ti-Al-Nb samples, the diameter is generally 12-16 mm but it would take a long time and considerable amounts of expensive feedstock wire to produce a sample long enough to cut a regular tensile sample. Therefore an Electrothermal Mechanical Testing System ETMT was used to test Ti-Al-Nb samples' mechanical properties as this only requires a short specimen (40mm long)

ETMT test was performed at the University of Oxford using the Instron ETMT8800 Electrothermal Mechanical Testing System equipped with iMetrum strain camera (see in Figure 3.12-a). Samples were firstly ground with 800 and 1200 grit paper to remove any larger surface roughness and to achieve a good finish, and then sprayed alternatively with white and black paint, so as to create a point pattern that can be detected by the iMetrum strain camera (see in Figure 3.12-b). Samples were placed in the ETMT machine and fastened into place with screws. Special cut grips were used to make sure the samples would only be loaded with a uniaxial stress and would not experience any further bending forces and shear stresses. The gauge length used was 14 mm. The strain camera was focused onto the sample surface and two marker areas were chosen between which the camera should measure strain. Further inputs for the camera were the sample dimensions for calculating uniaxial stress (around 1mm each), the stress values between which the elastic modulus should be measured (chosen as 50 and 100 MPa), and the strain value for proof stress (chosen as 0.2%). The camera was then set to start recording images with a frequency of 5Hz. The test was started with the Instron WaveMatrix software. The first step was to increase the load from 0 to 2N, the second step to hold this load of 2N for 5s. In the third step, load was increased at a constant true strain rate of 10^-4 1/s until the sample failed. True strain rate was chosen intentionally instead of engineering strain rate, so that the crosshead velocity was not constant during the test, but was rather steadily increased.

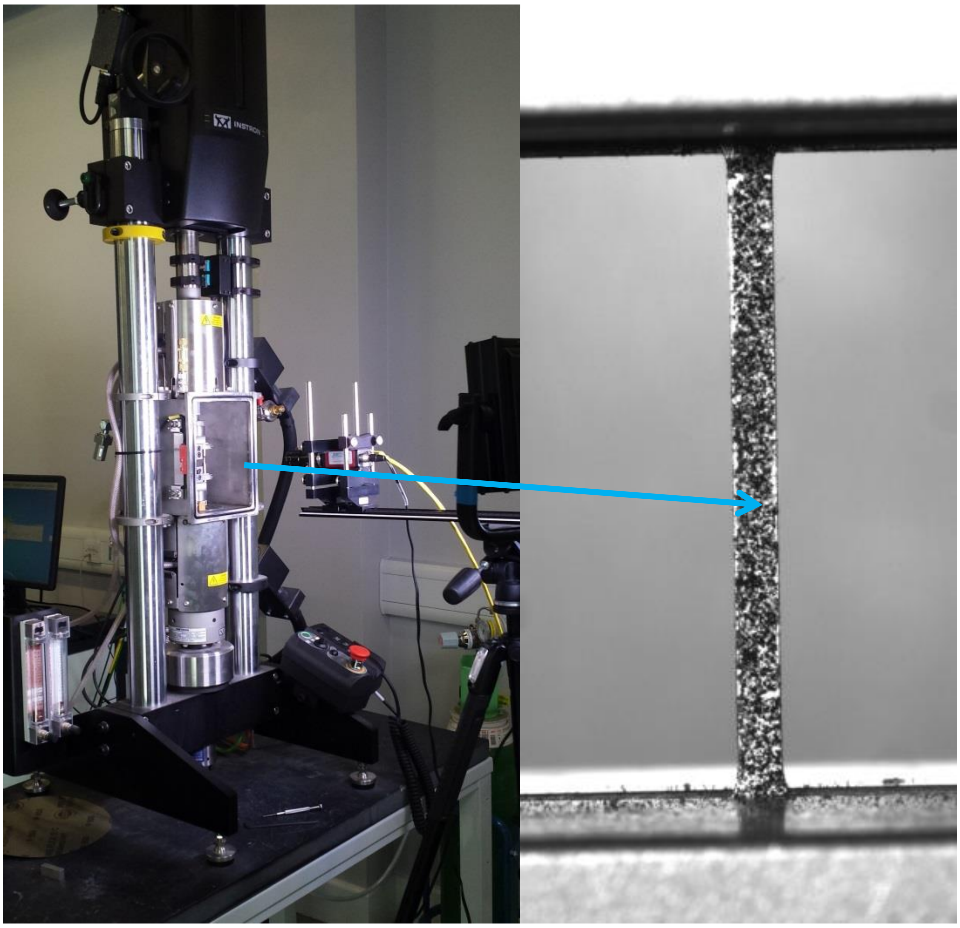

a b

Figure 3.12 a) Instron ETMT8800 Electrothermal Mechanical Testing System equipped with iMetrum strain camera; b) sample covered with white and black point pattern (recorded by the camera)

3.7 X-Ray Diffraction (XRD)

Phase analysis can help to verify the homogeneity of SDA samples. In Ti-Al based alloys, there is an important intermetallic phase, TiAl gamma phase, which is quite brittle. XRD can indicate what phases existed in the sample and can quantify their fractions which can help to interpret the mechanical behaviour of the sample. XRD was performed using PHILIPS X' Pert X-ray diffractometer from 20° to 100°. The wavelength is 1.54056Å for Cu Kα radiation used in this experiment. Match! was used to analyse the data and identify the phases.

3.8 Hot Isolated Pressing (HIP)

Ti-Al based alloys tensile samples were HIPped at 1260 ^{0}C and 150 MPa for 4 hours before ETMT tests. The heat treatment was performed to homogenise the microstructure. The cast Ti-46Al-8Nb sample had also been HIPed under these conditions.

3.9 Video recording

There is a USB microscope camera on the SDA nozzle head, and it can be used to record the suspended droplets. These live videos can show if the wires are feeding properly and get melted together smoothly which is important for the operation of the machine and allows adjustment or the stopping of the process. However, as it takes only around 20 seconds for a suspended droplet to form and then be deposited it is hard to observe and investigate what is going on during the mixing in such a short video played with normal speed. A high speed camera was therefore used to show the process slowly and help get more details of the droplet formation, growth and release. The impact of the droplets to form splats took an even shorter time, typically 0.01-0.1 s. The recorded video was compared with a model of the splatting process.

FASTCAM Mini UX100 with 6X (18 - 108mm FL) C-Mount Close Focus Zoom Lens was set up outside the chamber to record high speed video. The videos of the droplets have a 1,280 horizontal by 720 vertical pixel resolutions at 4,000 frames per second (fps). The videos of the splats have a 1,280 x 1,000 pixel resolution to 4,000 fps.

3.10 Temperature measurement

The temperature has been measured using a Metis MQ22 pyrometer. The pyrometer was fixed in a small box and the box has a 50mm dia., 5mm thick, uncoated λ/10 Fused Silica Window on it. The window can transmit the wavelength of 1.45 µm - 1.8 µm but block the CO_2 laser in order to protect the pyrometer from the laser. The pyrometer can measure with two wavelength 1.45µm and 1.8µm, and the results measured with 1.8µm can be more accurate. The pyrometer was pointed at the droplet and the measurement started. Figure 3.13 shows the temperature variation when a pure Ti droplet was heated up by the laser beam and then cooled down.

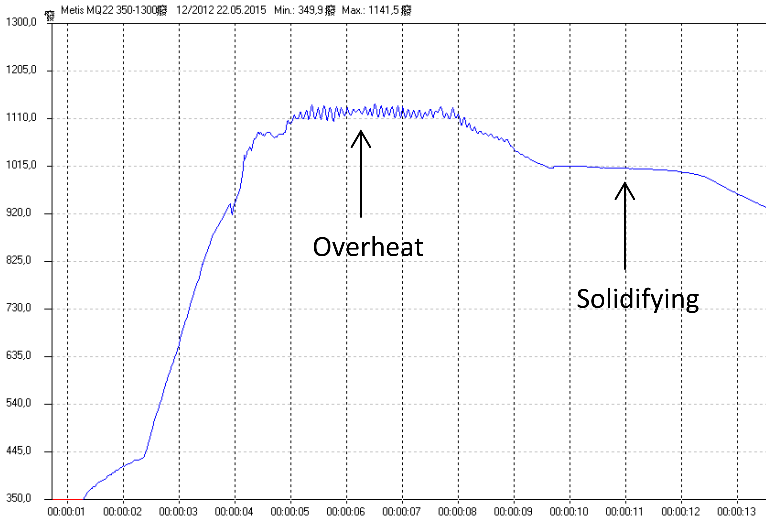

Figure 3.13 The temperature curve of a pure Ti droplet after heating and cooling

As Figure 3.11 shows, the associated software with the pyrometer only measures temperatures from 350°C to 1300°C, so the actual temperature was worked out using Ti's melting point as a reference. According to the Planck's law,

$$B_\lambda(\lambda, T) = \frac{2hc^2}{\lambda^5} \frac{1}{e^{\frac{hc}{\lambda k_B T}} - 1} \tag{1}$$

Because $B_\lambda(\lambda, T)$ was a constant value, it is known that:

$$\frac{1}{e^{\frac{hc}{\lambda k_B T_1}} - 1} = \varepsilon \times \frac{1}{e^{\frac{hc}{\lambda k_B T_2}} - 1} \tag{2}$$

In which T_1 is the measured temperature and T_2 is the actual temperature, and ε is the emissivity of the whole temperature measuring system. By putting the measured Ti droplet's melting temperature and the actual Ti melting point (known as 1668 °C) into the Equation 2, the emissivity of the whole temperature measuring system can be known. Then putting the measured overheated temperature of Ti droplet and ε into the Equation 2 again, the actual temperature of the Ti droplet can be calculated.

3.11 Modelling

One form of the SDA samples is splats, the deposition of a single droplet. The splats can be analysed in a similar way to the cut 1 mm thick discs, and are much easier to produce. In order to produce the splats as flat as possible some modelling work was undertaken to have a better understanding of their formation.

The program SimDrop was used to simulate the formation of splats. It is a simulation software supplied by Simulent to analyse various droplet impact scenarios. The simulation can indicate the predicted splat size and thickness. To set up SimDrop for the simulation the droplet material, droplet characterization, type of surface, interface properties and substrate properties where inputted.

The general setting including the maximum time step, Δt and the total simulation time. It can be calculated according to the equation: $\Delta t < (R_0 / CPR) / V_0$, where R_0 and V_0 are the initial radius and velocity of the droplet, and CPR are Cell Per Radius which is an indication of the grid size and the optimized number for it is 15. The time interval, T_{plot} for the output files also needed to be determined as it determines how many output files are generate. It is recommended setting based on the equation: $T_{plot} \leq 0.1D_0/V_0$, where D_0 is the diameter of the initial droplet. Boundary condition, thermal boundary condition and grid are also need to determine.

The droplet's initial temperature, diameter, velocity and distance to the substrate were required as inputs to the software. Though the software provides property files for several materials but these did not include the titanium used in this work. Therefore a titanium data file was created based on the density, melting point, heat of fusion and the liquid phase kinematic viscosity, thermal conductivity, specific heat and surface tension of Ti at different temperatures.

The substrate properties need to be defined as well, including the initial temperature and the thermal resistance between the solid and substrate. In thermal spray processes the thermal resistance between the solid and substrate is typically between 1×10^{-7} m^2-K/W (for room temperature substrates) to 1×10^{-6} m^2-K/W (for higher temperature substrates).

There are also several materials’ property files for selection. In our case, the droplets were deposited on Cu plate directly to form splats, so the Cu file was selected.

After all the input data is ready, the simulation was started. The result of the simulation is a series of f (volume of fluid) files. Using the software Tecplot 360, these f files could be translated into a video that simulates the formation of the splat.

3.12 Oxygen content Measurement

Ti and Al are both active elements that can be easily oxidized and form brittle oxides. Therefore the SDA process was performed in the argon filled glove box with an oxygen level of 20-50 ppm. There is also nozzle gas (argon) near the suspended droplet to protect the atmosphere and equipment. The oxygen content of as-cast Ti-46Al-8Nb and SDA Ti-46Al-8Nb was measure at Incotest by the LECO method to see how oxygen influences SDA samples.

3.13 References

Hauptstein, B., *Accelerated systematic exploration of superconductivity in Niobium alloys using a novel laser deposition technique (Unpublished)*, 2014, University Of Birmingham.

CHAPTER 4: SDA OF Ti-Al BASED ALLOYS

This chapter investigates the potential of the new SDA technique to produce bulk alloy samples rapidly and with the target composition. Three alloy systems have been studied: Ti-Al-Fe, Ti Al-V and Ti-Al-Nb. Among all these three systems, Ti-Al-Nb is the most challenging system to make due to the high melt point of Nb, and therefore a further development of the process based on Ti-Al-Nb was carried out. SDA splats are also been introduced and investigated based on the requirements from other AccMet partners (SDA sample users).

4.1 Introduction

Based on the combinatorial concept of the AccMet project, a large number of alloy samples are to be fabricated and go through a series of high-throughput characterisation tests. SDA has been developed as a new combinatorial synthesis process to meet these requirements. The advantage of SDA is the rapid production of bulk alloy samples. As a bulk alloy sample is produced, rather than just a thin film, it means that mechanical property characterisation can be undertaken with more confidence.

The SDA process is a development of Direct Laser Fabrication (DLF). DLF commonly uses powder feedstock delivered to the process head where it is introduced into the melt pool created by the laser beam. A sample produced by DLF will have a composition similar to the feedstock powder from which is made, which is normally pre-alloyed. To produce a series of different alloy samples either a series of pre-alloyed feedstock would be required (very expensive) or a series of powders would need to be pre-mixed. Pre-mixing blends of powder is a time consuming step and therefore not suited to the combinatorial synthesis. Delivering different powders from individual powder feeders to the processing has the potential to speed up the mixing process but has the disadvantage that powder feeder systems are expensive and not suited to a wide range of delivery rates. SDA overcomes these limitations by using a multiwire feeding system. All fed wires can be melted into the sample, and the sample's composition can be simply controlled by adjusting the feeding rate of each wire. Table 1.1 compares DLF powder-feed system and SDA wire-feed system to show the advantages of SDA wire-feed system. The main limitation of SDA is the restricted range of wire feedstock available.

This work is aimed at using SDA to make homogeneous alloy samples. Initially the binary alloy system Fe-Al was studied and different wire feed patterns investigated. All the wires are melted into an alloyed droplet above the melting pool as this was found to be the most effective way to get homogeneous samples. Ternary systems were then investigated. For the first few ternary systems, 0.5 mm metal wires were used.

Various Ti-Al-Fe and Ti-Al-V samples were made according to the requirements of the AccMet project. Standardised EDS mapping was operated on a Hitachi TM3000 SEM to check the homogeneity of these samples. All the homogeneous samples were marked with a unique AccMet number and send to various project partners for further tests. All the results were uploaded to an online database called the Virtual Alloy Library with the help of GRANTA. Through this work Cardiff University has identified a Ti-Al-Fe composition as a promising thermoelectric ternary system based on the samples produced. (García-Cañadas, Adkins et al. 2016)

Ti-Al-Nb is a more difficult system than Ti-Al-Fe and Ti-Al-V to process because of the high melting point of the element Nb (2469 °C), which is similar to the boiling point of Al (2470 °C). Therefore, the main part of the work here explored the optimisation of the SDA method to make homogeneous Ti-Al-Nb samples. Different inhomogeneities in Ti-Al-Nb samples are discussed and the causes of these inhomogeneities were discussed based on the formation of the droplets and the consistency of the deposited droplets. A microscope camera and a high speed camera were used to observe the SDA process including the formation of the droplets and the growth of the melting pool. Finally, a process guide developed to indicate the best way to produce Ti-Al-Nb samples according to the composition required. The guide includes the selection of wires with different diameter and the position of the wires. The influence of the process parameters were also studied based on Ti-Al-Nb. With this study the possibility to fabricate homogeneous alloy bulk samples using SDA has been enhanced significantly.

During the AccMet project, a large number of samples were produced for the project partners according to their requirements. Some of the partners are in charge of testing functional properties like superconductivity and thermoelectricity. These samples usually had complex compositions but do not require a large sample size. By allowing an alloy droplet to impact onto a massive substrate a sample in the form of a splat is produced. A Ti-46Al-8Nb splat has been characterised. High speed photography of splats of pure Ti droplets and the simulation software, SimDrop, are used to study the splatting process and the parameters that affect it.

4.2 Ti-Al-V ternary system

Ti-Al-V samples were made using Ti, Al, and V wires with a diameter of 0.5 mm. For general ternary alloy systems, the range of samples produced has target compositions dispersed uniformly across the whole phase diagram. Each sample has a 10 at.% difference compared to the other samples. The target compositions of Ti-Al-V have been shown in Figure 4.1. Binary systems Ti-V and Al-V are also included.

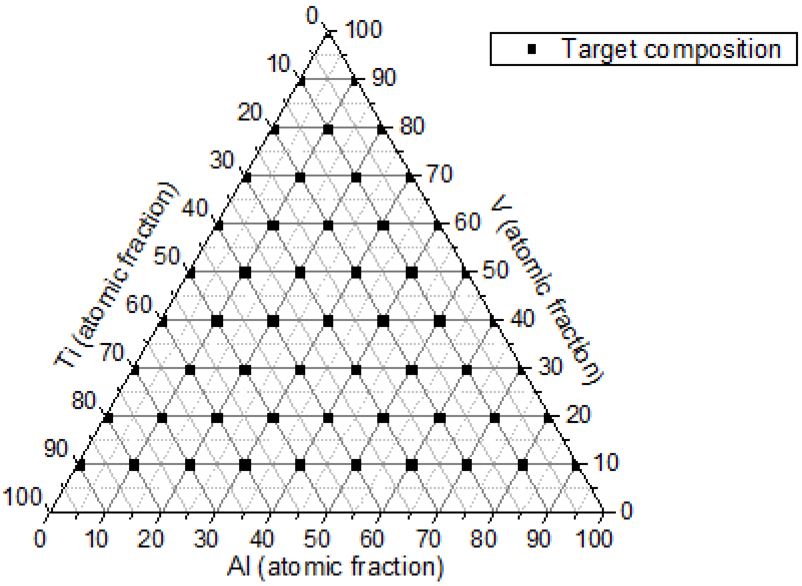

Figure 4.1 Ti-Al-V samples with different composition formulations spread in the ternary diagram

In the first trial, 44 samples were made, and 31 samples were confirmed as homogeneous samples by EDX, the analysis results are shown in Figure 4.2. The black dots are the 44 samples produced and their target composition. The red dots are the 31 homogeneous samples and their EDX results. The homogeneous samples have an EDX result close to their corresponding target composition.

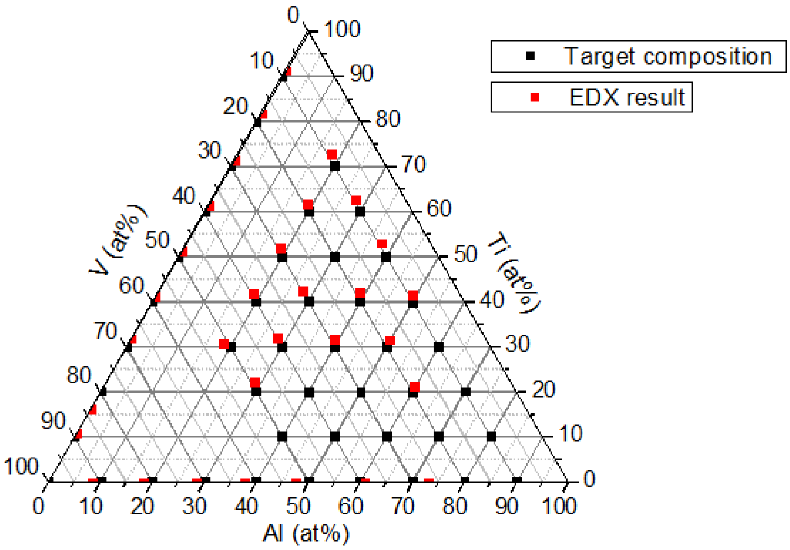

Figure 4.2 Ti-Al-V samples with different composition formulations and its relative EDX result in the ternary diagram

The general characterization of the SDA samples was mainly focused on the chemical segregation and any inclusions first. If the constituent elements are distributed uniformly in a sample and the sample has no particle inclusions then the sample was regarded as homogeneous and suitable for further characterisation. Most of the samples are fully dense, though some have some small pores. Samples with pores but with a uniform distribution of elements are still considered acceptable. A typical homogeneous Ti-Al-V sample is shown in Figure 4.3. For a sample’s EDX mapping, TM3000 provides a back-scattered image, individual elements' distribution images and the overlay of the back-scattered image and all elements' distributions images. In Figure 4.3 the Ti distribution in the sample, the left side has more dots than the right side, but it is not due to the distribution of Ti in the sample. Since the same phenomenon can be also observed in Al and V distributions, this is due to the system error, like the misalignment of the beam. The sample itself is still homogeneous. The sample's target composition and EDX result is shown in Table 4.1.

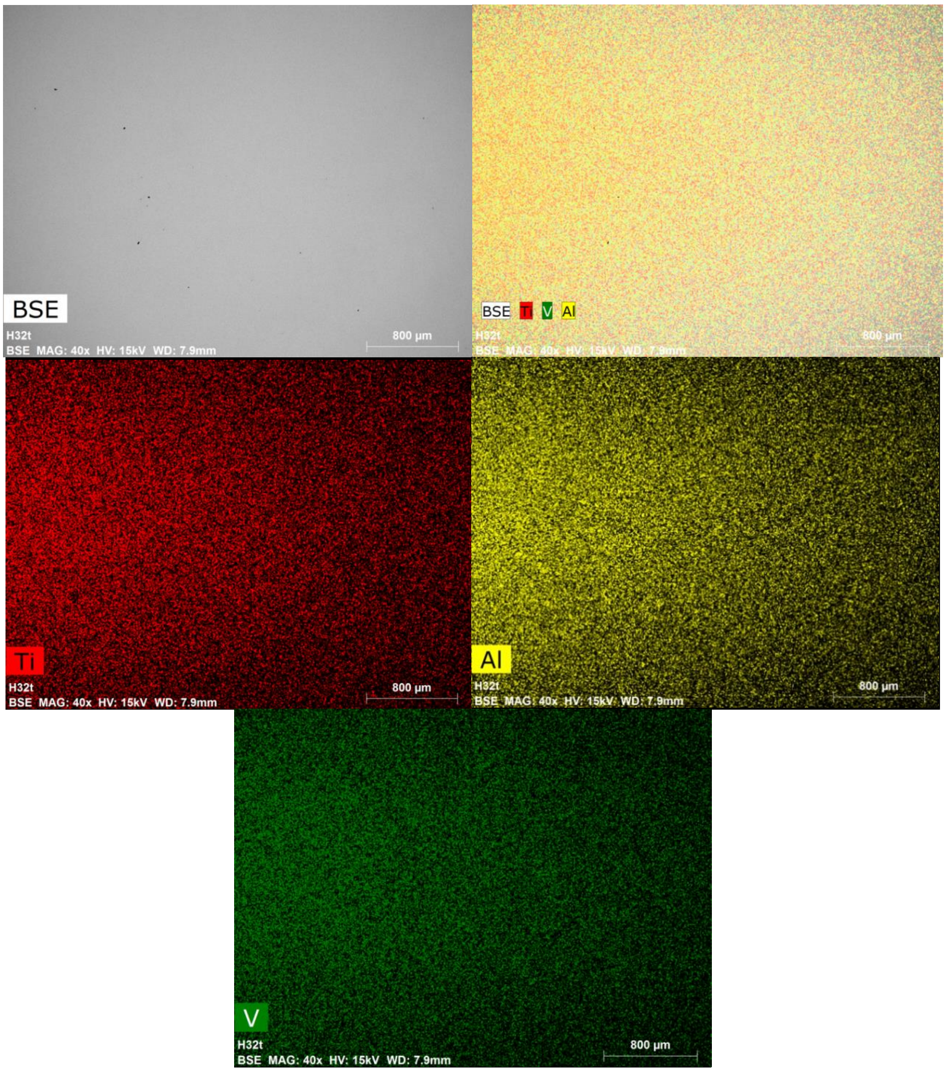

Figure 4.3 The EDX mapping of 30Ti-40Al-30V

Table 4.1 30Ti-40Al-30V's comparison of target composition and EDX result (all in atomic fraction)

	Ti	Al	V
Target composition	30.02	40.03	29.95
EDX result	31.90	38.98	29.12

4.3 Ti-Al-Fe ternary system

Ti-Al-Fe samples were made using Ti, Al and Fe wires with a diameter of 0.5 mm. Like Ti-Al-V, the target compositions of Ti-Al-Fe are dispersed uniformly across the whole phase diagram. Binary systems Ti-Al, Ti-Fe and Fe-Al are included in the system, and even pure Ti, Al and Fe samples were produced. 78 samples have been made which can be found as black dots in Figure 4.4, and some of the compositions have been made twice even three times. 62 samples have been found to be well alloyed and have homogeneous microstructure which is shown as red dots in Figure 4.4.

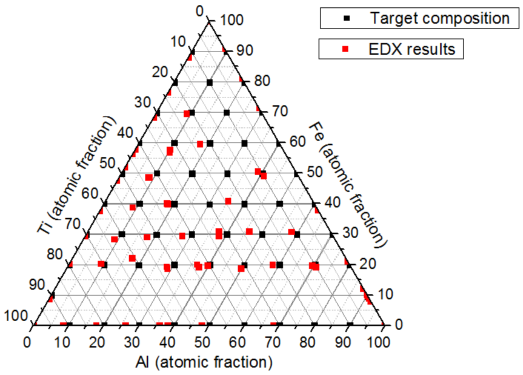

Figure 4.4 Ti-Al-Fe samples with different composition formulations and its relative EDX result in the ternary diagram

The sample 20Ti-60Al-20Fe is selected to illustrate a homogeneous Ti-Al-Fe ternary sample (shown in Figure 4.5). The sample 50Ti-50Al is chosen to demonstrate a homogeneous Ti-Al binary samples (as shown in Figure 4.6) and 90Al-10Fe as an example of a homogeneous Al-Fe binary sample (as shown in Figure 4.7). Several phases can be observed in the back-scattered images of the 20Ti-60Al-20Fe and 90Al-10Fe samples. The comparisons of target compositions and EDX results of 20Ti-60Al-20Fe, 50Ti-50Al and 90Al-10Fe are listed in Table 4.2.

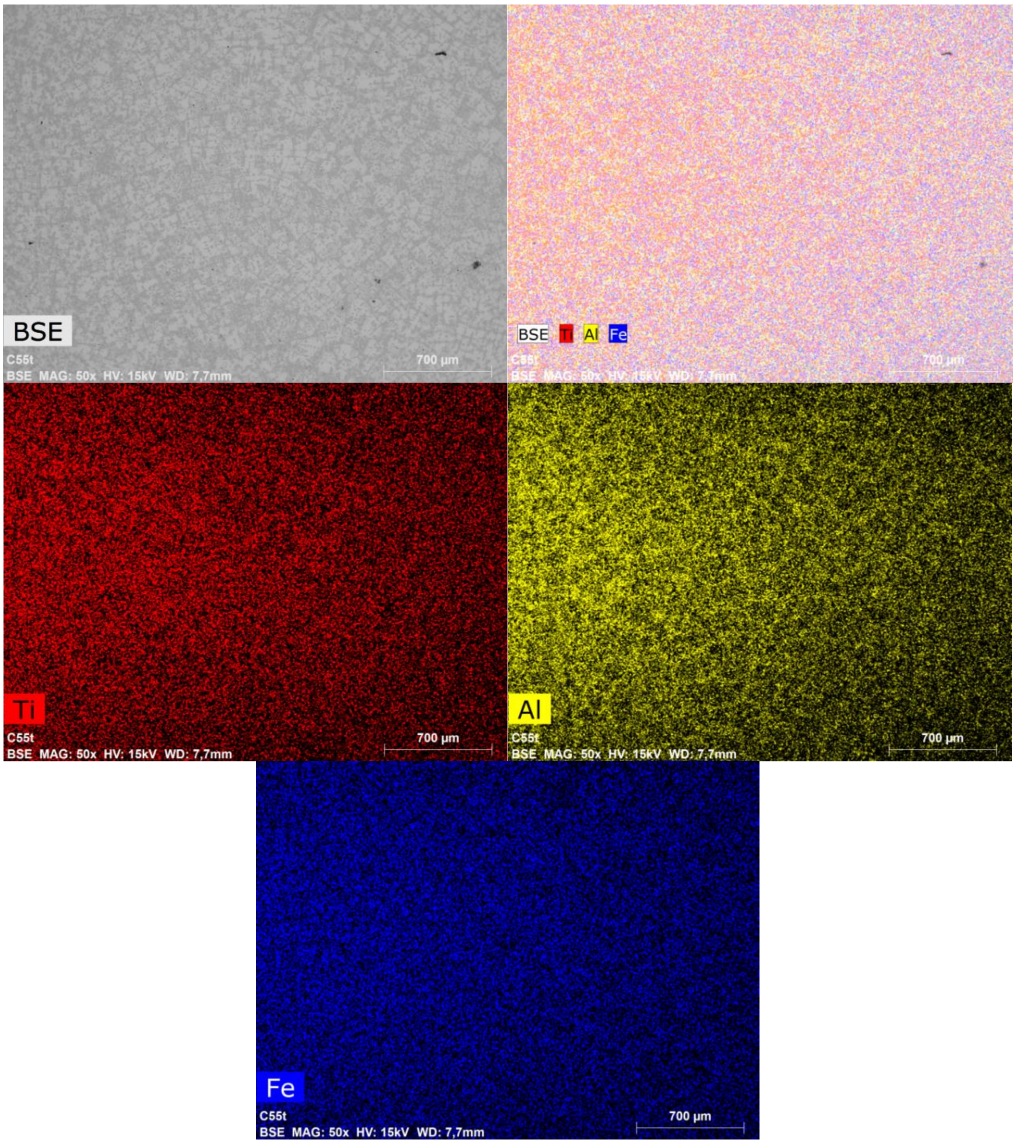

Figure 4.5 The EDX mapping of 20Ti-60Al-20Fe

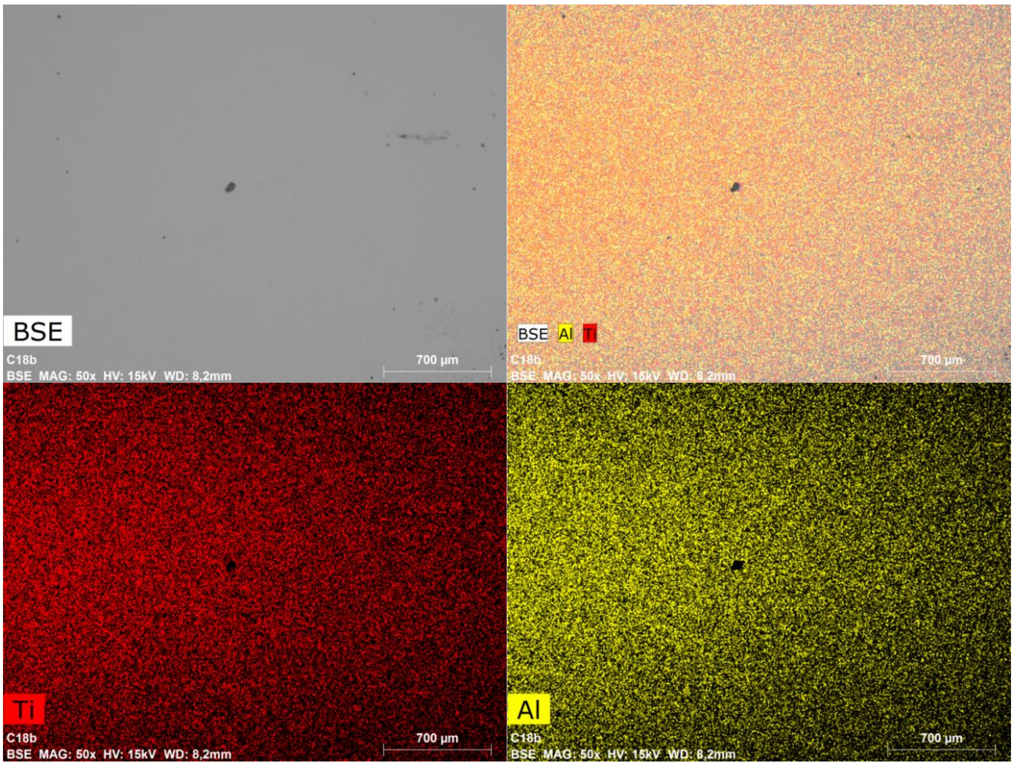

Figure 4.6 The EDX mapping of 50Ti-50Al

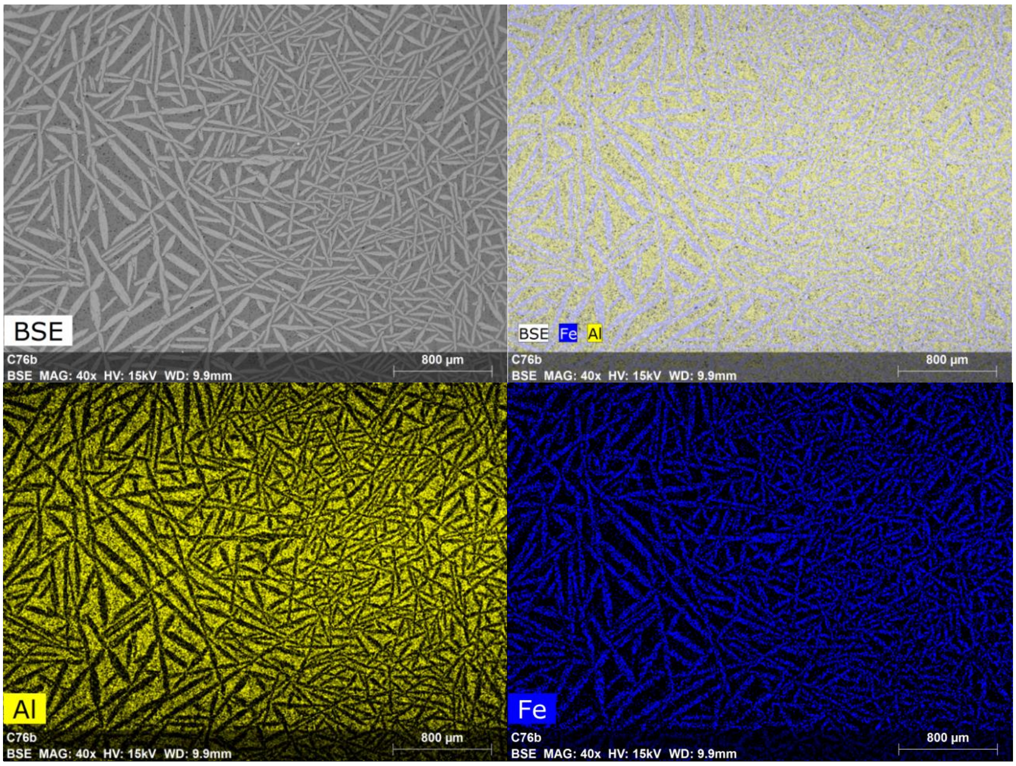

Figure 4.7 The EDX mapping of 90Al-10Fe

Table 4.2 The comparisons of target compositions and EDX results of 20Ti-60Al-20Fe, 50Ti-50Al and 90Al-10Fe (all in atomic fraction)

		Ti	Al	Fe
20Ti-60Al-20Fe	Target composition	20.00	59.97	20.03
	EDX result	21.92	20.02	58.06
50Ti-50Al	Target composition	49.99	50.01	-
	EDX result	52.06	47.94	-
90Al-10Fe	Target composition	-	89.99	10.01
	EDX result	-	90.32	9.68

High-throughput power factor measurements were carried out on these Ti-Al-Fe samples by Cardiff University. The power factor can be regarded as the main indicator of the thermoelectric performance of the material. They found certain compositions in the Ti-Al-Fe system showed potential as a thermoelectric material, so more Ti-Al-Fe samples were produced with small element difference around the composition of interest. The results are shown in Figure 4.8. Among all these Ti-Al-Fe ternary samples, the highest power factor of 13.3 × 10^{-4} W/m K^2 is achieved which is lower but comparable to those of the current high temperature thermoelectric materials like Bi_2Te_3 based alloys (about 30 × 10^{-4} W/m K^2) (García-Cañadas, Adkins et al. 2016).

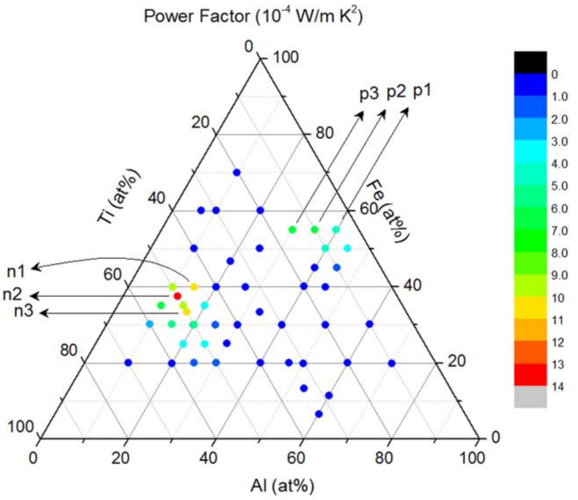

Figure 4.8 Thermoelectric screening results of the power factor of the Al−Fe−Ti ternary system. Samples p1−p3 and n1−n3 are the best p- and n-type specimens discovered, respectively (García-Cañadas, Adkins et al. 2016).

4.4 Virtual Alloy Library

Virtual Alloy Library (as shown in Figure 4.9) is the Accelerated Metallurgy database, an important part in AccMet project. There are many partners in the project, and each organisation has different tasks. For example, samples fabrication and EDX checking was undertaken by University of Birmingham, and the following high-throughput power factor measurement is carried out by Cardiff University, and so on. All the data for a sample was then uploaded onto the database by the various partners. Most of the samples in the database are for ternary and binary alloys, but it also has a significant number of alloys with 4 or even 5 elements.

Welcome to the Accelerated Metallurgy project Metals & Alloy Data system. Three databases are available on the system:

- The **Virtual Alloy Library** is a dedicated data repository intended to capture all alloy data generated as part of the Accelerated Metallurgy project, such as specimen compositions (planned, nominal or measured), manufacturing conditions, raw material supplies, testing facilities, test results or modelling predictions.
- The **Generic Materials Data** is a generic materials data source for materials scientists and engineers. Its contents largely revolve around the MaterialUniverse table, a set of complete, normalized, generic datasheets allowing comparison and selection for metals, ceramics, polymers, composites, and natural materials. It contains linked data on restricted substances and the legislation that affects them.
- The **Critical Materials** database is a reference source which helps to identify and understand supply risk for the materials based on factors such as geopolitical risk, physical scarcity, conflict mineral risk, and price volatility."

Search for information within Virtual Alloy Library:

Search for data in
All Data ▾

Figure 4.9 The interface of Virtual Alloy Library

Each sample with different composition has a unique AccMet number in the database. The 60Ti-20Al-20Nb sample for instance, has the AccMet number is UBS000082. The database has the hardness, thermoelectric power factor, simulated properties (in Figure 4.10.a), the EDX result (in Figure 4.10.b) and the XRD trace (in Figure 4.10.c).

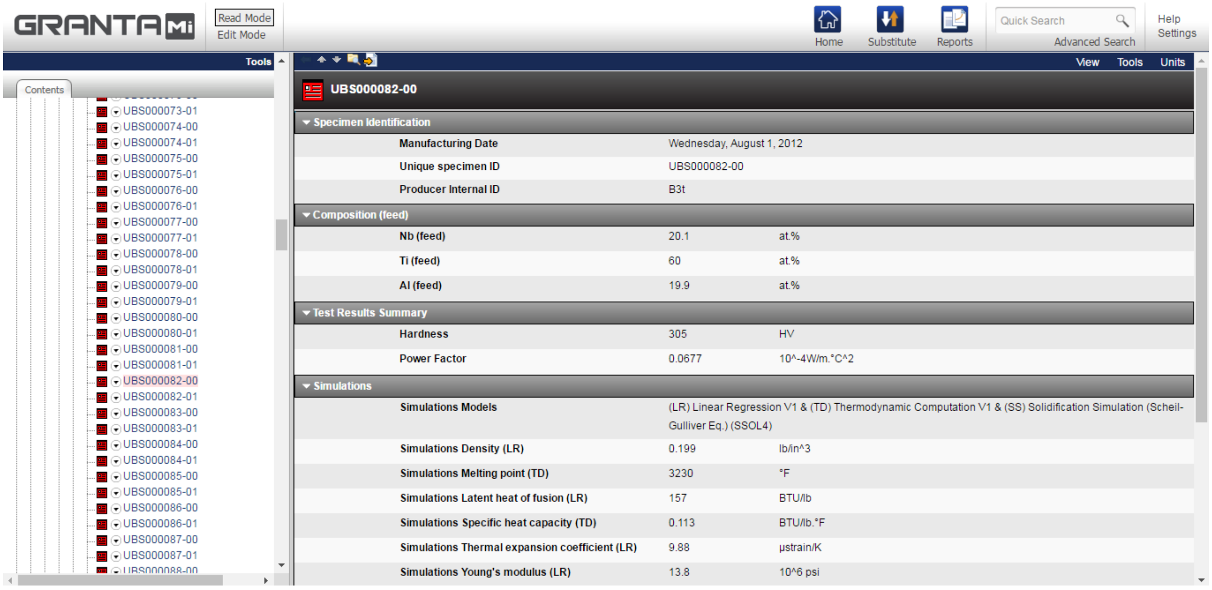

UBS000082-00

Specimen Identification

Manufacturing Date	Wednesday, August 1, 2012
Unique specimen ID	UBS000082-00
Producer Internal ID	B3t

Composition (feed)

Nb (feed)	20.1	at.%
Ti (feed)	60	at.%
Al (feed)	19.9	at.%

Test Results Summary

Hardness	305	HV
Power Factor	0.0677	10^-4W/m.°C^2

Simulations

Simulations Models	(LR) Linear Regression V1 & (TD) Thermodynamic Computation V1 & (SS) Solidification Simulation (Scheil-Gulliver Eq.) (SSOL4)	
Simulations Density (LR)	0.199	lb/in^3
Simulations Melting point (TD)	3230	°F
Simulations Latent heat of fusion (LR)	157	BTU/lb
Simulations Specific heat capacity (TD)	0.113	BTU/lb.°F
Simulations Thermal expansion coefficient (LR)	9.88	µstrain/K
Simulations Young's modulus (LR)	13.8	10^6 psi

a

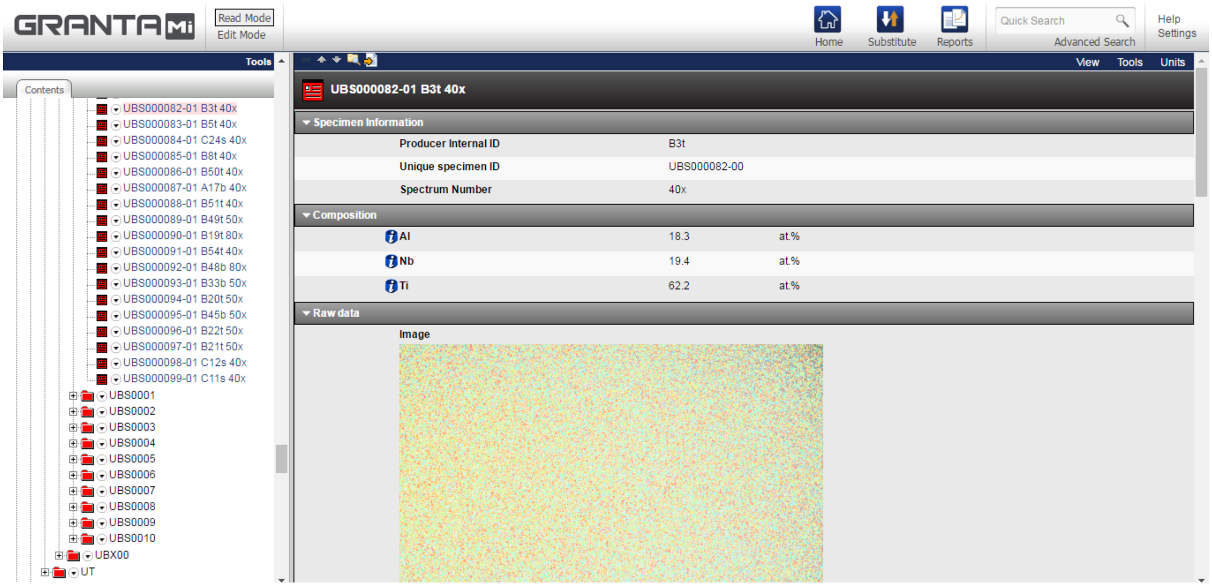

UBS000082-01 B3t 40x

Specimen Information

Producer Internal ID	B3t
Unique specimen ID	UBS000082-00
Spectrum Number	40x

Composition

Al	18.3	at.%
Nb	19.4	at.%
Ti	62.2	at.%

Raw data

Image

b

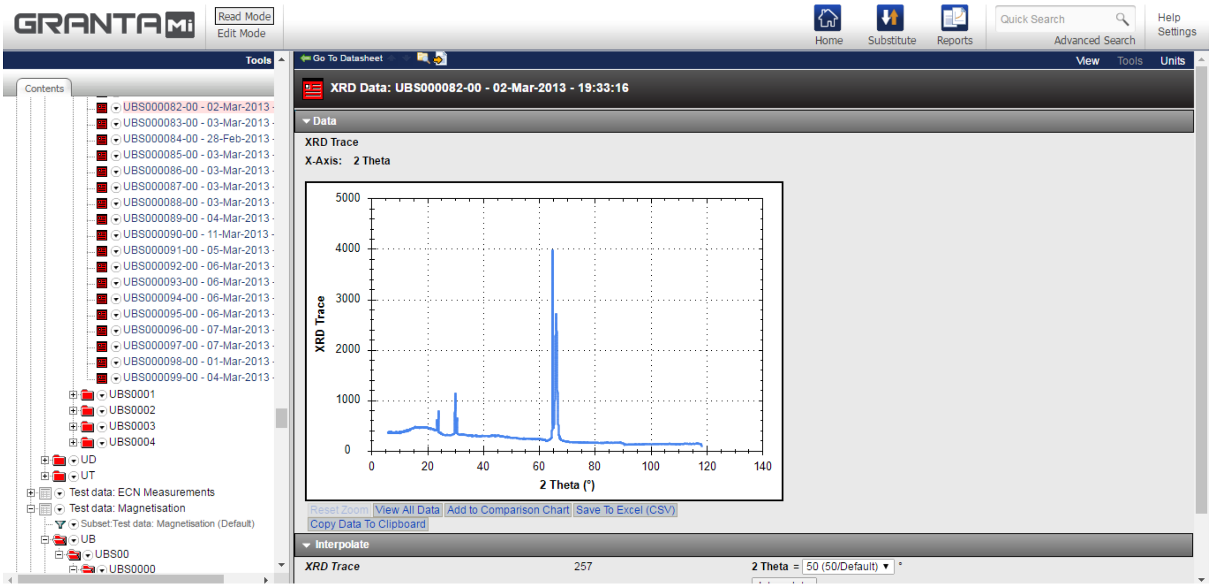

XRD Data: UBS000082-00 - 02-Mar-2013 - 19:33:16

XRD Trace
X-Axis: 2 Theta

XRD Trace 257 2 Theta = 50 (50/Default) °

c

Figure 4.10 60Ti-20Al-20Nb in Virtual Alloy Library, a) summary information about 60Ti-20Al-20Nb (including fabrication date, AccMet number, target composition, hardness, power factor and simulation properties); b) EDX results of 60Ti-20Al-20Nb; c) XRD result of 60Ti-20Al-20Nb

4.5 Ti-Al-Nb ternary system

4.5.1 Investigation of the inhomogeneity of the Ti-Al-Nb samples

At the beginning, Ti, Al, Nb wires with a diameter of 0.5 mm were used to make the samples. There are 72 samples with target compositions in the system. However during the process deposition for some specific compositions, the samples couldn’t be built up successfully because the difference between each wire feeding rate is too big (will be discussed in 4.5.8 wire selections). Moreover, some of the samples are very brittle, so they broke up during the EDM cutting. Hence, after cutting 50 samples remained for characterisation. The target compositions and the relative EDX result are shown in Figure 4.11.

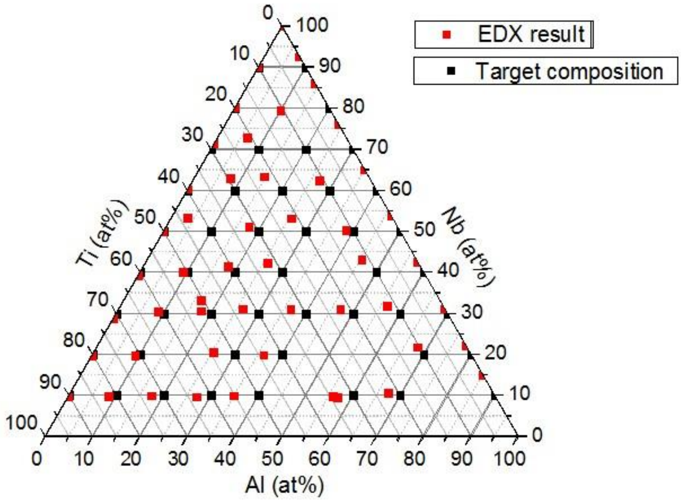

Figure 4.11 Ti-Al-Nb samples with different composition formulations and its relative EDX result in the ternary diagram

The homogeneity of the samples was investigated in three ways; a) chemical segregation, i.e. elements distributes uniformly; b) particles inclusions and c) variation in grain size. The initial screening was focused on the chemical segregation and inclusions. In the chemical segregation investigation 30 out of the 50 samples were found to be homogenous. For these 30 homogenous samples, most of them have a compositional difference less than 2 at.% compared to the target composition. Only a few samples' Al contents are around 5 at.% less than expected. The 20 samples were rejected from the EDX mapping results. The reason for rejection was found to be due to four different defects: (1) the presence of Nb-rich particles, as seen in samples Ti-40Al-30Nb (Figure 4.12), Ti-60Al-30Nb, Ti-30Al-20Nb, Nb-60Al, Ti-40Al-10Nb, Ti-70Al-

10Nb, Ti-60Al-10Nb, and etc., (2) rings with slight compositional differences, as seen in Ti-20Al-70Nb, Ti-10Al-50Nb, Ti-80Nb, Ti-90Nb, Nb-80Al, Nb-50Al (Figure 4.13), (3) two parts have a slight compositional difference in Al content, like Ti-10Al-70Nb (Figure 4.14), (4) has Al-rich region, like Nb-10Al (Figure 4.15). The other 30 samples were found to have less that 1 at.% variation across the sample.

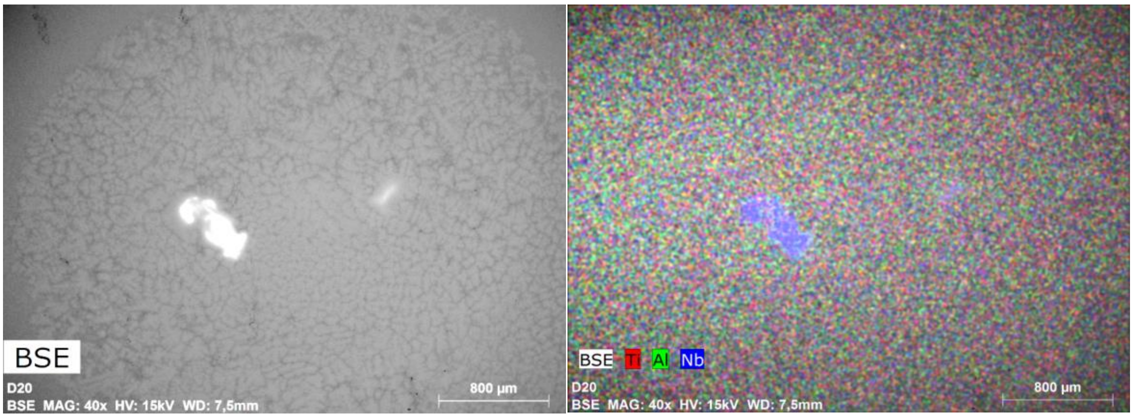

a

b

Figure 4.12 a) Ti-40Al-30Nb's Back-scattered Image, b) Ti-40Al-30Nb's mapping Image

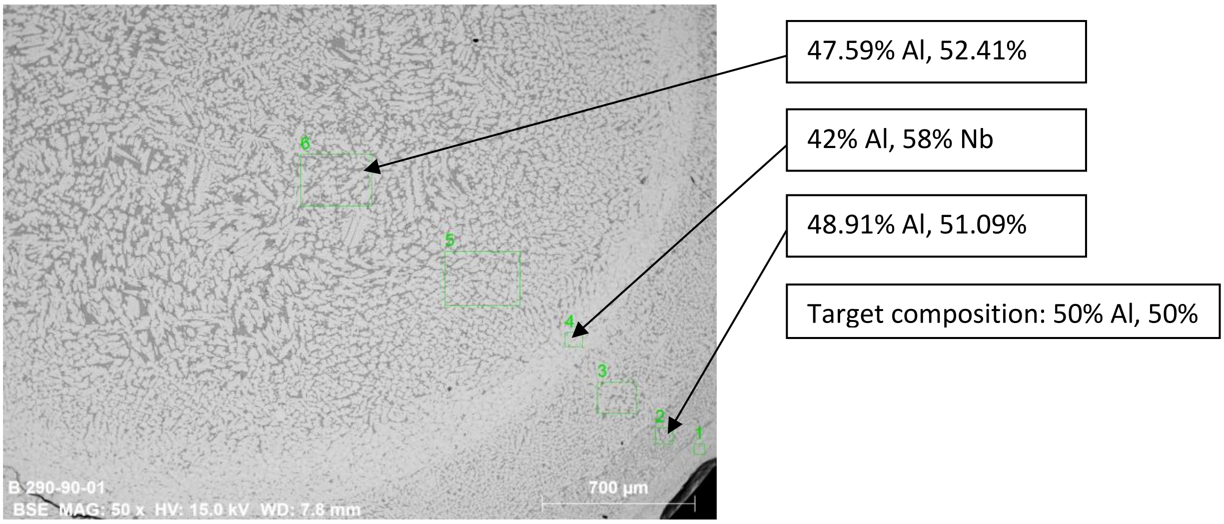

47.59% Al, 52.41%

42% Al, 58% Nb

48.91% Al, 51.09%

Target composition: 50% Al, 50%

Figure 4.13 Nb-50Al's Back-scattered Image and EDX result (all in at.%)

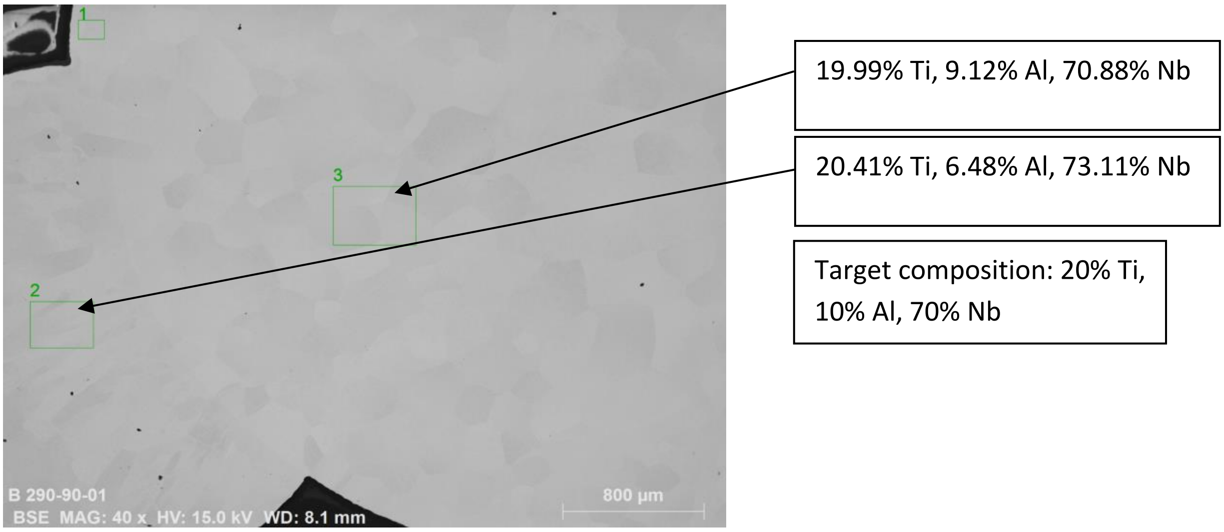

19.99% Ti, 9.12% Al, 70.88% Nb

20.41% Ti, 6.48% Al, 73.11% Nb

Target composition: 20% Ti, 10% Al, 70% Nb

Figure 4.14 Ti-10Al-70Nb's Back-scattered Image and EDX result (all in at.%)

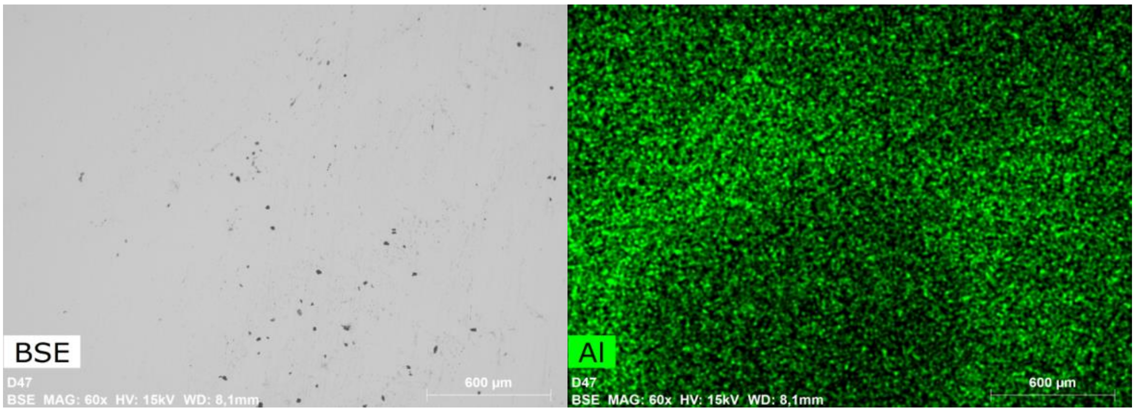

a

b

Figure 4.15 a) Nb-10Al's Back-scattered Image, b) Nb-10Al's Al mapping Image

4.5.2 Characterisation of Ti-Al-Nb samples

i. Microhardness test

Three samples (Nb-50Al, Ti-30Al-10Nb, and Ti-20Al-10Nb) have representative microstructures, so they will be discussed here. Nb-50Al as discussed above was found to be inhomogeneous, with several rings with slight compositional differences. Ti-30Al-10Nb is a homogeneous sample, but it has a clear variation of grain size from sample's edge to the centre. The grains get smaller when approach to the edge (shown in Figure 4.16). Ti-20Al-10Nb is quite homogeneous sample. It is not only compositional uniform, but also has no large difference in grain size. The optical microscope images of these samples after the test are shown in Figure 4.17 to see the arrangement of the indents. The microhardness test can measure Young's modulus E as well as the hardness of the sample. The result of Young's modulus E and hardness HV of three samples are shown in Figure 4.18.

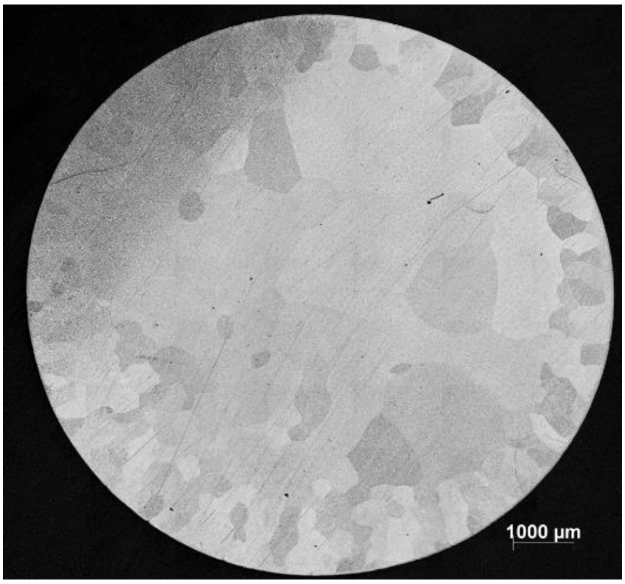

Figure 4.16 The optical microscope image of Ti-30Al-10Nb after etching

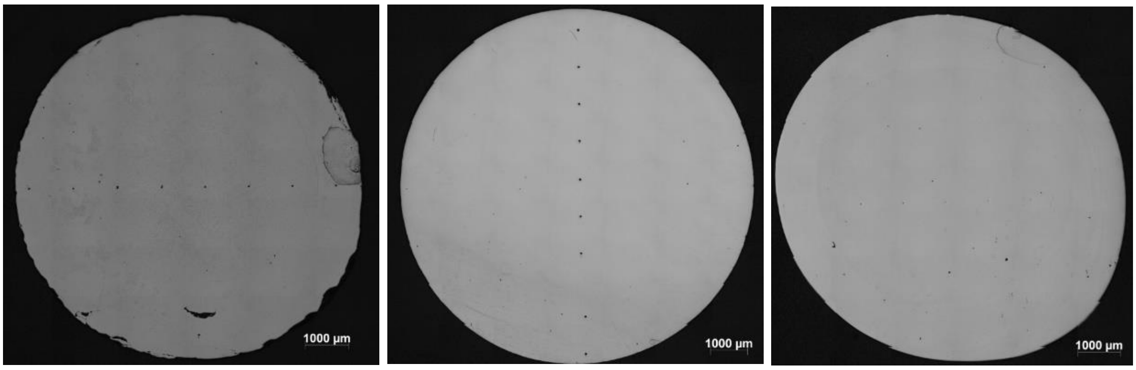

a b c

Figure 4.17 The optical microscope image of a) Nb-50Al, b) Ti-30Al-10Nb, c) Ti-20Al-10Nb after indentation

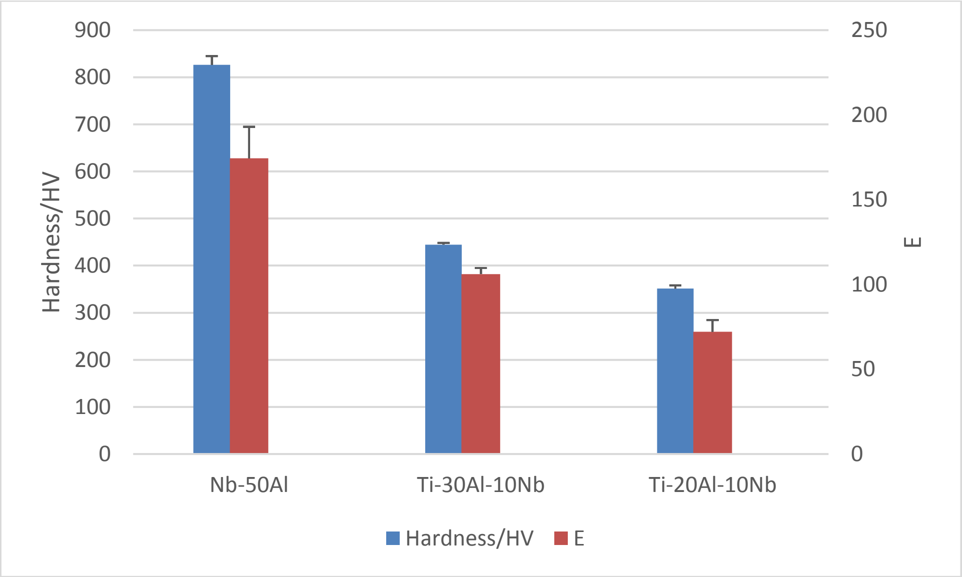

Figure 4.18 The result of Young's modulus E and hardness of Nb-50Al, Ti-30Al-10Nb, Ti-20Al-10Nb

ii. Compositional contour and hardness contour of Nb-50Al

Nb-50Al has several rings with slight compositional differences. Nb-50Al’s EDX was performed on Jeol 7000 using 25kV as accelerated voltage. As Figure 4.19 shows, area analyses for the whole image were carried with a magnification of 1000. Each area has a distance of 1 mm, so the analysis covered the whole sample. Hardness test used force was HV1, and each indent has a distance of 1 mm. The indents also cover the whole sample. The compositional contour and hardness contour of Nb-50Al are shown in Figure 4.20.

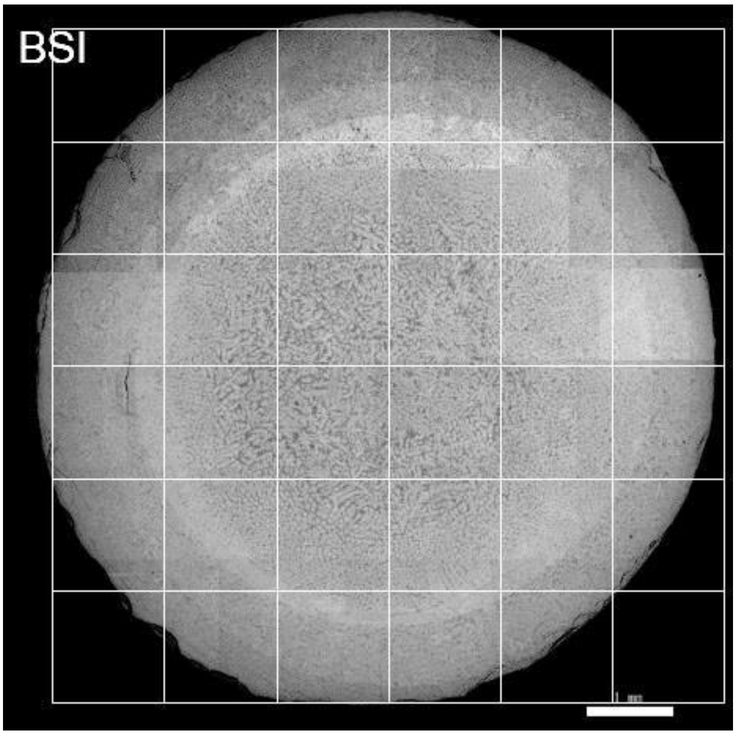

Figure 4.19 Back-scattered image of Nb-50Al.The squares can be roughly regarded as EDX analysis areas, and the cross spots can be seen as the hardness test points.

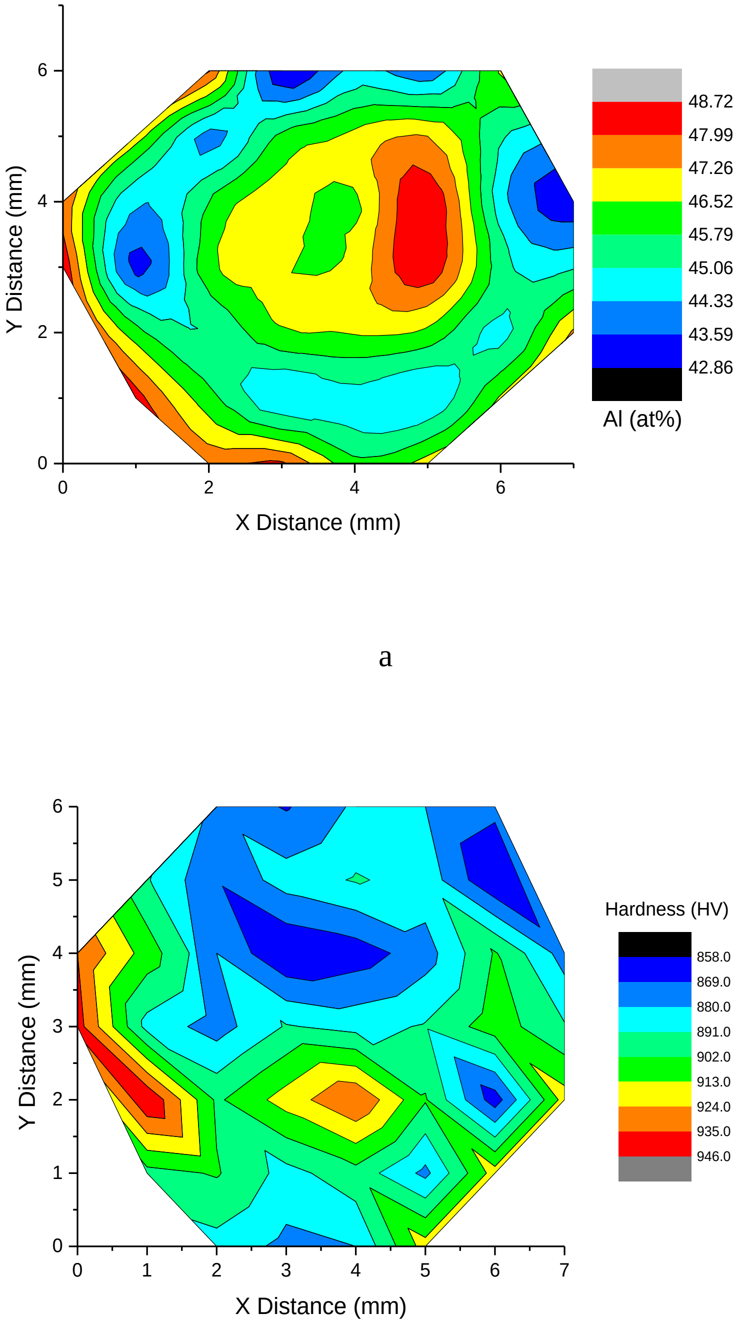

a

b

Figure 4.20 a) Al content compositional contour of Nb-50Al, b) hardness contour of Nb-50Al

Compared the compositional contour and hardness contour of Nb-50Al, the composition has a same ring effect like the microstructure shows, but the hardness is not showing the same ring. The influence of the composition on the hardness is therefore not significant.

However, when comparing the microhardness test results of Nb-50Al, Ti-30Al-10Nb and Ti-20Al-10Nb, the inhomogeneous sample Nb-50Al still has a larger standard deviation than other two homogeneous samples on both hardness and Young's modulus (shown in Figure 4.18). For these homogeneous samples, the hardness and Young's modulus across the whole sample varies in a small range.

iii. XRD result of Ti-30Al-10Nb and Ti-20Al-10Nb

Because Ti-30Al-10Nb and Ti-20Al-10Nb are regarded as quite successful and homogeneous samples among Ti-Al-Nb samples, XRD of them were taken to compare the phases using SDA and the phases under equilibrium condition. According to the XRD result, Ti-30Al-10Nb has α2, and O2 (Ti2NbAl) two phases and Ti-20Al-10Nb has α and α2. The XRD result is shown in Figure 4.21.

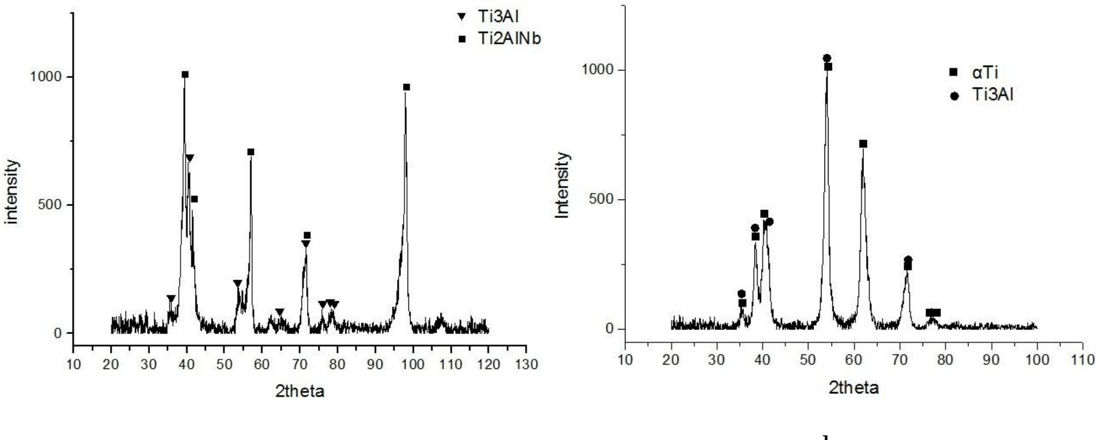

a b

Figure 4.21 XRD patterns of a) Ti-30Al-10Nb, b) Ti-20Al-10Nb

In terms of the equilibrium ternary phase diagram, Ti-30Al-10Nb has α2, O2 (Ti2NbAl) and τ (Ti4NbAl3) these three phases, and Ti-20Al-10Nb has α2 and O2. However, according to the XRD result, they have α2, O2 and α, α2 respectively. Although during the SDA process the samples' cooling rate is not as fast as the regular air cooling rate due to the fixed laser beam above the melting pool, it is still a non-equilibrium process. Therefore, the samples' phases may not be the same as the equilibrium phases predicted by the phase diagram. In some cases the samples may need to be heat treated prior to characterization to develop these equilibrium phases.

iv. Oxygen level of as-cast and SDA Ti-46Al-8Nb

Some of the samples were rejected because of cracking. Initially there was concern that this embrittlement may have been due to oxygen diffusion. (Wu, Huang et al. 2009) Therefore, oxygen level tests were performed on as-cast Ti-46Al-8Nb and SDA Ti-46Al-8Nb. However the measured oxygen content in SDA sample was only 610ppm, only slightly higher than a cast sample (550ppm) (see in Table 4.3). This oxygen content is low enough to ignore its embrittling effect to the sample. The brittleness is therefore not caused by oxygen diffusion. Instead it maybe because of too much internal stress introduced during the process, or that there are TiAl intermetallic phases in the samples like TiAl gamma phase (which was identified in Figure 5.4) which is quite brittle.

Table 4.3 Oxygen content in as-cast Ti-46Al-8Nb and SDA Ti-46Al-8Nb

	O in weight%
As-cast Ti-46Al-8Nb	0.055
SDA Ti-46Al-8Nb	0.061

4.5.3 Videos of 10Ti-10Al-80Nb with different wires

For Ti-Al-Nb samples with high Nb content, they usually have a high Nb wire feed rate as well, and the difference between Nb wire feed rate and Ti/Al wire feed rate is quite big. 10Ti-10Al-80Nb is a typical compositional formulation with high Nb content. Three SDA 10Ti-10Al-80Nb samples were made (or tried to make) with different wires to see how wires selections influence the process and the final products. There is only one kind of Nb wire with a diameter of 0.5 mm, while Ti and Al wires can either be with diameters of 0.5 mm or 1 mm. Wires with different diameters can lead to different feed rate which makes significant differences during wires mixing. Table 4.4 shows the possible wire selections for 10Ti-10Al-Nb and its relative wires feed rate.

Table 4.4 Possible wires choices for 10Ti-10Al-80Nb and its relative wires feed rate

Wires choices	Ti wire's feed rate	Al wire's feed rate	0.5 mm Nb wire's feed rate
1 mm Ti and 1 mm Al	15 mm/min	14 mm/min	485 mm/min
1 mm Ti and 0.5 mm Al	15 mm/min	56 mm/min	485 mm/min
0.5 mm Ti and 0.5 mm Al	59 mm/min	56 mm/min	485 mm/min

To make a SDA 10Ti-10Al-80Nb sample, 1 mm Ti and 1 mm Al wires cannot be picked at the same time, because both Ti and Al wire are feed too slow as 15 mm/min and 14 mm/min especially compared to the Nb's feed rate (485 mm/min), and it was too hard to form a suspended alloyed droplet. It requires that the three wires should meet together quickly during melting, and this is hard to achieve, so each wire was more likely to melt and deposit alone. As for 1 mm Ti and 0.5 mm Al wires, although Al wire's speed is fast enough to get alloyed by the droplet attached on Nb wire, Ti wire still too slow to touch the droplet in time. According to the video of SDA process recorded by the microscope near the nozzle head (shown in Figure 4.22), two deposition patterns can be concluded in terms of Ti wire's position while the last droplet has deposited. Because of high laser power and low Ti feed rate, Ti wire melts back once it gets close to the laser beam. The Ti wire would feed backward and forward regularly. Therefore, when a suspended droplet was about to drop, the Ti wire was either just melted back after feeding some Ti into the alloyed ball or just approached to the centre and with little Ti absorbed by the droplet (see in Figure 4.22). These two different situations may lead to two droplets with different Ti composition. This can be the cause of serial droplets with different compositions which lead to the inhomogeneity of the final product.

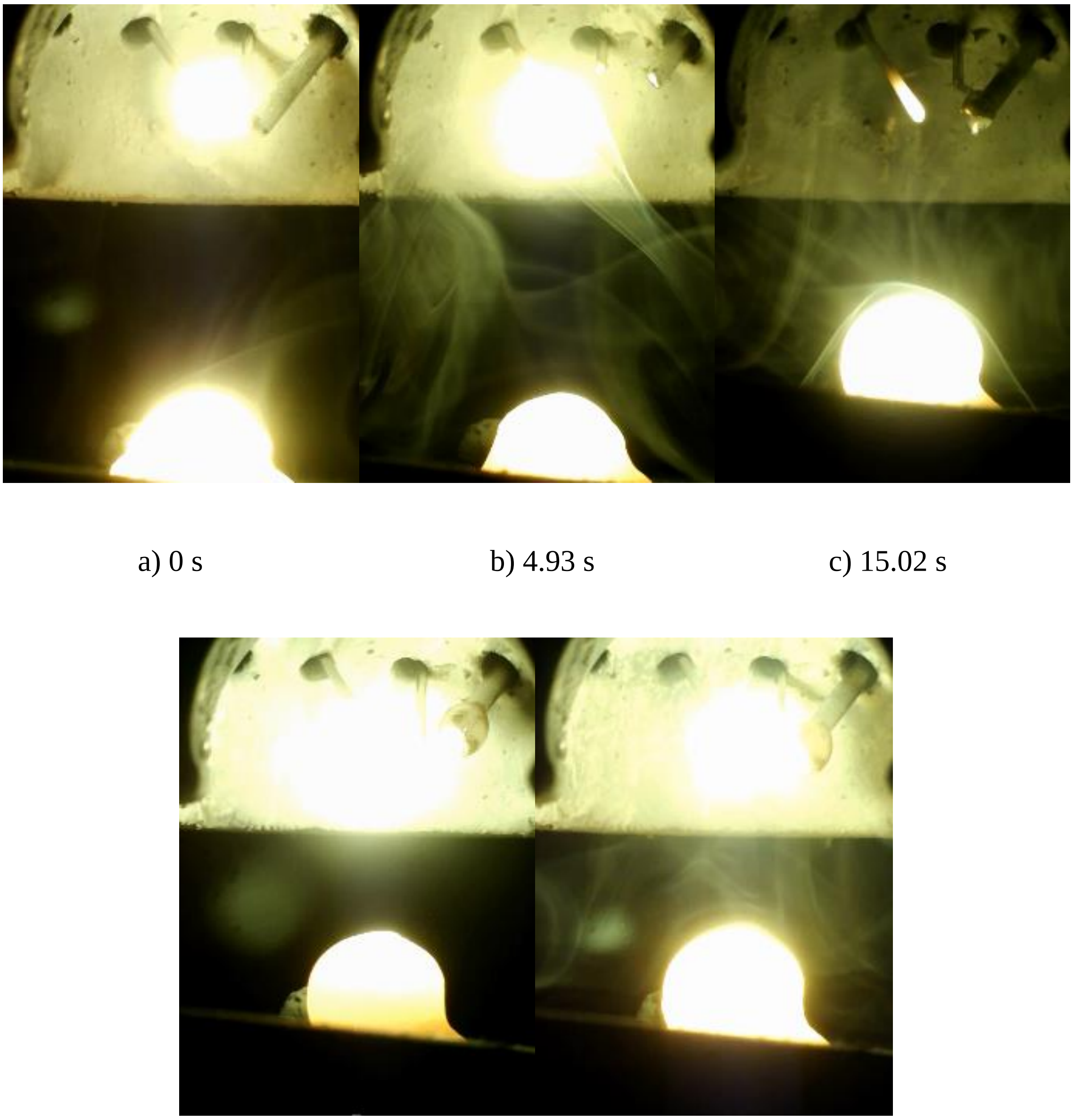

a) 0 s b) 4.93 s c) 15.02 s

d) 19.17 s e) 23.09 s

Figure 4.22 The SDA process of producing 10Ti-10Al-80Nb, and the wires from left to right are 0.5 mm Nb, 0.5 mm Al and 1 mm Ti.

Description of Figure 4.22: a droplet just fell into the melting pool at 0 s, and the Ti wire just approached the centre (a); then it touched with the ball attached to the Nb wire and melted back quickly (b); Ti wire fed toward the centre slowly, and at the same time the next droplet was large enough to drop off with the feed of Nb and Al (c); Nb and Al were fed together to form a new ball attached to the Nb wire, while Ti wire melted alone on the other side (d); the third droplet was fell off without the addition of Ti (e).

However, if the Ti wire was changed to 0.5 mm, the Ti wire would be melted back more easily. Moreover, the droplets that can be attached to the wires get smaller because of its surface tension which means the formation time of the droplets get shorter. It requires three wires meet together quickly during melting, and it is hard to achieve, so sometimes during the production of 10Ti-10Al-80Nb, the Ti and Nb formed their own balls, and dropped separately (as shown in Fig 4.23).

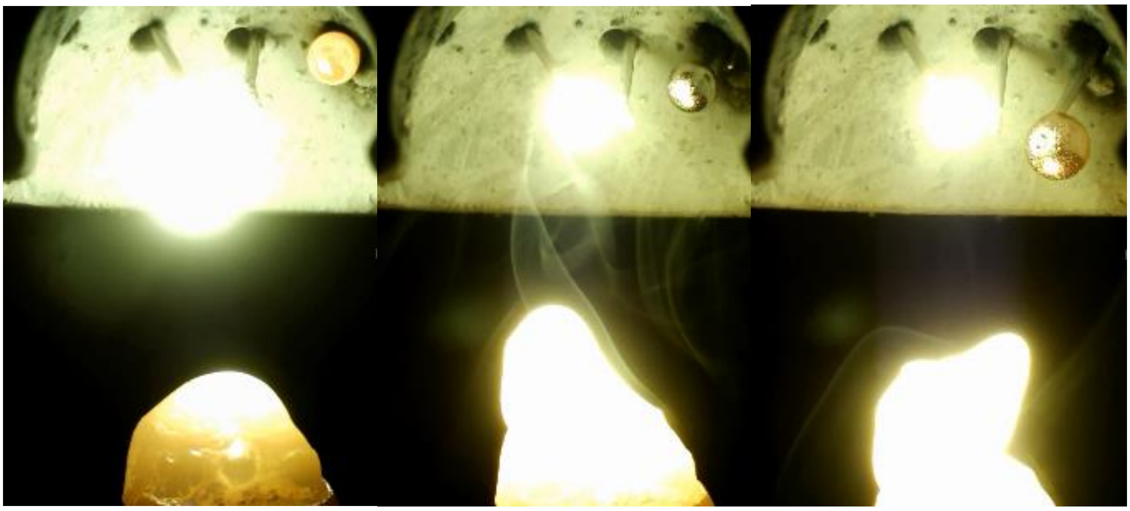

a) 0 s b) 1.21s c) 14.06 s

Figure 4.23 The SDA process of producing 10Ti-10Al-80Nb, and the wires from left to right are 0.5 mm Nb, 0.5 mm Al and 0.5 mm Ti.

Description of Figure 4.23: when three wires were feeding toward the laser beam, Ti suddenly melted back separately (a); an Nb, Al alloyed ball fell off without Ti (b); a second Nb, Al alloyed ball fell off, while Ti was still melt separately(c).

4.5.4 Videos of Ti-46Al-8Nb with different wires

Like 10Ti-10Al-80Nb, Ti-46Al-8Nb samples' processing videos were also been studied to find the most suitable wires to make Ti-46Al-8Nb samples. Some possible wires choices for Ti-46Al-8Nb and its relative wires feed rate are given in Table 4.5.

Table 4.5 Possible wires choices for Ti-46Al-8Nb and its relative wires feed rate

Wires choices	Ti wire's feed rate	Al wire's feed rate	0.5 mm Nb wire's feed rate
1 mm Ti and 1 mm Al	112 mm/min	105 mm/min	80 mm/min
1 mm Ti and 0.5 mm Al	110 mm/min	410 mm/min	78 mm/min
0.5 mm Ti and 0.5 mm Al	432 mm/min	406 mm/min	77 mm/min

If three wires were all 0.5 mm, Ti and Al wires' feed rates are quite high and above 400 mm/min, while Nb wire's feed rate is as low as 77 mm/min. The difference between three wires made Ti and Al melted together quickly and deposited into the melting pool while Nb was melted alone and slowly (see in Figure 4.24). After a few TiAl mixed droplets fall into the melting pool, an Nb ball can touch the suspended droplet attached on Ti wire to form a TiAlNb alloyed droplet that have a higher Nb content than expectation. Even though these droplets can get further mixed in the melting pool, the melting pool does not have the energy to homogenise the large composition differences in these droplets. Because the energy provided by the laser shooting from the top is mainly absorbed by the suspended droplet above the melting pool, and also the sample cannot be built up if the melting pool has too much energy. As a result, an inhomogeneous sample will be made. Moreover, since the Ti wire is as thin as 0.5 mm and the feed speed is as high as 400 mm/min, Ti wire can possibly miss the laser path a little bit which may cause Ti wire feed through the centre without melting (shown as Figure 4.25). Sometimes Ti wire was melted back immediately and kept the process moving, and sometimes it just feed away completely and made the process to start over again.

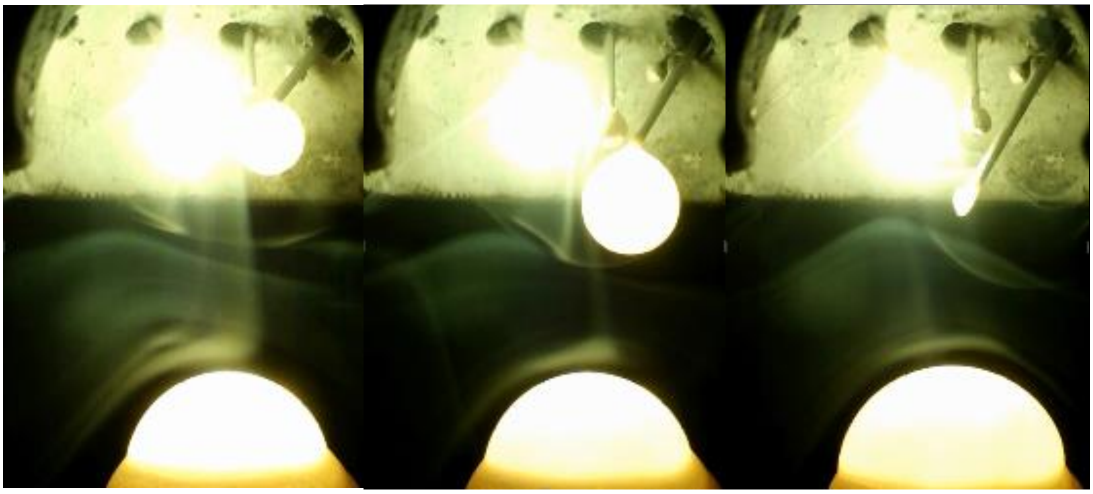

a) 0 s

b) 3.79 s

c) 4.22 s

Figure 4.24 The SDA process of producing Ti-46Al-8Nb, and the wires from left to right are 0.5 mm Nb, 0.5 mm Al and 0.5 mm Ti.

Description of Figure 4.24: three wires fed toward the laser beam, Ti and Nb each has a ball attached to it, and they are TiAl alloyed ball and pure Nb ball respectively (a); with time passed by, Al keeps touching the TiAl alloyed ball on Ti wire, TiAl alloyed ball and Nb ball grow larger and larger without meeting each other (b); TiAl alloyed ball was heavy enough and drop off, while Nb ball was still hanging on Nb wire (c).

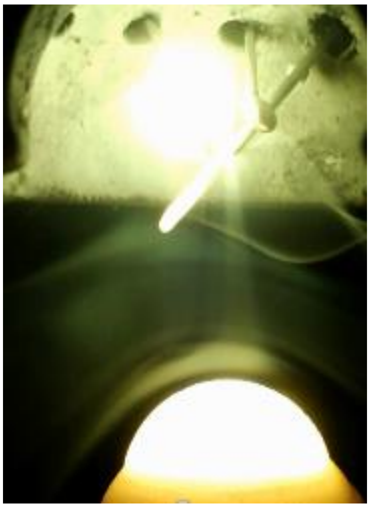

Figure 4.25 A screenshot of the SDA process of producing Ti-46Al-8Nb, and the wires from left to right are 0.5 mm Nb, 0.5 mm Al and 0.5 mm Ti.

Change of 0.5 mm Ti wire into 1 mm can help the Ti melt properly, but it does not improve the whole process. TiAl alloyed droplets still formed and deposited into the melting pool directly like the process with three 0.5 mm wires (see in Figure 4.26).

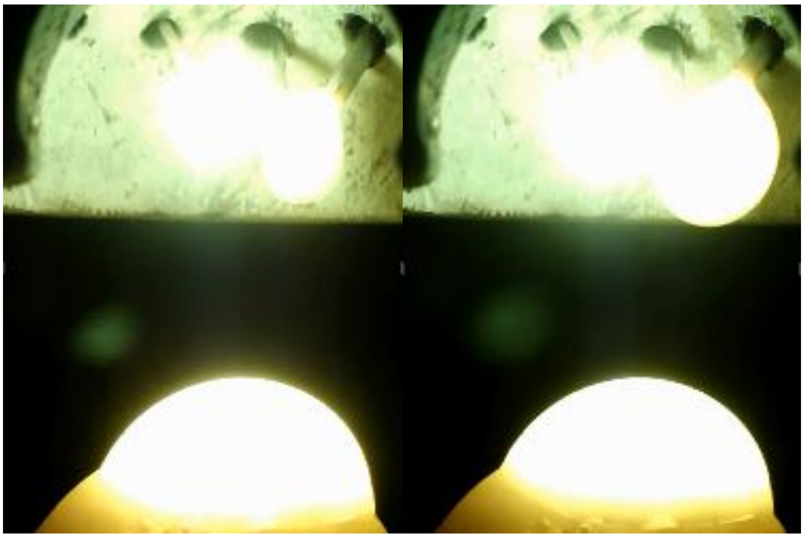

a) 0 s b) 6.32 s

c) 15.79 s d) 16.76 s

Figure 4.26 The SDA process of producing Ti-46Al-8Nb, and the wires from left to right are 0.5 mm Nb, 0.5 mm Al and 1 mm Ti.

Description of Figure 4.26: three wires fed toward the laser beam, Ti and Nb each has a ball attached to it, and Al was fed into the ball on Ti wire (a); balls grew especially the ball on Ti wire (b & c); TiAl alloyed ball on Ti wire dropped off, while Nb ball was still hanging on the Nb wire (d).

The wire selection of 1mm Ti, 1mm Al and 0.5mm Nb have a better performance than other choices (shown in Figure 4.27). This wire selection can provide a different feed pattern to form TiAlNb suspended droplets easily. The suspended droplet was attached to both Ti and Nb wires so that it can stay in the centre and get all three wires feed into the alloyed ball directly at the same time. Therefore, the droplet can suspend for a certain period and get fully mixed with three elements with target content, and then deposit into the melting pool.

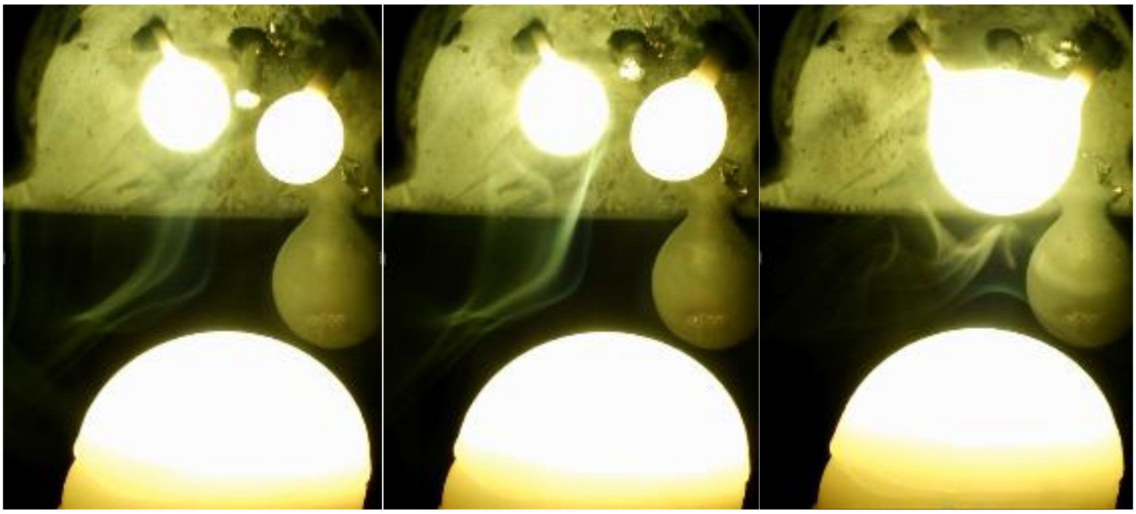

a) 0 s b) 1.1 s c) 7.39

Figure 4.27 The SDA process of producing Ti-46Al-8Nb, and the wires from left to right are 0.5 mm Nb, 1 mm Al and 1 mm Ti.

Description of Figure 4.27: three wires started to feed toward the laser beam, Ti and Nb wires are melted and form balls at the end of the wires (a); Al wire touches the Ti ball and is melted back (b); two balls on the two sides meet together and became a whole alloyed ball suspended by Ti and Nb wires, and Al kept feeding into the droplet in the middle and melted (c).

4.5.5 Formation of droplets

In SDA elemental wires are fed together into the laser beam where they are melted. The melted alloy droplet formed is suspended on the end of wires and grows larger as more material is melted into it. SDA samples are build up by overlapping of these alloyed droplets. How these wires melt in the alloyed droplet determines the composition and homogeneity of the droplet, and these droplets will determine the final quality of the SDA sample. The characterizations of Ti-Al-Nb samples were shown above, and there were some inhomogeneity issues need to be solved. In order to understand the cause of these inhomogeneities, the formation of the droplets need to be investigated.

The formation of the droplets was studied using high speed video initially processing with only two wires with the systems Ti-Al, Ti-Nb and Nb-Al and then with three wires, Ti-Al-Nb). The feed rates of the wires was kept constant for all the experiments at the optimum rates for Ti-46Al-8Nb, and were Ti 1mm diameter wire 122 mm/min, Al 1mm diameter 102 mm/min and Nb 0.5 mm diameter wire 77 mm/min. The laser power used was 1972 W. The video camera used was a USB microscope camera filming at 30 frames per second.

i. Video of the Ti-Al Droplet

The Ti wire and Al wire were fed into the laser head from one side. A single Ti-Al alloyed droplet was formed in about 17 seconds, Figure 4.28 is a series of screen shots from the video of the formation of Ti-Al droplet that shows the process and the details as the two wires were melted together. The melting point of titanium is 1668 °C, while the melting point of aluminium is 660 °C. Therefore, as the Al wire enters the hot zone at the edge of the column of laser energy it forms a droplet earlier than the Ti wire which generally melts closer to the centre of the laser beam. As they alloy the Ti-Al droplet is attached at the end of the Ti wire. This alloyed droplet has a relatively high temperature since it absorbed most of the energy provided by the laser beam, so when Al wire touches the droplet, the end section of the Al wire is melted into the droplet. As the Al wire is melted back, it takes some time before the Al wire feeds forward to meet with the alloyed droplet again. During the contact between the Al wire and the alloyed droplet during which the Al wire melted back, the droplet was dragged back by the Al wire due to the surface tension (as shown in Figure 4.28-5). Sometimes when the droplet was pulled back the Ti wire did not have enough time and energy to get melted into the droplet, and then it would be exposed outside the droplet. This might lead to the end part falling off directly, see Figure 4.28-7. These Ti particles were quite small, and were only produced occasionally, normally at the beginning stage of the formation of the droplets. As the droplets grew large the Al wire contact does not drag it back anymore, and Ti wire’s end was not exposed outside the droplet so all the materials would melt into the droplet. Generally Ti particles would fall off just 1 – 2 times for every droplet and for some of the droplets; if Ti ends were melted back into the droplet in time then no Ti bits would fall off.

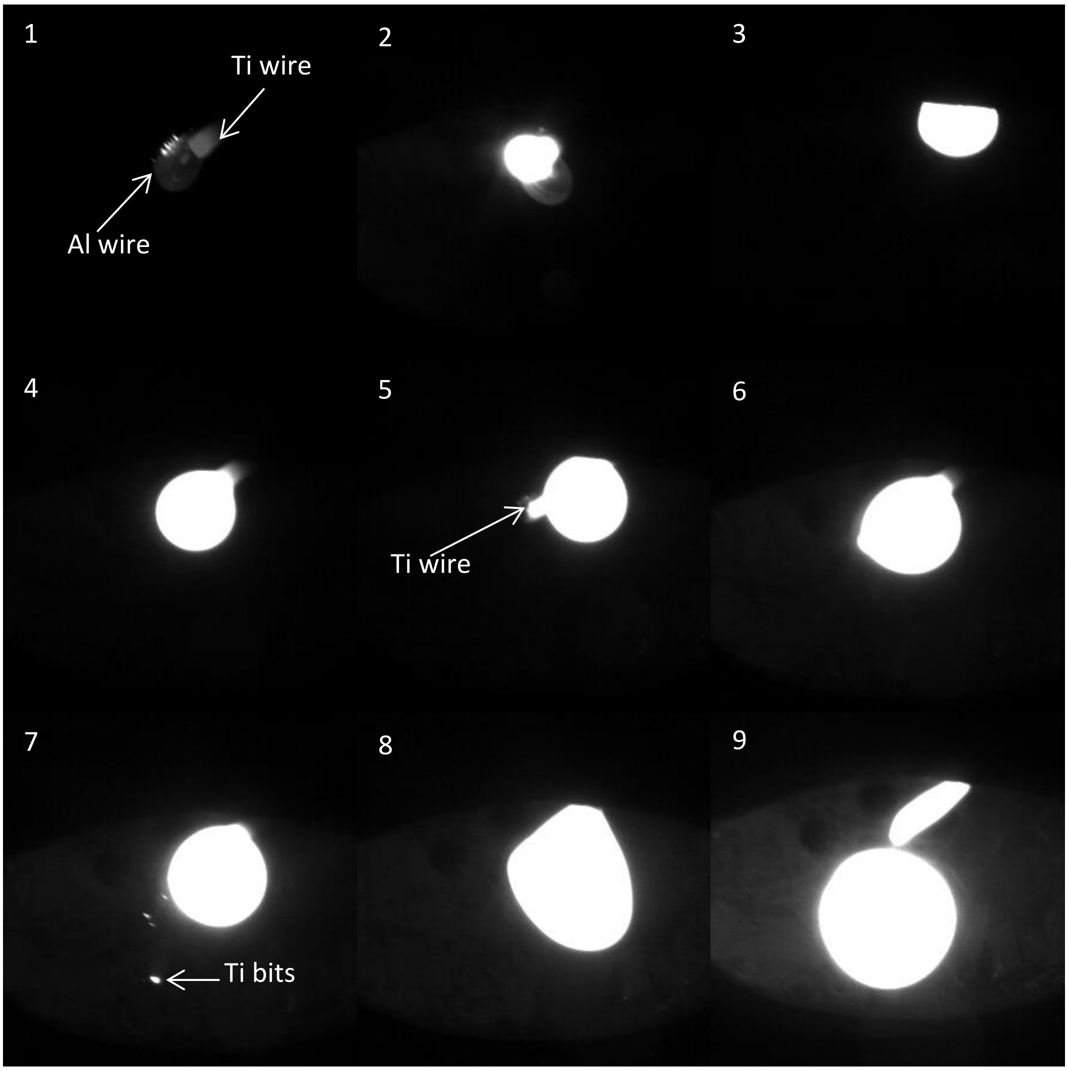

Figure 4.28 Formation of a Ti-Al droplet.

Description of Figure 4.28: (1) 0 s. The start of the process after the last droplet has just detached. The Al wire is already starting to melt due to the low melting point of Al. (2) 0.95 s. Ti and Al wires are fed towards the centre of the laser beam and are melted separately at first. (3) 1.25 s. The Ti ball and Al ball meet and mixed together to become the alloyed droplet. The droplet melts back along the wires immediately when the contact occurs. (4) 2.34 s. As the wires kept feeding, the droplet moves back towards the centre of the laser beam and consequently absorb more energy. (5) 3.22 s. Following another contact from the Al the droplet is melted back again, however the Ti wire in the droplet had not melted yet, so the Ti wire stuck out of the droplet. (6) 5.30 s. The end of the Ti wire, outside the droplet, may melt back into the droplet. (7) 5.45 s. A small part of the Ti wire failed to melt back into the droplet and falls down directly. (8) 13.46 s. As the droplet grew larger, the contact of the Al wire with the droplet was no longer able to drag the droplet of centre but now just causes an oscillation of the droplet. (9) 17.01 s. Finally, the droplet weight is large enough to overcome the surface tension and the droplet detaches from Ti wire.

ii. Video of the Ti-Nb Droplet

At the beginning of the formation of Ti-Nb droplet the Ti wire and Nb wire were always melted separately, with a Ti droplet and Nb droplet attached to their wires respectively. Because of different materials and different wire diameters, Nb wire could only hold a small Nb droplet and it was possible for the Nb droplet to drop off directly. Therefore, before the alloyed droplet was formed there were several Nb droplets which fell down in advance (as shown in Figure 4.29-2, 3). As wires kept feeding, the Ti droplet grew larger and finally it was large enough to touch the Nb wire. A Ti-Nb alloyed droplet was then formed and subsequently the Ti wire and Nb wire were fed into the alloyed droplet directly. Because Nb has a high melting point (2469 °C), sometimes the Nb wire was not melted in the droplet, and would stick out of the droplet. As a result, some of Nb particles would fall off directly as shown in Figure 4.29-4, 5.

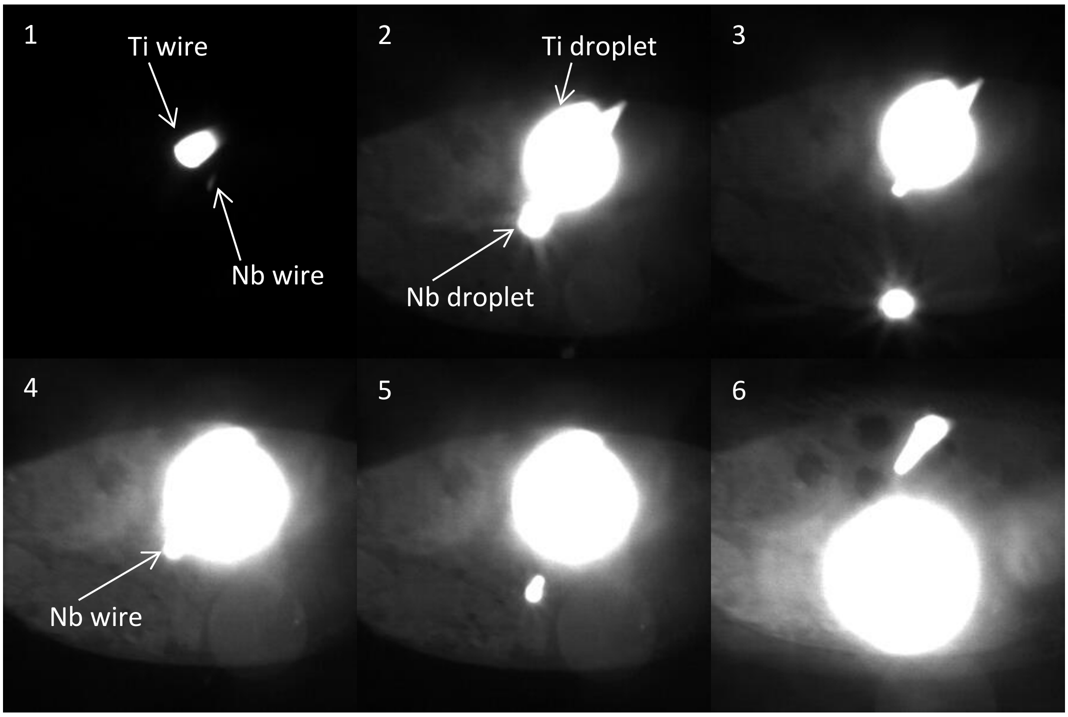

Figure 4.29 Formation of a Ti-Nb droplet.

Description of Figure 4.29: (1) 0 s. The start of the formation with the last droplet was just detached. (2) 7.42 s. Ti wire and Nb wire are melted separately. Each wire has a droplet on it. (3) 7.46 s. Separately a melted Nb droplet is falling off. (4) 16.02 s. Ti droplet and Nb droplet had met with each other and became an alloyed droplet attached to Ti wire. The Nb wire has gone through the alloyed droplet. (5) 16.4 s. The Nb wire's end that was not in the droplet was not melted back into the droplet and fell off directly. (6) 32.06 s. The Ti-Nb alloyed droplet fell from Ti wire.

iii. Video of Al-Nb Droplet

The volume fraction of Al in the Al-Nb droplet was quite high and Nb wire could not hold a large alloyed droplet, so during the formation of the Al-Nb droplet the alloyed droplet was attached on the Al wire. Al-Nb droplet formation time was about 6 s, much quicker than other Ti-Nb, Ti-Al, or Ti-Al-Nb droplets. When the Nb wire touched the

Al droplet it made the Al ball melt back (see in Figure 4.30-2). Before the alloyed droplet moved back to the centre (like Figure 4.30-4 shows), the Nb wire was melted alone and deposited small pure Nb particles (as shown in Figure 4.30-3). In Figure 4.30-5, we can see the alloyed droplet was attached on Al wire. However, the droplet's temperature was quite high and it made the Al wire's end that held the droplet melt back The Al-Nb droplet fell off after 5.8 s. It may not be homogeneous since its surface showed parts with different contrast.

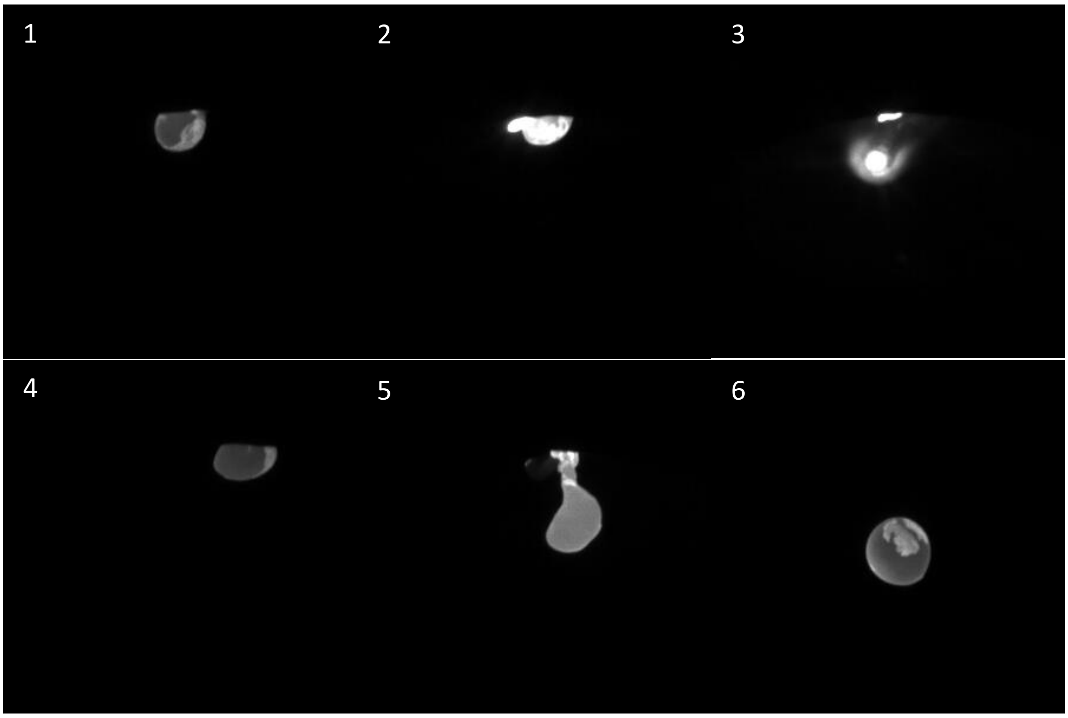

Figure 4.30 Formation of an Al-Nb droplet

Description of Figure 4.30: (1) 1.18 s. 0 s was set when the last Al-Nb droplet was fell off. From 0 – 1.18 s, the Al ball appeared gradually as its temperature increased while it got closer to the laser beam. The Nb wire is hidden behind the Al ball and could not be observed. (2) 1.30 s. The Nb wire touches the Al ball, and the droplet's temperature is increased and melts back along the Al wire. (3) 1.34 s. After the droplet melts back and is hidden behind the nozzle, the Nb wire is melted drops off alone. (4) 1.50 s. The alloyed droplet moves towards the centre again. (5) 4.04 s. The alloyed droplet was attached on the Al wire, and Al wire’s end part was half-melted. (6) 5.80 s. The Al-Nb droplet was falling off. The droplet may not be homogeneous as the surface of the droplet shows some contrast.

iv. Video of the Ti-Al-Nb Droplet

Ti, Al and Nb wires each melt separately at first. Because there are three wires melting, and Ti and Al wires’ feed rate were relatively fast, their Ti and Al droplets were growing relatively fast and consequently the Ti, Al and Nb drolets all meet together before the Nb droplet can fall off alone. The alloyed droplet was attached by both Ti and Nb wires on two side of the droplet, and Al wire was fed in the middle. The droplet was always hanging in the middle by Ti and Nb wires to keep the balance (as shown in Figure 4.27-c). However during the growth of the alloyed droplet, the speed of the Ti and Nb wire were too fast to allow the wires to melt completely in the droplet, so sometimes the wires would stick out from the droplet. The exposed wire’s end part would fall off directly as Ti and Nb particles (see in Figure 4.31-4 – 4.31-8). The Ti particles were smaller than Nb particles, and after these particles deposited in the melting pool, the melting pool had enough energy to melt/dissolve the Ti particles. Therefore, Ti particles that deposited alone did not affect the quality the SDA sample significantly and were not a problem. On the other hand, the Nb particles did not melt/dissolve in the melting pool after deposition. As a result, Nb particles would remain in the SDA sample and made the sample inhomogeneous.

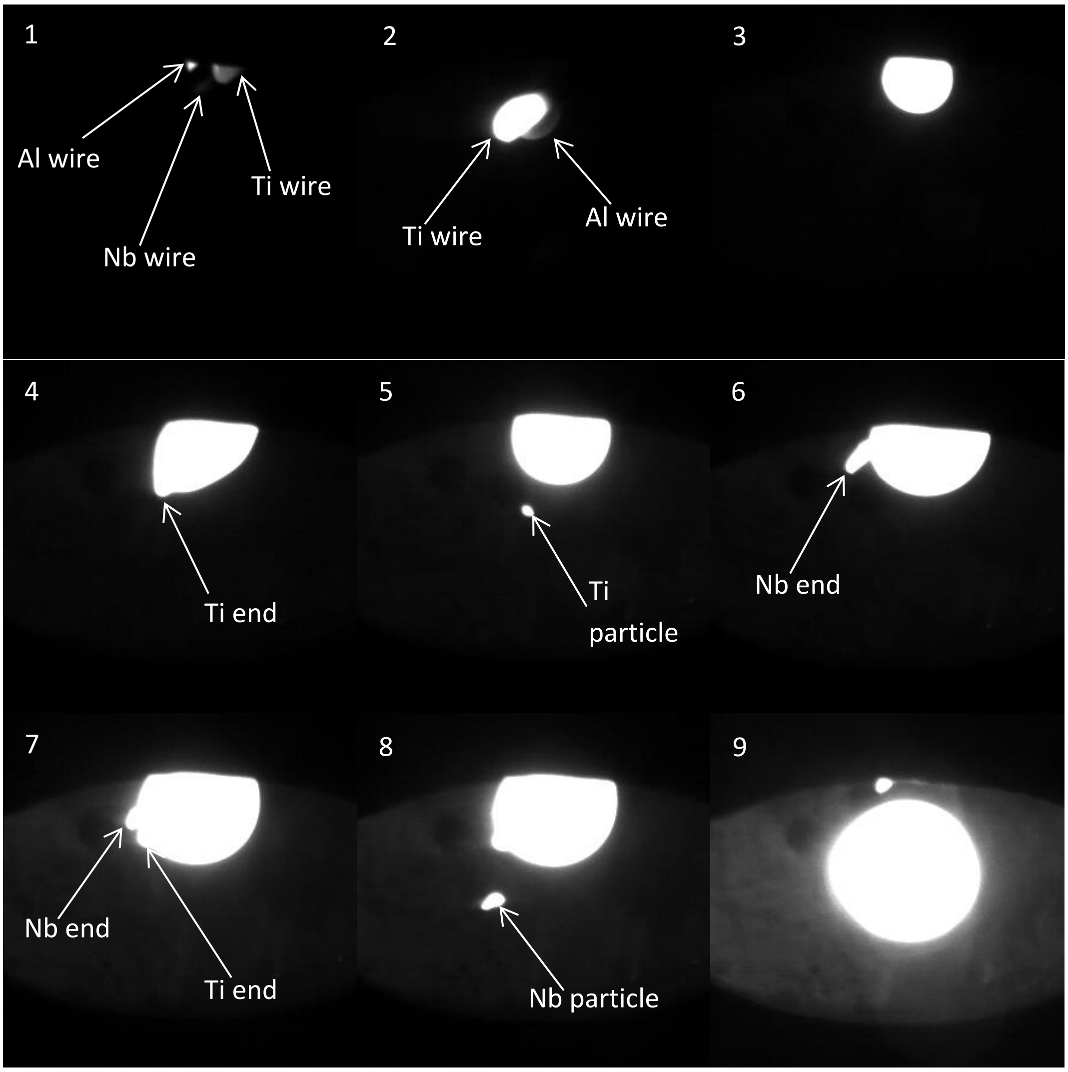

Figure 4.31 Formation of a Ti-Al-Nb droplet

Description of Figure 4.31: (1) 0 s. The previous Ti-Al-Nb droplet has just dropped off. (2) 1.30 s. Ti, Al and Nb wires are melting separately. (3) 1.56 s. Ti, Al and Nb droplets have met together and mixed to become an alloyed droplet. (4) 5.31 s. Ti wire is protruding outside the droplet. (5) 6.25 s. The end of the Ti wire did not melt back into the droplet and fell off directly. (6) 12.92 s. Nb wire sticking out from the droplet. (7) 13.41 s. Nb and Ti wires exposed outside the droplet. (8) 13.46 s. The Nb wire end fell off directly and the Ti wire end was melted back into the droplet. (9) 20.54 s. The alloyed Ti-Al-Nb droplet was too big to suspend on the wires and fell off.

By observing the formation of Ti-Al-Nb droplet it is clear that even processing with optimized process parameters some Nb particles will be incorporated in the final samples. The optimized parameters can reduce the number of Nb particles in one SDA sample, but some will always be incorporated into the larger samples.

4.5.6 Compositions of individual droplets

In order to use SDA samples for some screening trials such as mechanical testing, the homogeneity of the SDA sample as a whole part required. The SDA samples are built up by the deposition of a series of droplets. These droplets should have the same chemical compositions due to the constant feed rate of their constituent wires, and consequently the SDA sample, which is the combination of the alloyed droplets, should be homogeneous.

A series of 13 alloyed Ti-46Al-8Nb droplets were checked in a row to see the consistency of their contents in order to verify this assumption. The 13 alloyed droplets were deposited one by one, and their depositions were determined separately by EDX analysis of a polished section. The EDX results are listed in Table 4.6. The formation of each of these alloyed droplets was also recorded by the high speed camera to observe any problems during manufacture.

Table 4.6 Chemical compositions of serial Ti-46Al-8Nb alloyed droplets

Serial Number	Al (at.%)	Ti (at.%)	Nb (at.%)
1	44.8	46.2	9.0
2	42.4	48.5	9.1
3	47.9	43.6	8.5
4	44.1	47.7	8.2
5	46.5	43.5	10.0
6	48.8	41.8	9.4
7	44.4	46.8	8.8
8	44.6	46.6	8.8
9	43.3	48.0	8.7
10	45.3	45.8	8.9
11	44.9	46.0	9.1
12	43.2	47.8	9.0
13	44.8	46.2	9.0

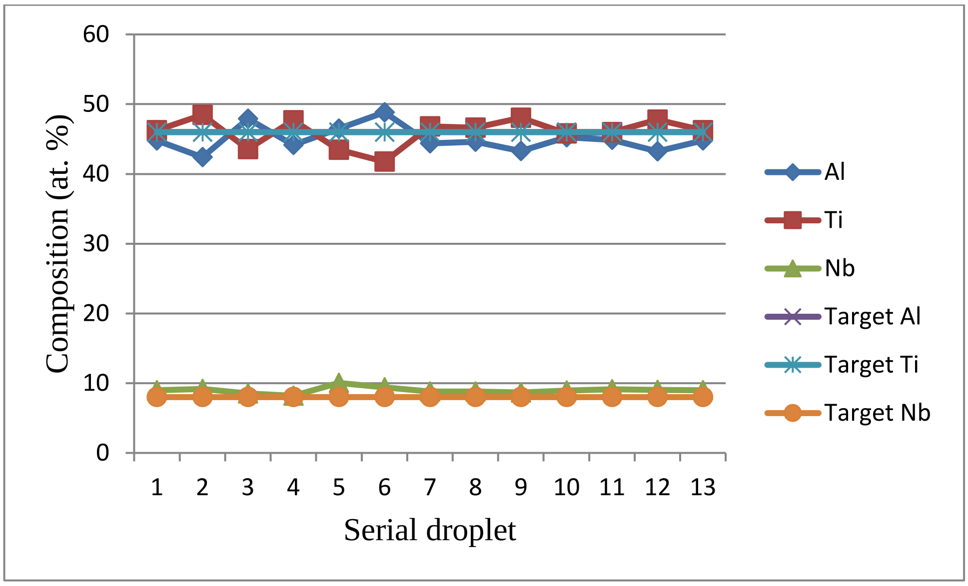

Figure 4.32 Actual compositions of 13 alloyed droplets of nominally Ti-46Al-8Nb

From Figure 4.32, it is clear that within these 13 alloyed droplets, Nb was the most consistently introduced element compared to Ti and Al .The Nb content was with 1 at.% of the target level for all the droplets. Among these 13 droplets, Droplets 2, 6, 9 and 12 had a larger chemical variation to the target composition compared to the other droplets.

4.5.7 Ti-46Al-8Nb samples with different process parameters

During the SDA process, there are mainly two parameters to be controlled: laser power and wire feed rate. To investigate the effect of these parameters four TiAlNb samples were made with same wire feed rates and different laser powers and another four TiAlNb samples were made with same laser power and different wire feed rates. All these 8 samples have the same chemical composition of 48.7% Ti, 43.7% Al and 7.6% Nb (all in atomic fraction). The details of these samples are listed in Table 4.7.

Table 4.7 TiAlNb samples made with different process parameters

Sample	Laser power (W)	Ti feed rate (mm/min)	Al feed rate (mm/min)	Nb feed rate (mm/min)	Feed volume (mm^3/min)
1	1498	241	202	153	378
2	1677	241	202	153	378
3	1879	241	202	153	378
4	1972	241	202	153	378
5	1972	482	404	306	766
6	1972	122	102	77	191
7	1972	80	67	51	125
8	1972	61	51	38	95

The samples were polished and etched to reveal the microstructure. Optical images can show the Nb rich particles clearly which is the main defect of these low Nb TiAlNb samples. From the optical images of 4 samples made with same wire feed rates and different laser powers, the number of Nb rich particles was found to be reduced with the laser power raised up.(as shown in Figure 4.33).

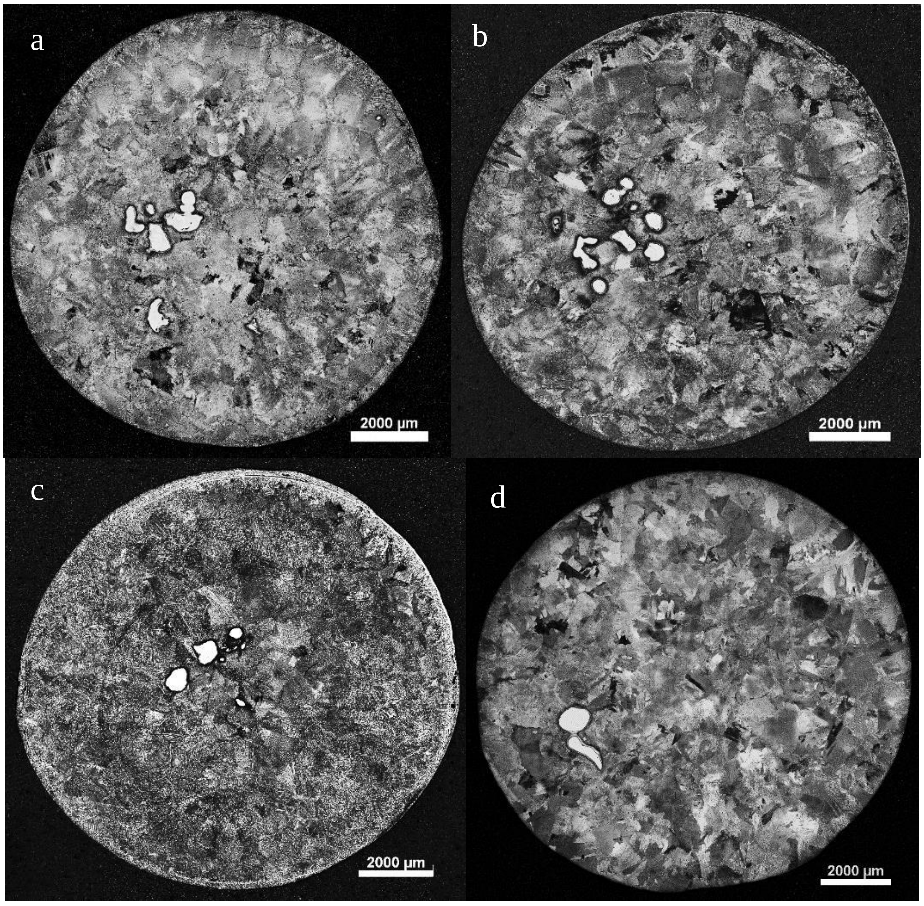

Figure 4.33 Optical images of 4 TiAlNb samples made with different laser power. The laser powers used in 4 samples from a to d are 1498 W, 1677 W, 1879 W and 1972 W respectively.

For the 5 samples made with same laser power and different wire feed rates, the optical images are shown in Figure 4.34. From a to c, the number of Nb rich particles decreases as the feed rate slow down. Samples c and d have no inclusions appeared under OM.

However, according to the EDX results, d has a composition of 48.43% Ti, 36.47% Al, 6.02% Nb and 9.09% Fe (all in atomic fraction). This Fe contamination was from the substrate of the sample which is steel. Samples d and e are both contaminated by the substrate melting into the sample. These two samples were also not able to build upward during the process. The sample (c) with a feed rate of 122 mm/min Ti, 102 mm/min Al and 77 mm/min Nb is the homogeneous.

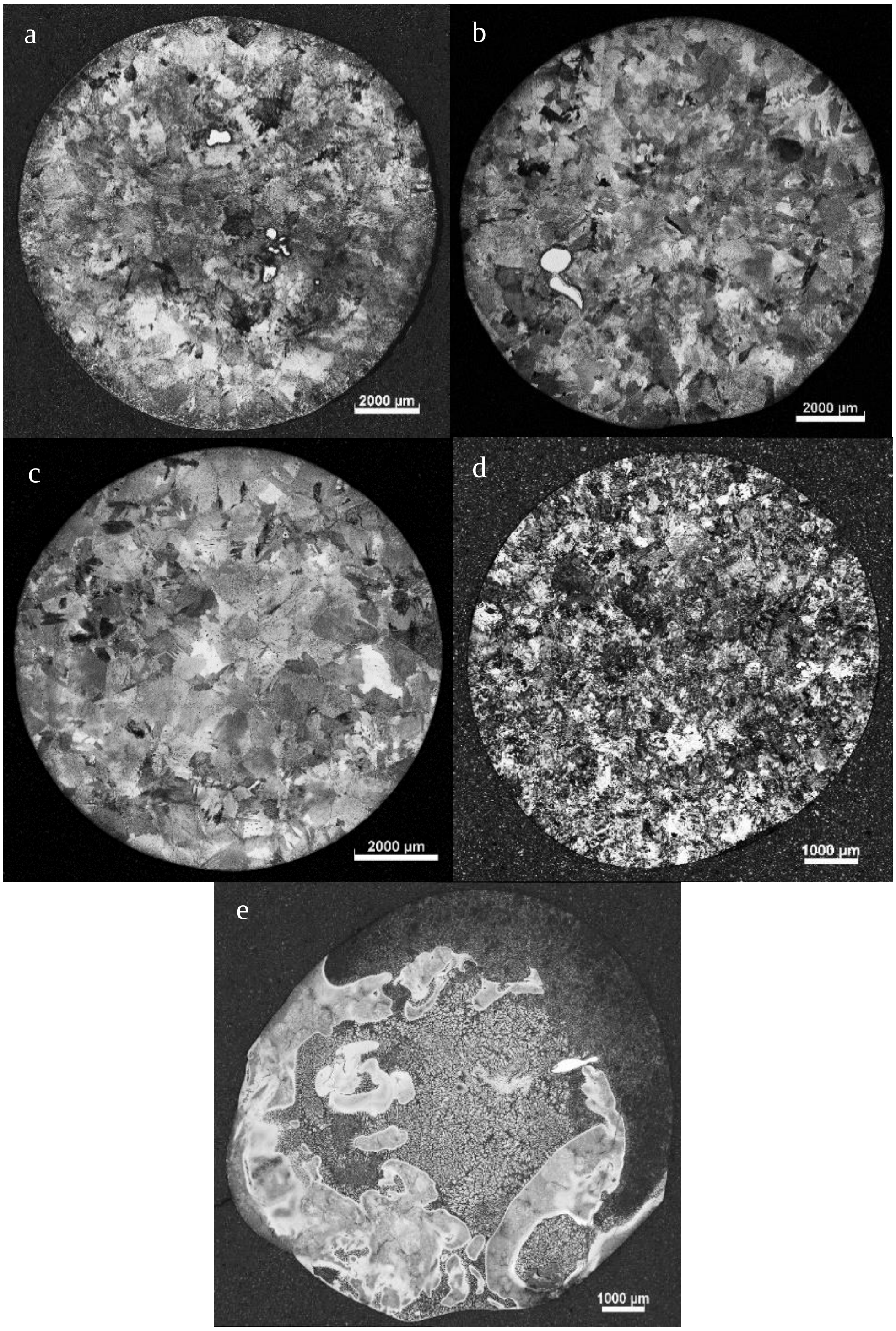

Figure 4.34 Optical images of 5 TiAlNb samples made with different feed rate. The feed volume used in 5 samples from a to e are 766 mm^3/min, 378 mm^3/min, 191 mm^3/min, 125 mm^3/min and 95 mm^3/min respectively.

A compositional contour map has been made to validate its homogeneity. Al and Nb distributions in the TiAlNb sample are shown in Figure 4.35. Al and Nb contents have a variation within 4 at.% across the whole sample, and the standard deviations of Al and Nb are 0.4 and 0.2 relatively.

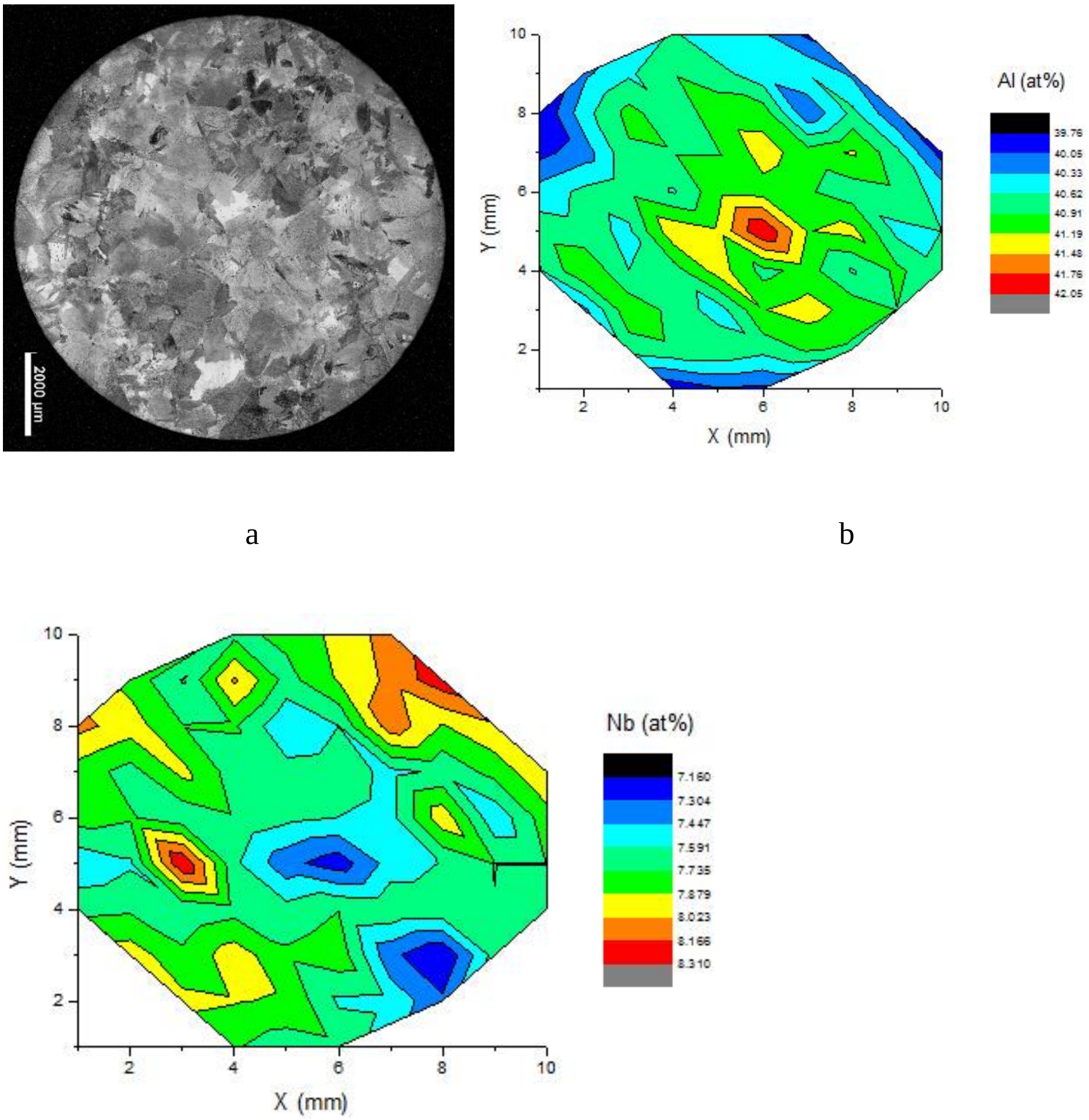

a

b

c

Figure 4.35 (a) Optical image of the homogeneous TiAlNb sample; (b) Al distribution in the sample; (c) Nb distribution in the sample.

4.5.8 Discussions

i. The cause of inhomogeneity of Ti-Al-Nb samples

In the first trial of Ti-Al-Nb samples, 50 samples were successfully made and 30 of them were homogeneous. The other 20 samples were failed for different reasons, and they are mainly summarized into four kinds of inhomogeneity as mentioned in 4.5.1.

Some samples were rejected because the chemical composition was found to vary significantly from sample's edge to the centre. To find out the cause of this kind of inhomogeneity, we can start with the analysis of the consistency of sequential deposited droplets.

Among 13 sequential deposited Ti-46Al-8Nb samples, 4 droplets present a relative larger chemical variation as shown in Figure 4.32. Take Droplet 6 for example, the Ti content of Droplet 6 was 4.3 at. % lower compared to the target composition. According to the video recorded by the high speed camera, at the beginning of formation of Droplet 6, a single Ti ball was fell off alone before the three wires met together and formed the alloyed droplet (as shown in Figure 4.36). Therefore the final alloyed droplet had a lower content of Ti.

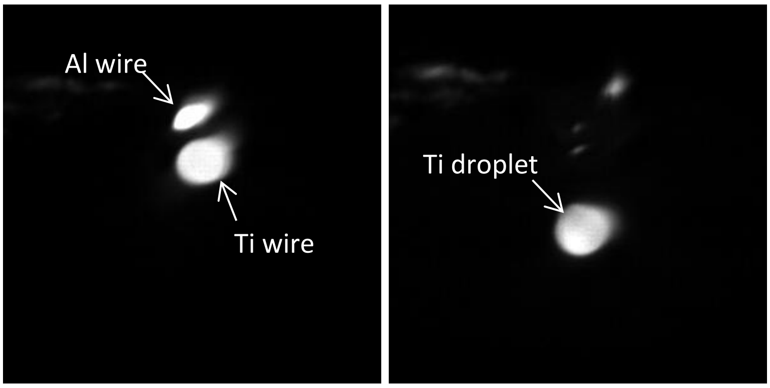

Figure 4.36 The beginning of the formation of Ti-46Al-8Nb Droplet 6

Generally speaking, the slight variation of the composition of the droplets does not have much influence on the homogeneity of the final large SDA samples. This is because the SDA samples are built up by the overlapping of the alloyed droplets, see Figure 4.37 shows. During the production of the SDA samples, a melt pool is always observed on the top of the sample where the alloyed droplets are deposited. There is considerable mixing of material in this area and the content of several droplets are blended together. For each layer of the SDA sample, it is actually the mixture of 3-4 droplets. Therefore, as long as the chemical differences are not too much, these slight variations between alloyed droplets can be reduced by the further mixing in the melting pool after deposition.

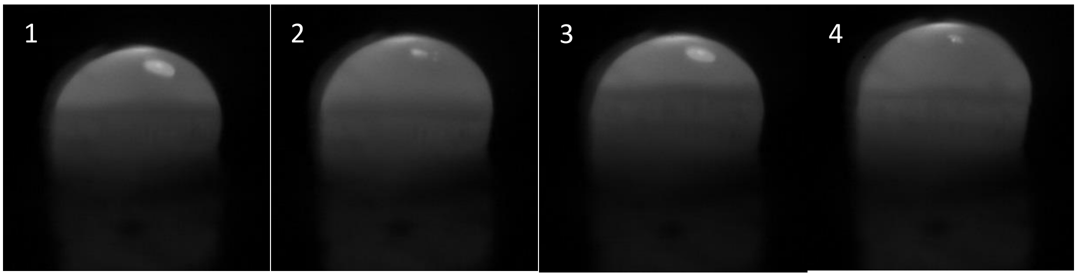

Figure 4.37 Two Ti-46Al-8Nb droplets deposited into the melting pool

Description of Figure 4.37: (1) Just before the first droplet fell into the melting pool; (2) the first droplet just fell into the melting pool. The boundary of the solidified bottom part and the melting pool was remelted because the deposited droplet with high temperature. (3) Just before the second droplet fell into the melting pool. During the formation of the second droplet above the melting pool, the melting pool had shrunk as the bottom part of the melting pool was solidified gradually. (4) The second droplet just fell into the melting pool and the melting pool was getting larger again by re-melting the solidified layer beneath the melting pool.

However, if the chemical difference between each deposited droplet was too big, the chemical variation still can’t be eliminated completely by the diffusion of these droplets in the melting pool during the limited solidification time. The inhomogeneities like rings with slight compositional differences and regions with different Al content are all caused by the chemical variation between the deposited droplets.

Rings with slight compositional differences show in the SDA samples can be called the “ring effect” as several rings can be clearly seen, for example as it shown in Nb-50Al (Figure 4.13). In the back-scattered image of the Nb-50Al sample there are several rings. One of the rings with less precipitates has a higher Nb content. Combine with the compositional contour of Nb-50Al (Figure 4.20a), the centre and the edge have a similar composition, but between centre and edge the Al content is lower than other areas. This result can generally be treated as the outcome of several droplets’ overlapping. Every droplet is expected to have 50 at.% Al and 50 at.% Nb, however some droplets may have less Al mixed in it. After Nb rich droplet spread in the melting pool and covered by the next droplet, the Nb rich ring was formed and solidified under a limited diffusion time. As Figure4.38 shows, the bulk specimen is the result of overlay of droplets.

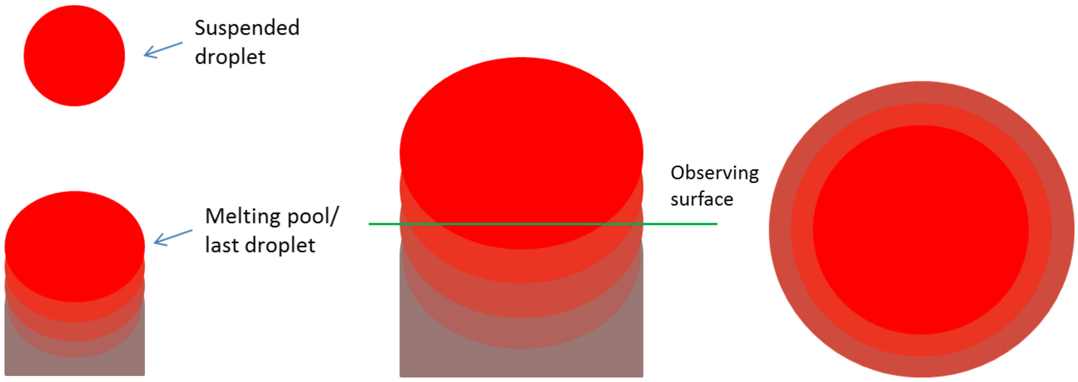

Figure 4.38 A schematic of a sample build by several droplets and its observing part

After the sample, is produced the characterization is undertaken on a polished section, a horizontal plane of the sample. Therefore, the material in the edge area and centre area is coming from different droplets. The difference in the droplets may lead to a variation in the sample from its edge to the centre. Moreover, the precipitates near the edge are finer than the precipitates in the middle of the sample. This is due to the edge area has a faster cooling rate than the centre.

Regions with different Al content is also caused by droplets with different compositions, however the droplets were not deposited right in the same position. Therefore, instead of the ring effect, the samples presented regions with chemical variation.

These inhomogeneities mentioned above were all due to the droplets with different compositions which are decided by the wires mixing above the melting pool. However, the wires mixing behaviour can’t be controlled completely, it can only be improved by applying proper wire feed rate to avoid the unwanted deposit situations as much as possible. Moreover, the substrate can be preheated or other heat sources can be placed around the melting pool to slow down the solidification and extend the diffusion time for the deposited droplets in the melting pool.

Despite the inhomogeneities been discussed above, a certain number of samples were found to contain Nb rich particles and regarded as inhomogeneous. During the SDA process, the three constituent wires were melted above the melt pool to form a prealloyed droplet which then drops into the melt pool. The laser beam is focused on the droplet which shadows the melt pool. The prealloyed droplet is the main place for three metals to diffuse/react with each other. Nb wire needs sufficient energy and time to melt in the suspended droplet, otherwise the Nb cannot get melted completely and Nb wire will stick out of the alloyed droplet like Figure 4.39 shows. Then these Nb needles will fall into the melting pool directly. The melting pool does not have enough energy to melt these needles, thus Nb rich particles are remained in the final sample.

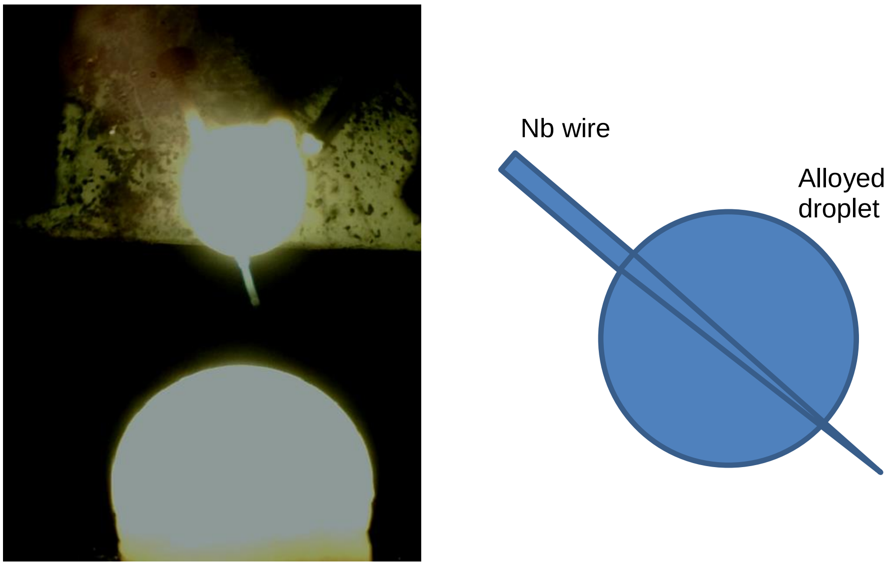

Figure 4.39 Nb wire's melting condition when the feed rate is high

It is not only when the Nb wire feed rate is too high that the wire protrudes out of the droplet but a movement of the alloyed droplet would also expose the Nb wire. The Ti-Al-Nb alloyed droplet sometimes would be dragged backwards by the Al wire. As Figure 4.31 shows, Ti and Nb wires hold the alloyed droplet in the middle during the process, Al wire would feed towards the centre and touch the alloyed droplet. Once the droplet was touched by Al wire, it would move back a little bit because of the surface tension and expose the Nb wire. The exposed Nb end would drop into the melting pool directly instead of melting back to the alloyed droplet. Therefore high laser power and low feed speed are needed to provide enough energy to melt these Nb particles. The process parameters like laser power and feed rate will be discussed later in "The optimization of SDA for Ti-Al-Nb".

ii. Al loss during the SDA process

From the EDX result of Ti-Al-Nb samples in Figure 4.11, Ti-Al-Nb samples have lower Al content generally than the target composition. That is because laser power has to be high enough to melt all three wires, while the boiling point of Al is close to the melting point of Nb so there is some vaporization of the Al during alloying. This vaporization could be observed during the SDA process. For example, the white smokes which can be seen in Figure 4.22-24 is vaporized Al. By measuring by EDX the actual Al content compared to the target Al content the compensation ratio of Al has been worked out according to the equation:

$$\text{Compensation ratio of Al} = \frac{\text{Target composition of Al} - \text{Measured composition of Al}}{\text{Target composition of Al}}$$

However the compensation ratio is not a constant across all the samples. This is in part because the measured composition of Al cannot reflect the actual Al content in the sample. For example, if there is one sample's Al content are measured 5 at.% less than its target composition, then there may be 1-2 at.% EDX system error in this 5 at.% loss. Since the system error is random and unpredictable, the compensation of Al cannot be quantified. Also the Al loss during the process varies with different laser power. Therefore, to accurate compensation of the Al loss is not possible. Generally speaking, for elements Ti and Nb, 1-2 at.% difference value compared to the target composition is acceptable. As for Al, a difference value less than 3 at.% is also reasonable. In the combinatorial approach the actual sample is characterised and this property value can be plotted against the measure composition.

iii. The optimization of SDA for Ti-Al-Nb

Only 30 out of 72 samples are successfully produced and checked to be homogeneous using SDA in Ti-Al-Nb alloy system when it was initially investigated (as Figure 4.23 shows). The other samples were failed due to the brittleness of the sample or due to the sample's inhomogeneity. Even for samples with same composition some may be produced successfully and while another may have inclusions in it. This indicates that the reliability of the SDA system is not ideal. Therefore, further exploration of the process was undertaken in order to enhance the repeatability of the SDA system and increase the possibility of making homogeneous samples.

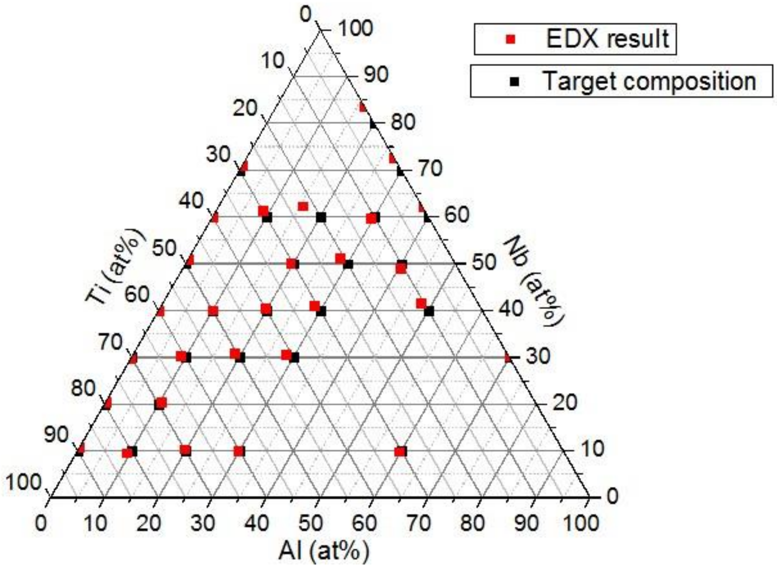

Figure 4.40 30 homogeneous Ti-Al-Nb samples with different composition formulations and its relative EDX result in the ternary diagram

a) Wire selections

From initial trails it was determined that the feed angles for the feedstock wires are important. The wires need to meet together under the laser beam to melt. A small misalignment of wires can mean the wires miss the beam and consequently the wires do not melt. Wires are fed from spools to the nozzle head through plastic tubes, so the 0.5 mm wires have certain tendency to curve when they exit the nozzle head. The feed angles of all wires were therefore adjusted by twisting the plastic tubes to find a position where all the wires go through the laser path. However this was difficult to control. Needle tubes were added to the head to help the wires feed straight. However, for some elements with low melting point or wires with low feed rate, the wires can be easily melted back into the needle tube and stop the wires from feeding. It was found that increasing the wire diameter to 1.0mm (from 0.5mm diameter) improved the reliability of the melting process. The 1 mm diameter wire was found to come off the spool with less of a curve which allowed them to feed more directly into the laser without rotating the plastic tube. For a given composition, replacing 0.5 mm wire into 1 mm wire slows the wire's feed rate by a factor of 4. Sometimes this substitution can make the various feed rates of the feedstock similar which can help wires melted together smoothly. So according to the composition the choice of wire with different diameter can make the processing more reliable.

In Figure 4.41, the Ti-Al-Nb ternary diagram has been divided into three regions based on the homogeneous Ti-Al-Nb samples' distribution on the ternary diagram (as shown in Figure 4.40). Most of homogeneous samples were in region B. The Ti-Al-Nb ternary phase diagram (as Fig 4. 42 shows) indicates there is not much TiAl γ phase in this area. Also in region B, samples have a relative high Ti, medium Nb content and low Al content. Because of the density difference this combination of the elements has fairly similar wire feed rates. For the failed samples in region A and C trials were undertaken to investigate if using different wire diameter might ease their manufacture. Trials were made with Ti & Al wires between 0.5 mm and 1 mm.

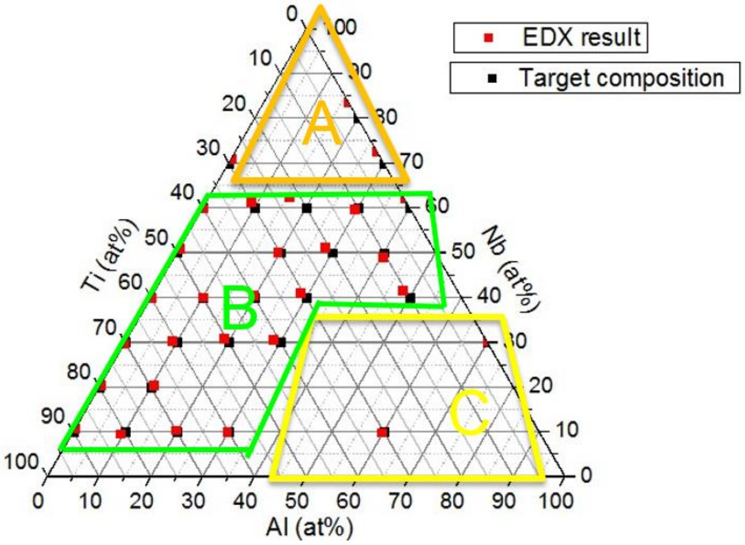

Figure 4.41 wire selections according to the 3 regions in Ti-Al-Nb ternary diagram

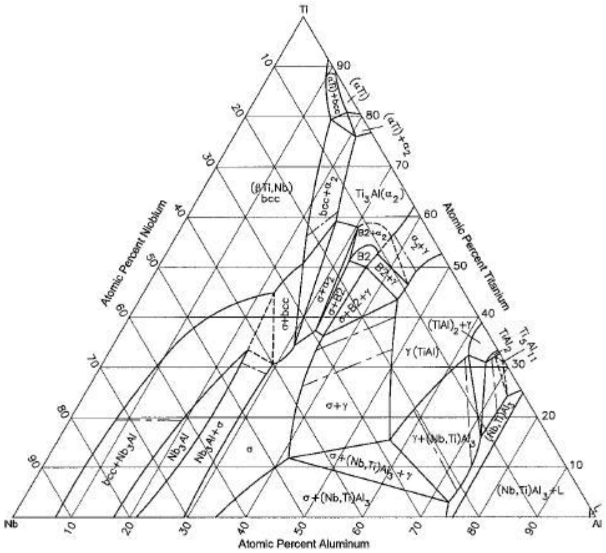

Figure 4.42 Ti-Al-Nb ternary phase diagram isothermal section at 1000°C

(Witusiewicz, V. T., et al. 2009)

Region A is the samples with high Nb content with the Nb wire's feed rate much higher than Ti & Al wires. It has been found that the Nb wire needs to be controlled to under 500 mm/min to assure it is melted properly, which means a low feed rate of the Ti and Al wires. To make 10Ti-10Al-80Nb in region A for example the possible wires choices and relative wires feed rate are listed in Table 4.4. The selection of 1 mm Al and Ti wires and 0.5 mm Nb wire leads to the separate melting of three wires. The selection of 1 mm Ti wire and 0.5 mm Al and Nb wires can't make Ti alloyed into droplet properly. The selection of 0.5 mm Ti, Al and Nb wires makes Ti melt alone. As a result, all the three wire choices seems not work properly, and the further suggestion is to try 1 mm Nb wire to slow down the Nb feed rate. It will give more time for Ti and Al to feed into the alloyed droplet instead of deposit alone.

For region C in Figure 4.41, although TiAl intermetallic phase and Nb particles may cause the failure of the products, with a suitable wire selection a good feed pattern can be achieved so that the homogeneous samples can be made. Ti-46Al-8Nb in region C is an example. Region C as a low Nb content region, if three wires were all 0.5 mm, Ti and Al wires feed rate are too high compared to the Nb wire feed rate (see in Table 4.5) which leads to the separate melting of Nb and can't form the alloyed droplet in time. Change of Ti wire from 0.5 mm to 1 mm does not help much, and the alloyed droplet was attached by the Ti wire and the Nb wire still can't get involved in the alloyed droplet properly. The selection of 1 mm Ti and Al wires and 0.5 mm Nb wire can make the alloyed droplet hold in the middle by both Ti and Nb wire. This feed pattern can help all three wires feed into the alloyed droplet.

b) Wire position

The position relationship between three wires has an important influence on whether three wires can meet each other successfully and form the alloyed suspended droplets. Because Al wire melts back easily, it has been found that it is best if it is placed in the middle of the three wires. Otherwise, Al will always melt back on the side before it reaches the ball attached on Ti or Nb wire which lead to the situation that Al melts alone on one side and Ti and Nb melt together on the other side. Moreover, this Ti-Al-Nb wires feed position (Ti and Nb wires on two sides and Al wire in the middle) was more stable than other wires feed positions. Because the droplet was no longer dragged back too much by the Al wire while the Al wire kept touching the droplet and melting back and feeding forward again.

c) Process parameters

Even with the optimum wire selection, Nb rich particles can still sometime be observed in the samples. Therefore, the influence of the process parameters on samples was investigated to improve the performance of the SDA process.

Ti-46Al-8Nb samples were made by SDA using different laser power and wire feed rate. As the laser power increased, the Nb particles in the samples reduced. The higher laser power, the more energy will help to melt the Nb particles. On the other side, as the wire feed rate gets lower, the Nb particles were also reduced even with no Nb particles in it anymore as shown in Figure 4.34-c. However, with further reduced wire feed rate, the samples started to be contaminated by the stainless steel substrate. The wire feed rate was too low, in other words, the laser power for the current wire feed rate was too high, and too much energy than expected was absorbed by the melting pool.

Therefore, if the laser power is too high or feed rate is too low, three wires tend to melt back which can lead to overheating of the melt pool. The overheating of the melt pool may lead to contamination by alloying with the substrate as well, and may even cause collapse of the sample which means the sample cannot be build up successfully. If the laser power is too low or feed rate is too fast, the suspended droplet does not have enough energy to melt the Nb completely. Then the Nb wire protrudes out of the droplet as shown in Figure 4.39. The Nb needle part that sticks out of the droplet will then get melted by the laser beam and drop into the melting pool. Since the melting pool still does not have enough energy to melt these needles, they will remain in the sample as Nb rich inclusions.

In summary, with a proper selection of the wires, the right feed position and optimised process parameters, a wide range of sample compositions can be produced successfully by SDA. A Ti-46Al-8Nb sample with a feed rate of 122 mm/min Ti, 102 mm/min Al and 77 mm/min Nb could repeatedly be produced with a homogeneous structure as a result of the exploration of SDA process optimization.

4.6 SDA splats

4.6.1 Ti-46Al-8Nb splats

To build up a homogeneous full size SDA sample, a series of alloyed droplets with similar compositions are required and these droplets need to deposit into the melting pool. However, the study of the Ti-46Al-8Nb droplets shows that the formation of the droplets is not a completely consistent process. Both the composition and the deposit position of the droplet are unpredictable. Therefore it is more difficult to build up a SDA sample rather than just deposit a single alloyed droplet. Moreover, contamination by small elemental particles is less likely when single alloy droplets are considered.

For several investigations undertaken by partners in the AccMet project, such as characterization of superconductivity and thermoelectric effect, small but flat samples are required. An investigation was therefore made into the production of an alloyed splat by depositing a single alloyed droplet.

A splat is made by depositing an alloyed droplet. The alloyed droplet is formed in the usual way by melting different wires together in the laser beam. Once the alloyed droplet is large enough it drops off and is deposited on a copper substrate where it is solidified quickly to become a splat. Because the falling time of the droplet is short and the solidification of the splat is fast, the homogeneity of the splat requires mixing of the materials while the droplet is still hanging on the wires. A first investigation was therefore made to determine whether Ti-46Al-8Nb droplet is mixed uniformly before it was impacted on to the substrate.

A Ti-46Al-8Nb alloyed droplet was deposited from a low height on the substrate and became a half-arc disc with a diameter of 16 mm. The undersurface of the splat was checked using SEM. There were cracks cross the splat due to the fast cooling rate, and a small Nb particle with a diameter of 160 µm near the edge (as shown in Figure 4.43). The microstructure of the splat was not like standard tall SDA samples with lamellar because the splat has experienced a fast cooling rate. Figure 4.44 shows the rapidly solidified splat had a fine microstructure. According to the EDX results, the Ti-46Al-8Nb splat had an average composition of 46.76 at.% Ti, 45.96 at.% Al and 8.28 at.% Nb with a small variation of less than 2 at.%. The Ti-46Al-8Nb splat showed a homogeneous composition and a uniform microstructure. This suggests that SDA splats should be suitable samples for some characterization tests. These samples can be produced even more time efficiently and with a considerable material saving compared to producing the regular SDA tall samples.

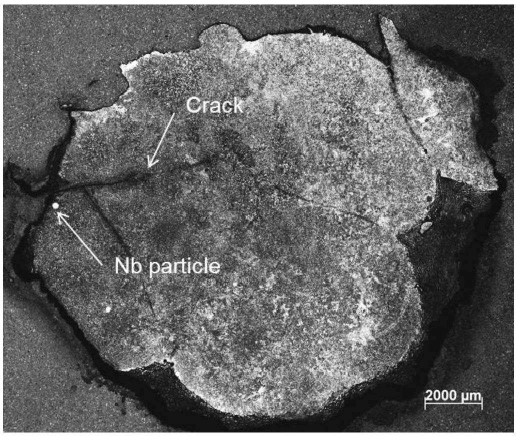

Figure 4.43 The optical image of undersurface of the Ti-46Al-8Nb splat

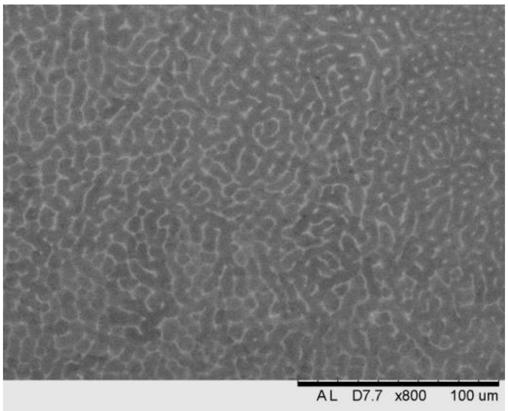

Figure 4.44 The back scattered image of undersurface of the Ti-46Al-8Nb splat

4.6.2 Simulation of the splatting process

For some characterization methods a flat sample is preferred. In order to study the parameters that affect the geometry of the splats, the simulation software SimDrop was introduced into the project. SimDrop is a droplet impact and solidification simulation software provided by Simulent (Simulent Inc.: siminfo@simulent.com). By inputting required data such as: initial drop temperature; initial radius of the drop; initial drop velocities; height; gap time between drops; initial substrate temperature; thermal resistance between solid and substrate; drop material file (liquid density, kinematic viscosity, thermal conductivity, surface tension…); and substrate file (density, thermal conductivity…), the software would give series of files that shows the shape change and temperature change of the droplet during splatting (like Figure 4.45 shows). Because Simdrop is a commercial and relatively simple simulation software, the simulations were started with pure Ti droplets and according to the purpose of simulation, only f-files that indicate the shape change of the droplet have been studied to see how different parameters may change the shape of the droplet.

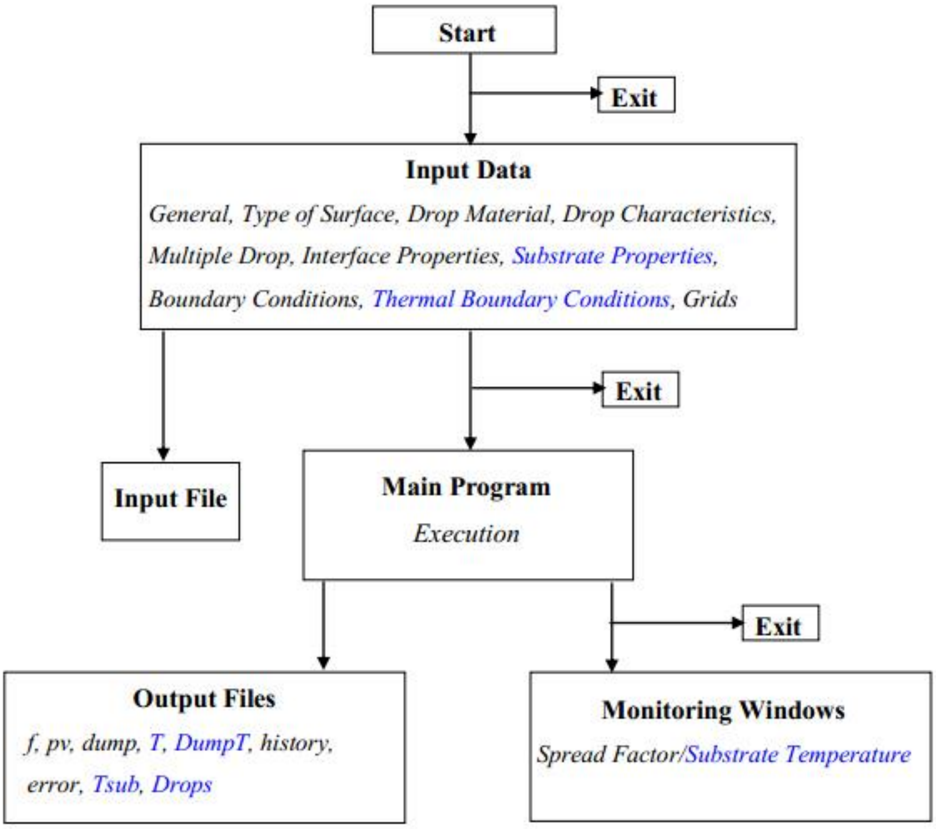

Figure 4.45 The flowchart of the SimDrop simulation process

i. Measurement of the droplet temperature

To improve the accuracy of the simulation it needs to be based on the actual SDA deposition process. This requires the temperature of the Ti droplet as it begins to fall. The temperature has been measured using a Metis MQ22 pyrometer. Table 4.8 shows the Ti droplet's measured overheated temperature, measured melting temperature and the calculated actual temperature. The Ti droplet was melting by 1970W laser beam with one Ti wire feeding.

Table 4.8 The measured overheated temperature, measured melting temperature and the calculated actual temperature of the Ti droplet that was melted by 1970 W laser beam with one wire feeding

Measured Overheated T (°C)	1008	1034.4	1030.2	1004.4
Measured Melting point (°C)	858.9	916.3	920.8	941.8
Actual T (°C)	2137.8	1995.6	1967.7	1829.77

Because the temperatures were measured by the infrared ray that pointed to the Ti droplet, any misalignment would lead to a lower measuring result than the actual temperature. Therefore, among this series of calculated actual temperatures of the Ti droplet, it is more accurate to use the highest value among them rather than the average value of them. As a result, the Ti droplet's temperature was estimated as 2138 °C. Although a significant superheat (470 °C) over the melting point of Ti this temperature is far below the melting point of Nb and would act as a quench.

ii. Simulation of the impact Ti droplets with a substrate

Generally speaking the simulation suggests that with a higher initial droplet velocity there is a stronger impact to form a larger and flatter splat. This was confirmed by experiment. In the SDA system, a higher initial velocity of the Ti droplets can be achieved by increasing the height of the deposition position. A splat deposited from a height of 40 mm has a diameter of 8.16 mm and a thickness of 3.84 mm, while another splat deposited with a height of 200 mm has a diameter of 15.44 mm and a thickness of 1.17 mm. However in the SDA system, due to the limitation of the chamber, the highest deposition height of the droplets is 200 mm. Therefore, simulation was carried to explore the influences of other process parameters including the temperature of the droplet, the substrate temperature and the substrate material.

The main deposition parameters of a SDA droplet become a splat are listed in Table 4.9. The initial radius of the droplet and the dynamic contact angles of the interface between the droplet and the substrate were measured from the SDA Ti droplet deposition video recorded by the high speed camera. Location of the drop centre at initial time means the deposition height (200 mm). However, as the software could not accept such a long distance to simulate, 3 mm was chosen in order to simulate the droplet impact close to the substrate. The deposition height was therefore transferred into the initial droplet velocity. The initial droplet velocity was calculated according to the law of conservation of mechanical energy (see as Equation 3) based on the deposition height 200 mm.

$$\frac{1}{2}mv^2 = mgh \tag{3}$$

In Equation 3, m is the mass of the droplet, v is the initial droplet velocity, h is the deposition height of the droplet, and g is gravitational acceleration (9.8 m/s^2). The droplet velocity of a droplet falling from 200 mm height was calculated as 2.04 m/s. The droplet material was pure Titanium, and the material “Titanium” file was made according to data from literature. (Mills, 2002) The substrate was Copper and the material “Copper” file was provided within the software. Other simulation settings like general output file settings and boundary condition settings were set as recommended based on the actual circumstances of the SDA droplet deposition.

Table 4.9 The main deposition parameters of a general SDA droplet

Initial droplet temperature (°C)	2000
Initial radius of the droplet (m)	0.26×10^{-2}
Initial droplet velocity (m/s)	2.04
Location of the drop centre at initial time (m)	0.3×10^{-2}
Initial substrate temperature (°C)	25 (room temperature)
Advancing contact angle (degrees)	150
Receding contact angle (degrees)	5

Several serial simulations were carried out in terms of different initial droplet temperature or initial substrate temperature. The simulation results are shown in Figure 4.46-47.

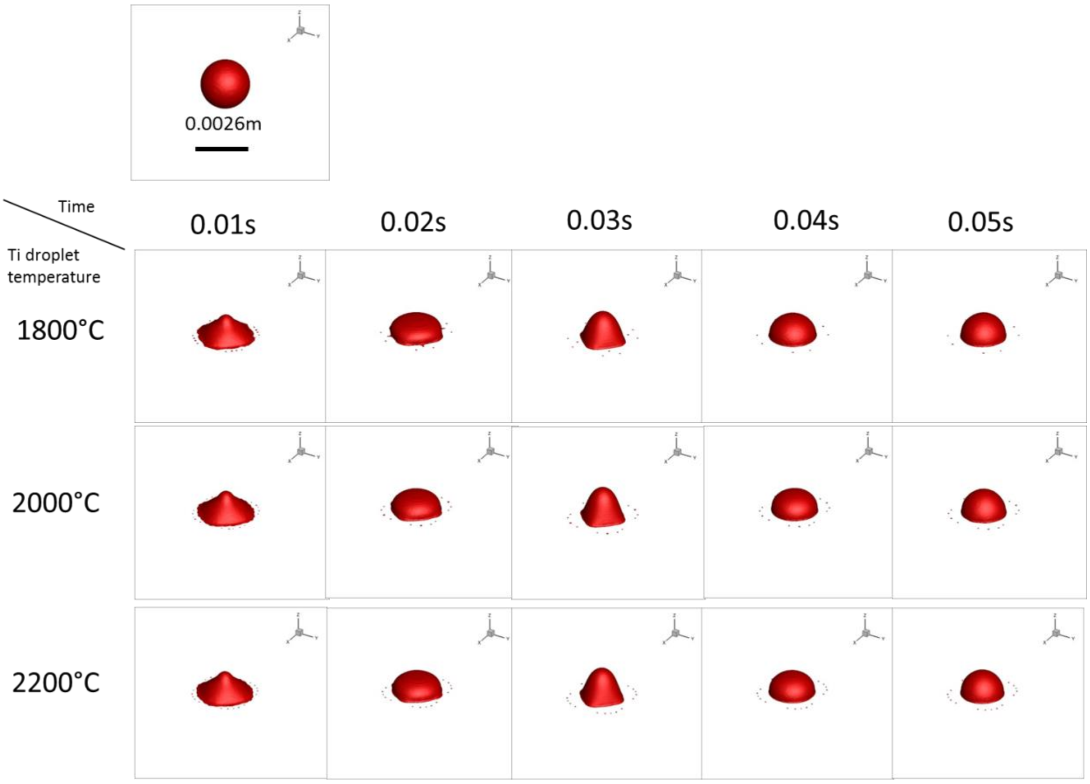

Figure 4.46 SimDrop simulations with different Ti droplet temperatures

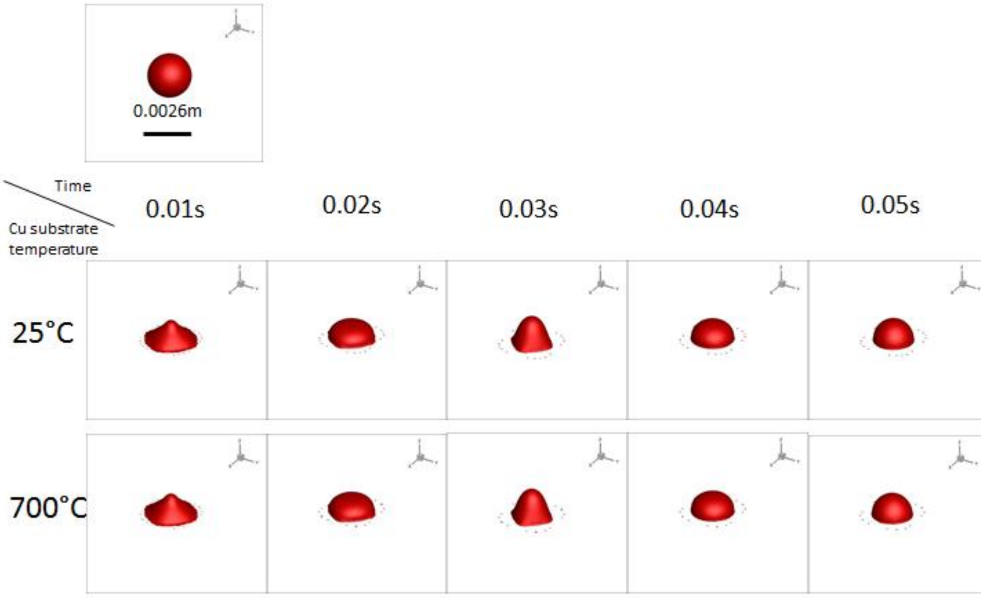

Figure 4.47 SimDrop simulations with different Cu substrate temperatures

Generally, the droplet hits the substrate first and spreads out as a flat disc. Then the material would bounce back, the splat would contract towards the centre. The middle of the splat would raise a small bump. The bump would reduce off then and the splat spread out again. The droplet would spread out and bounce back like this several times until solidified. From Figure 4.46 and 4.47, it is clear that with different Ti droplet temperature or Cu substrate temperature, the size of the splat did not change significantly. However with the increase of the Ti droplet temperature or a lower Cu substrate temperature, it seems more material would remain at the outer area. The lower substrate temperature would help the bottom layer of the splat gets solidified more quickly. The higher droplet temperature would help the droplet to stay as liquid for longer time after it bounced back and give the material more time to spread out again. Both of these two conditions can make the splat flatter.

4.6.3 Formation of a splat

A SDA Ti droplet deposited on the Cu substrate with a deposition height of 200 mm. The whole process was recorded by the high speed camera to compare with the simulation. In the experiment the solidification of the splat was found to be much faster than in the simulation. It is complete in 0.05 secs. This would indicate a cooling rate in excess of 10,000 ℃/s.

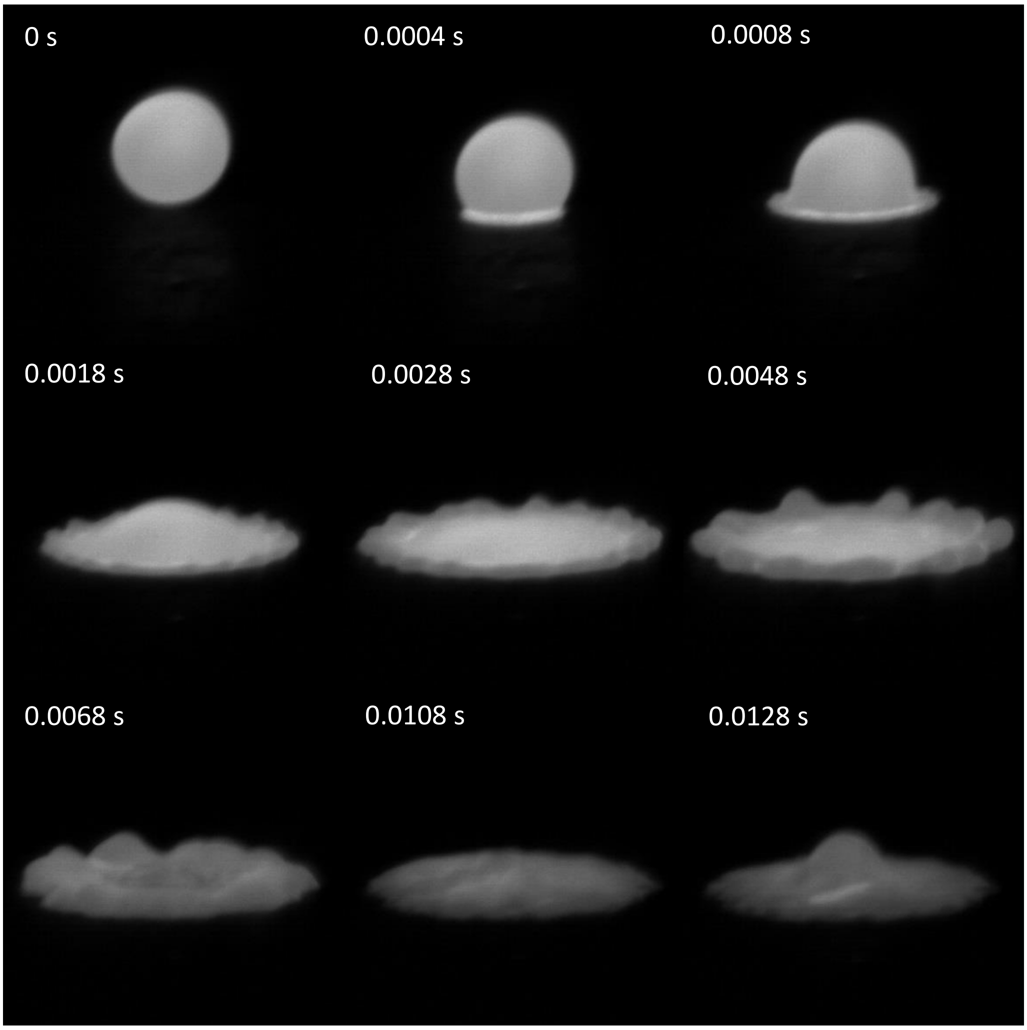

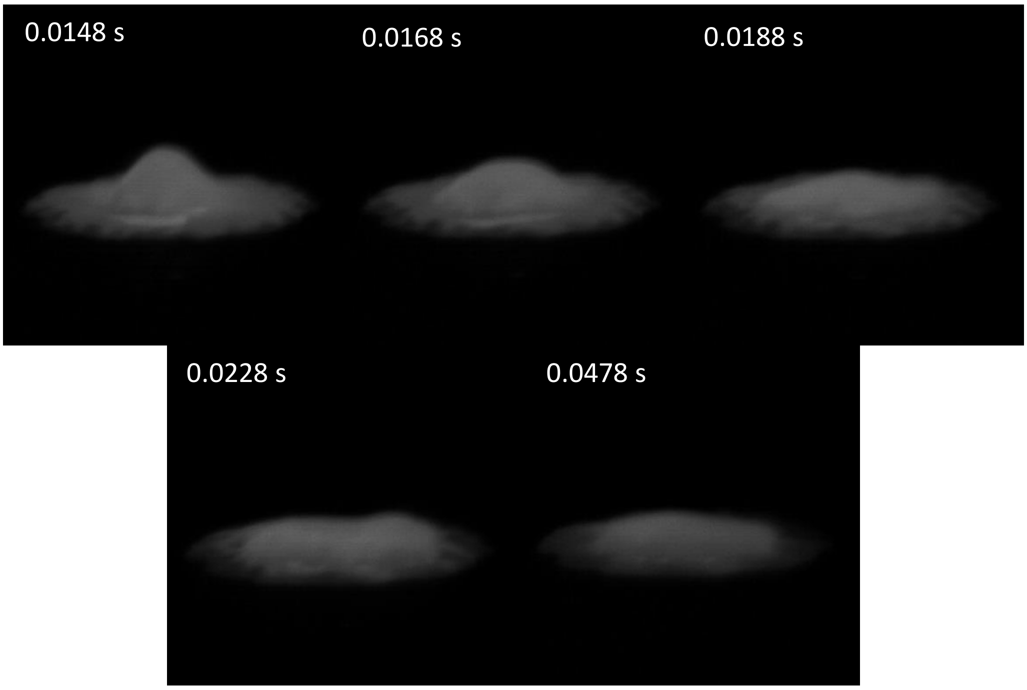

Figure 4.48 Formation of the pure Ti splat

Figure 4.48 is a series screenshots from the high speed video showing the formation of the Ti splat. When the droplet spread out and bounced back, unlike the simulation, the layer attached to the substrate was solidified quickly and only the liquid material above it bounced back and contracted towards the centre. The bouncing back height was not as high as in the simulation. As a result, the actual Ti splat was flatter than the simulated splat. Both splats have a similar size. The simulated Ti splat had a diameter of 11.7 mm, and the actual Ti splat had a diameter of 13.4 mm.

4.7 Conclusions and Summary

- Suspended Droplet Alloying (SDA) is a promising method for alloy exploration. It can produce a bulk specimen with a specific composition in just a few minutes. Ti-Al-X (e.g. V, Fe) systems have been made successfully (and 1000+ other samples in the AccMet project). All these AccMet samples were checked by the following a series of high-throughput tests such as hardness measurement, power factor measurement, EDX, XRD and so on. All the tests results are organised together in a database, the Virtual Alloy Library.

- Ti-Al-Nb is a challenging system because of Nb's high melting point. Unmelted Nb particles are the main problem in samples found to be inhomogeneous. The variation in the composition of constituent droplets also led to the inhomogeneity of the samples.

- High speed photography of the SDA process has indicated that during the formation of Ti-Al droplets and Ti-Al-Nb droplets the intermittent contact of the low melting Al wire can drag the alloyed droplet towards the Al wire as it touches leading to the exposure of Ti wire outside the alloyed droplet. Ti particles can be deposited directly if the exposed part does not melt back into the droplet in time.
- The photography also showed that during the formation of Ti-Nb droplets and Ti-Al-Nb droplets, the Nb wire is difficult to melt completely within the alloyed droplet and consequently the Nb wire may occasionally stick out of the alloyed droplet and deposit some Nb particles directly.
- During the formation of Ti-Al-Nb droplet it was observed that both small Ti

particles and and small Nb particles may deposit directly into the alloyed sample. However only Nb particles are detected in the SDA Ti-Al-Nb samples as the Ti particles can be further melted and alloyed in the melt pool present on the top of the sample while it is being manufactured. The Nb particles have a much higher melting point and are not re-melted and alloyed and hence remain visible in the final sample.

- The wire size and feed position have an important influence on suspended droplets formation. For the different target compositions, different wires diameters need to be selected to achieve a reasonably similar wire feed rates. Moreover, with a good feed position all wires can feed together and form an alloyed metal droplet.

- The relationship between laser power and wire feed rate is the key to the process. First of all, the laser power has to be high enough to melt the materials. Theoretically the more laser power applied, the more easily wires get melted. However, the laser power is restricted by the wire feed rate. The laser power can go higher if the feed rate is fast enough to allow the sample's height to build up. Otherwise, the overheating of the melt pool will lead to the contamination from the substrate. The feed rate needs to be above a certain minimum to avoid the contamination. Wires cannot feed too fast, because they may not get melted in time due to the limited laser power and short reaction time. Laser power and wire feed rate have to achieve a balance to successfully produce homogeneous samples.

- The compositional consistency of sequential Ti-46Al-8Nb droplets was found to be quite good. The Nb content was stable, and the Ti and Al content were basically stable with only one droplet showing a 3 at.% variation from the target. In production of a larger samples the small variations would be further reduced as several neighboring droplets would be further mixed together in the melting pool

- SDA process has been improved in terms of wire selection, wire feed position, wire feed rate and laser power. With a suitable selection of the process parameters homogeneous samples can be produced.
- By allowing a droplet to impact on a thick copper chill a splat is produced. In the Ti-46Al-8Nb alloy the splat had the target composition and a homogeneous microstructure. For some combinatorial investigations the adjusted method can save further time and materials.
- A simulation of the splatting process was undertaken with the commercial software SimDrop. Compared to the actual formation of the splat, the splat simulations carried by SimDrop showed somewhat different final shapes, but similar splat size to that achieved by experiment.
- The splats will be flatter on the top surface if the impact speed is high. Moreover, the splat simulations indicated that a higher droplet temperature (or a lower substrate temperature) will allow the production of splats which are flatter.

4.8 References

García-Cañadas, J., et al. (2016). "Accelerated discovery of thermoelectric materials: combinatorial facility and high-throughput measurement of thermoelectric power factor." ACS combinatorial science **18**(6): 314-319.

Mills, Kenneth C. "Recommended values of thermophysical properties for selected commercial alloys". Woodhead Publishing, 2002.

Wu, X. H., et al. (2009). "Oxidation-induced embrittlement of TiAl alloys." Intermetallics **17**(7): 540-552.

Witusiewicz, V. T., et al. (2009). "The Al–B–Nb–Ti system: IV. Experimental study and thermodynamic re-evaluation of the binary Al–Nb and ternary Al–Nb–Ti systems." Journal of Alloys & Compounds **472**(1):133-161.

Chapter 5: Ti-46Al-8Nb ALLOYS EXPLORATION BASED ON SDA

5.1. Introduction

From the literature review, it is known that Ti-46Al-8Nb alloy is one of TiAl alloy formulations with good properties (Wu, Xinhua 2006). It shows great potential as an advanced structural material operating in a high temperature environment. It has been suggested that minor addition of a fourth element, such as boron might further improve the performance of Ti-46Al-8Nb (Hu, Wu et al. 2005). In this work SDA has been applied to investigate the addition of a fourth alloying addition (Co, Hf, V, Zr). In each case the addition has been made as a replacement for some or all of the Nb.

Ti-46Al-8Nb, Ti-46Al-4Nb-4V, Ti-46Al-4Nb-4Zr, Ti-46Al-4Nb-4Co, Ti-46Al-4Nb-4Hf and Ti-46Al-8Hf alloy samples have been produced using SDA. However even using the optimised processing conditions some small Nb particles are observed in most of the samples.

The microstructure of the samples has been investigated by metallography/SEM-EDX, and XRD undertaken to determine the phases present. Tensile test were performed at ETMT (University of Oxford) to determine the mechanical properties of the alloys. After tensile testing the fracture surfaces were observed in the SEM. Comparison of the results of this work provides the initial guide which element can improve Ti-46Al-

8Nb’s properties. Cast Ti-46Al-8Nb was also characterised to compare the microstructural and properties differences between casting and SDA.

5.2. Characterization of cast Ti-46Al-8Nb

5.2.1. Microstructure

As-casted Ti-46Al-8Nb was HIPped at 1280 ^{0}C and 150 MPa for 4 hours. At 1280 ^{0}C, the sample was in the $\alpha + \gamma$ two-phase field, about 50 ^{0}C below the α single phase field. According to the Ti-Al-Nb phase diagram, the massively transformed γ would transform to a mixture of about 35% α and 65% γ at 1280 °C. However, with the influence of HIP (mainly due to the pressure), the volume fraction of α is lower than expected (Huang, Hu et al. 2007). Figure 5.1 shows the back scattered image of the polished as-casted Ti-46Al-8Nb. It shows the majority is lamellar microstructure with some of massive γ phase remaining among the lamella. The lamellar microstructure is the mixture of α_2 and γ as shown in Figure 5.1 and 5.3. The XRD results are displayed in Figure 5.4 and indicate there are α_2 (Ti_3Al) and γ (TiAl) phases in the cast Ti-46Al-8Nb. Figure 5.2 shows the back-scattered image of the etched cast Ti-46Al-8Nb which shows the massive γ grains more clearly. The dark regions are massive γ and the light area the lamellar microstructure. At the boundary of massive γ grains, there were some needle-like α phase precipitations (light phase in Figure 5.3). The spacing of lamellae in the cast Ti-46Al-8Nb sample is about 2-4 µm as Figure 5.3 shows. The cast Ti-46Al-8Nb is a homogenous sample, and it has similar microstructure and close composition all around the sample. The mean chemical composition of as-casted Ti-46Al-8Nb sample is 43.06 at.% Al, 49.21 at.% Ti and 7.73 at.% Nb.

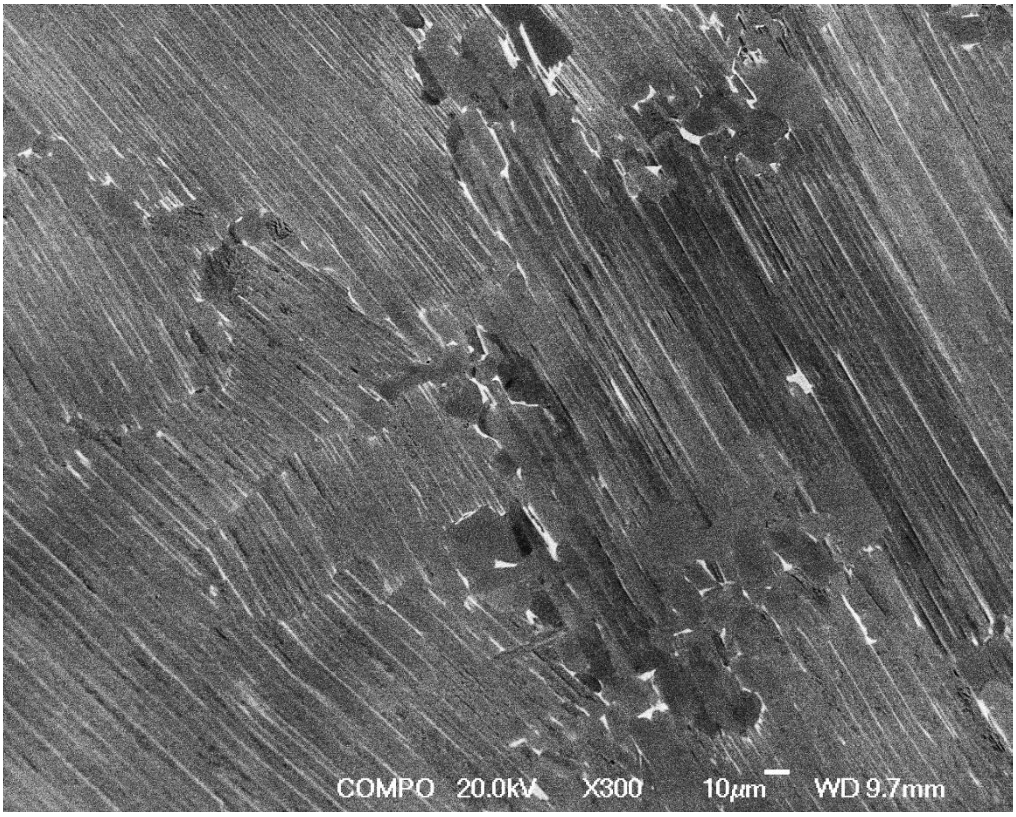

Figure 5.1 The back scattered image of polished cast Ti-46Al-8Nb

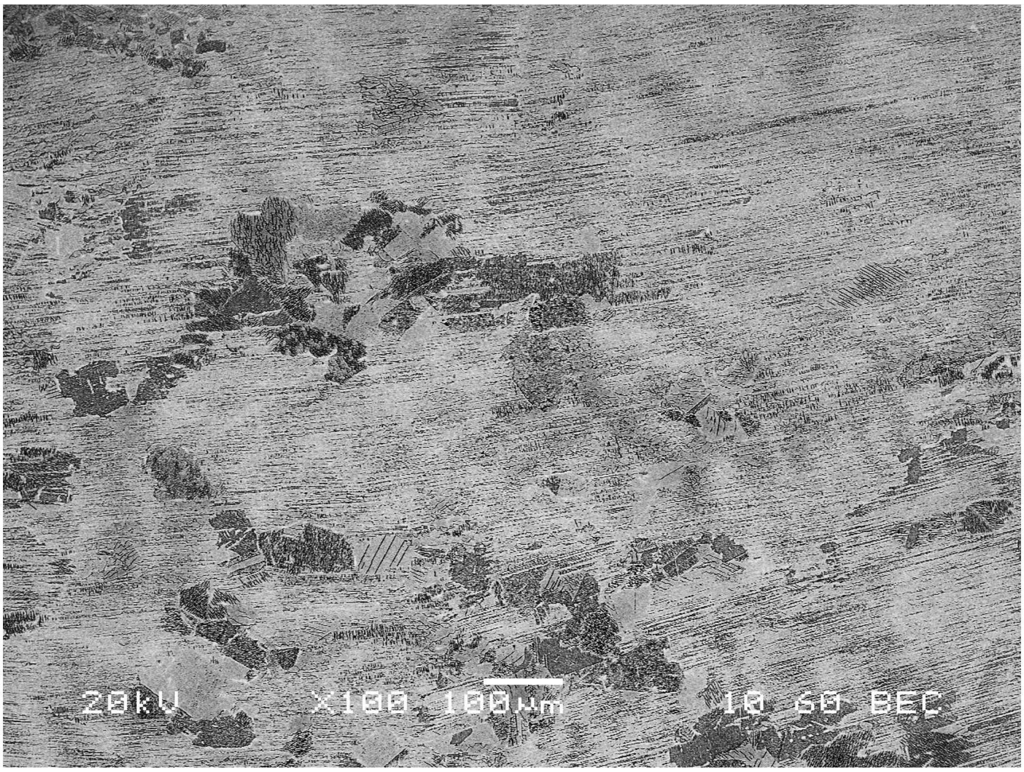

Figure 5.2 The back scattered image of etched cast Ti-46Al-8Nb

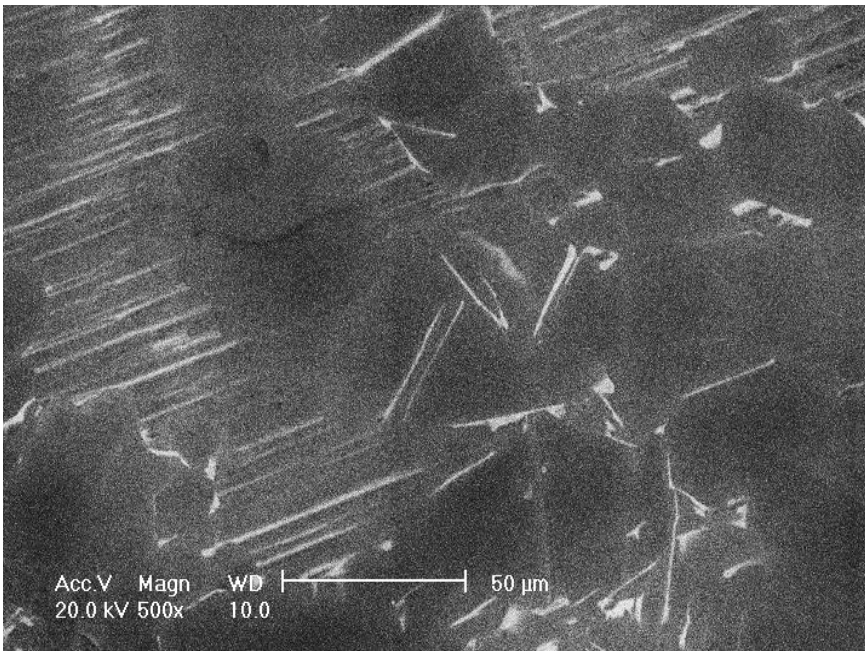

Figure 5.3 The back scattered image of polished cast Ti-46Al-8Nb

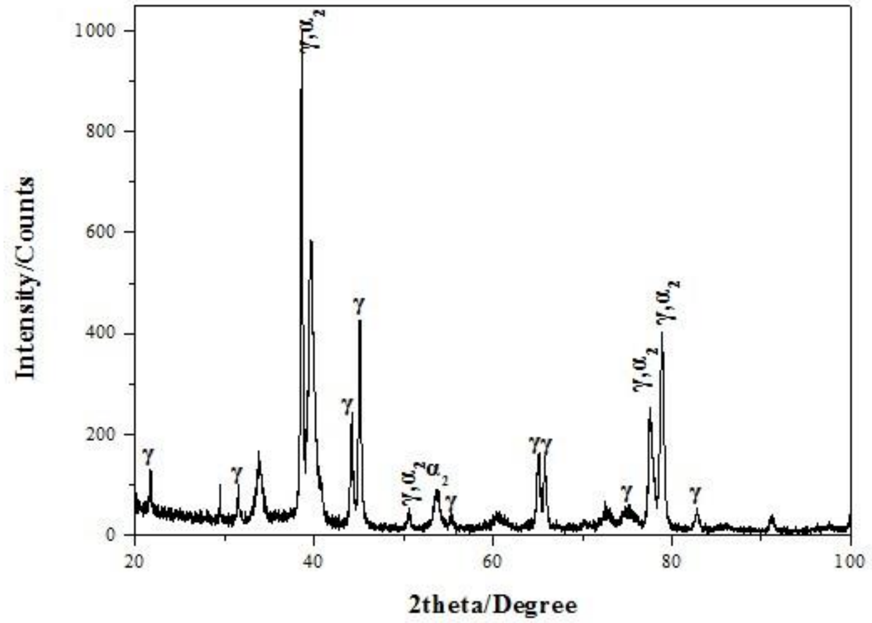

Figure 5.4 Transmission X-ray diffraction patterns of cast Ti-46Al-8Nb

5.2.2. Mechanical properties

Two tensile samples were cut from the same bulk material. The tensile stress-strain curves of them are similar as shown in Figure 5.5. The tensile properties of one of the cast Ti-46Al-8Nb sample are listed in Table 5.1. Compared to the cast Ti-46Al-8Nb sample reported in Huang's paper (Huang, Hu et al. 2007), these samples have similar UTS and lower ductility. This low ductility is mainly due to the size and shape of tensile samples which are much smaller than the standard tensile samples. The ETMT sample's size is shown in Figure 3.7.

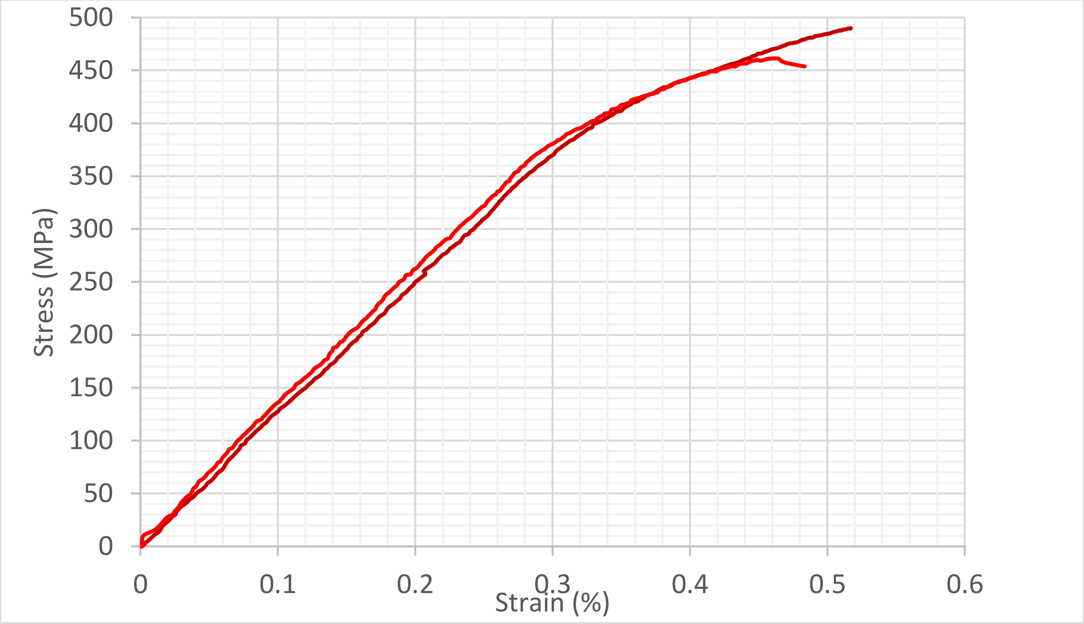

Figure 5.5 The tensile stress-strain curves of cast Ti-46Al-8Nb

Table 5.1 The comparison of tensile properties of as-casted Ti-46Al-8Nb tested by ETMT and another cast Ti-46Al-8Nb from Huang (Huang, Hu et al. 2007)

Sample	**Treatment**	**0.2% proof stress (MPa)**	**UTS (MPa)**	**Ductility (%)**
Cast Ti-46Al-8Nb tested by ETMT	HIPped for 4 h at 150 MPa at 1280 ° C	262.9	454.8	0.52
Cast Ti-46Al-8Nb from Huang	HIPped for 6 h at 150 MPa at 1280 ° C	345	436	0.8

After the tensile test, the fracture surface of cast Ti-46Al-8Nb was observed in the SEM as shown in Figure 5.6. All the fracture surfaces mentioned in this chapter were imaged using back-scattered image in order to check the chemical homogeneities of the tensile samples while observing the fracture surfaces. In Figure 5.6, cleavage planes can be clearly seen due to the lamellar microstructure.

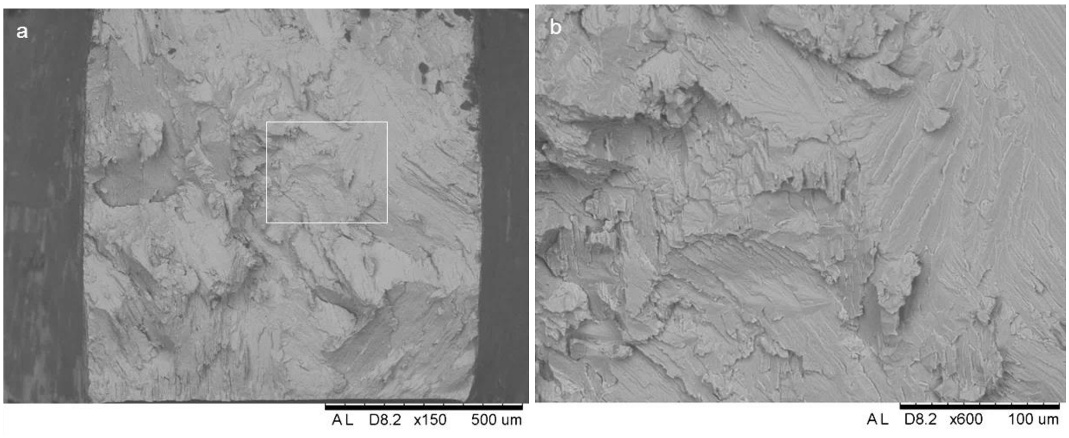

Figure 5.6 Back-scattered image of the fracture surface of as-casted Ti-46Al-8Nb, b is the zoom in region in a.

5.3. Characterization of SDA Ti-46Al-8Nb

5.3.1. Microstructure

Using the optimized SDA process parameters, Ti-46Al-8Nb samples that are homogeneous can be made although some Nb particles may still be observed in the sample. Figure 5.7-(a) shows the optical image of a SDA Ti-46Al-8Nb with some Nb particles in it. The sample was HIPped at 1260 ^{0}C and 150 MPa for 4 hours to attempt to homogenize the microstructure. Figure 5.7-(b) is the optical image of the SDA Ti-46Al-8Nb after HIP. The microstructure is becoming more homogeneous with the Nb particles were starting to dissolve into the structure. The pure Nb parts in the particles have disappeared with the particles growing larger. The matrix of the sample stayed lamellar after HIP (as shown in Figure 5.9-b). The composition change of the matrix is listed in Table 5.2. HIP did not change the microstructure or composition of the matrix.

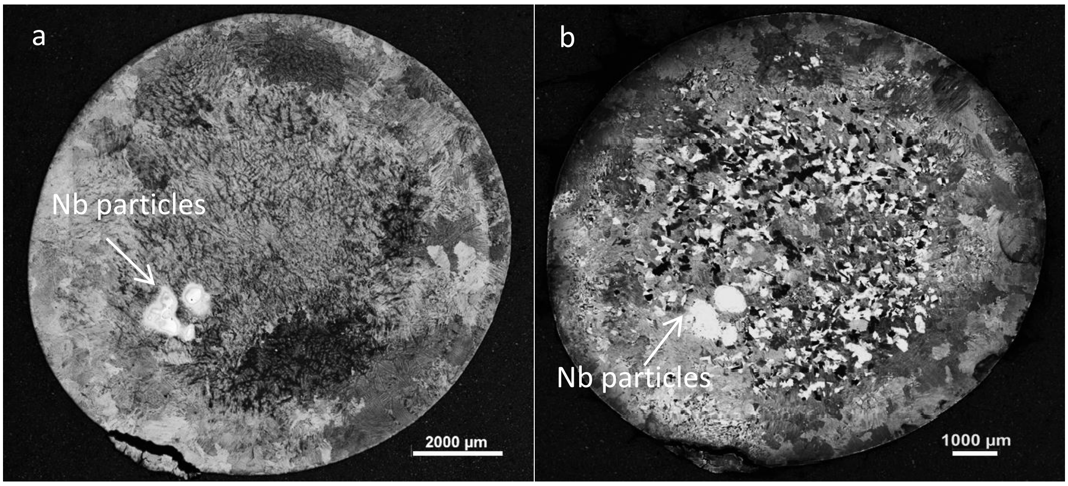

Figure 5.7 Optical images of SDA Ti-46Al-8Nb, a is before HIP and b is after HIP.

As seen in Figure 5.8, the SDA Ti-46Al-8Nb sample also retains some Ti segregation after HIP. The Ti segregation in Figure 5.8-a was like a disc with length of 2 mm and a width of 0.6 mm. Ti segregation area has the composition 57.14 at.% Ti, 35.26 at.% Al and 7.6 at.% Nb and the matrix around the segregation has a composition of 48.56 at.% Ti, 42.78 at.% Al and 8.66 at.% Nb.

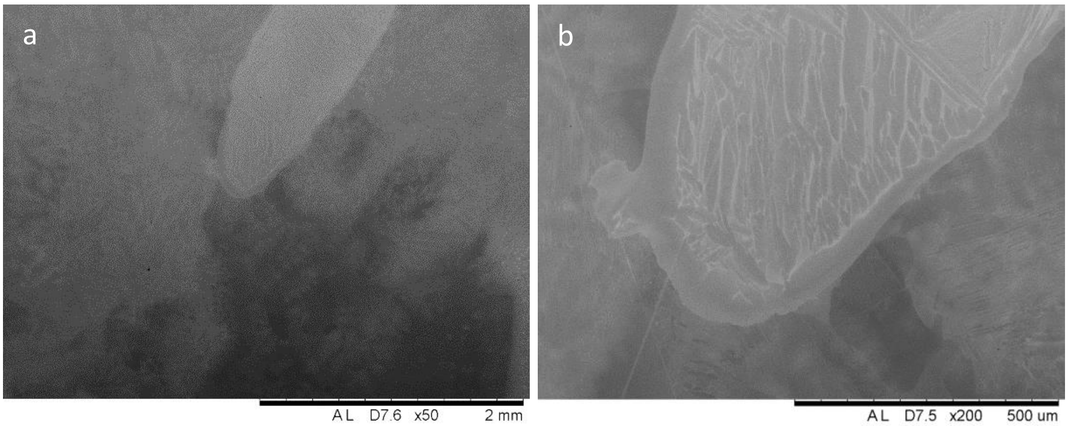

Figure 5.8 Back-scattered images of HIPped SDA Ti-46Al-8Nb, b is a zoom in part of a

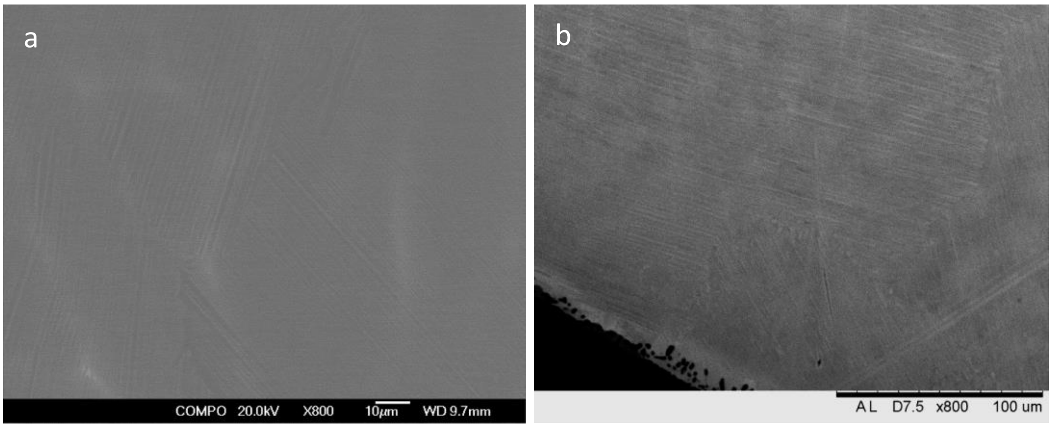

Figure 5.9 Back-scattered images of SDA Ti-46Al-8Nb, a is before HIP and b is after HIP.

Table 5.2 The chemical composition of the matrix in SDA Ti-46Al-8Nb

Treatment	Al (at.%)	Ti (at.%)	Nb (at.%)
As-built (before HIP)	43.45	48.25	8.3
HIPped	43.29	47.92	8.79

After HIP, the sample had an oxidized layer at the surface of the sample, see Figure 5.10. The oxidized layer has a width of around 50 μm. The black particles in the diffusion layer are Aluminum oxide (Al_2O_3).

Figure 5.11 shows Nb-rich particle in SDA Ti-46Al-8Nb after HIP. The Nb-rich particle after HIP has a diameter of 0.7 mm. In the middle of the Nb-rich particle, there is still pure Nb part marked as Region 1 in Figure 5.11. Near the Nb-rich particle, there are regions have a lower Nb content than the target value like Region 3 in Figure 5.11 and regions like Region 4 have more Nb in it than expected. As for the rest matrix like Region 5, it has a close composition compared to the target formulation. Chemical compositions around the Nb-rich particle in the HIPped SDA Ti-46Al-8Nb are listed in Table 5.3.

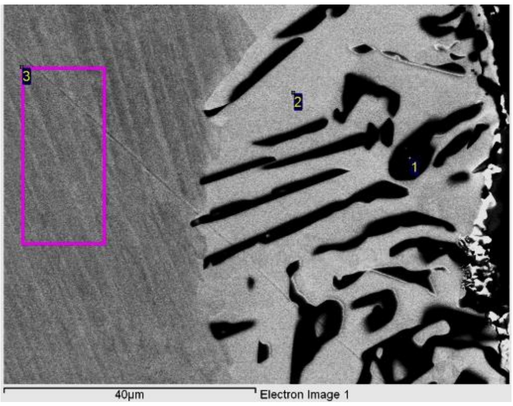

Figure 5.10 Back-scattered image of HIPped SDA Ti-46Al-8Nb

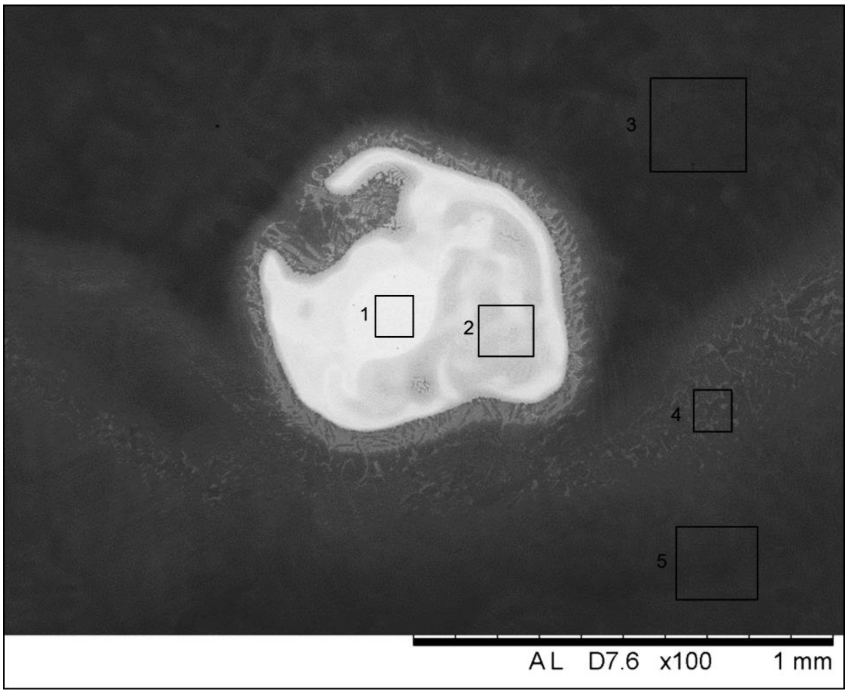

Figure 5.11 Back-scattered image of HIPped SDA Ti-46Al-8Nb

Table 5.3 Chemical composition around the Nb-rich particle in the HIPped SDA Ti-46Al-8Nb

Position (shown in Figure 5.11)	Al (at.%)	Ti (at.%)	Nb (at.%)
1	-	-	100
2	24.98	26.72	48.3
3	45.49	48.66	5.85
4	41.91	45.6	12.49
5	43.28	47.71	9.01

5.3.2. Phases

There are many small peaks in the transmission X-ray diffraction patterns of SDA Ti-46Al-8Nb as shown in Figure 5.12. Although the background signals are quite confused, high peaks from α_2 and γ phases can be distinguished clearly.

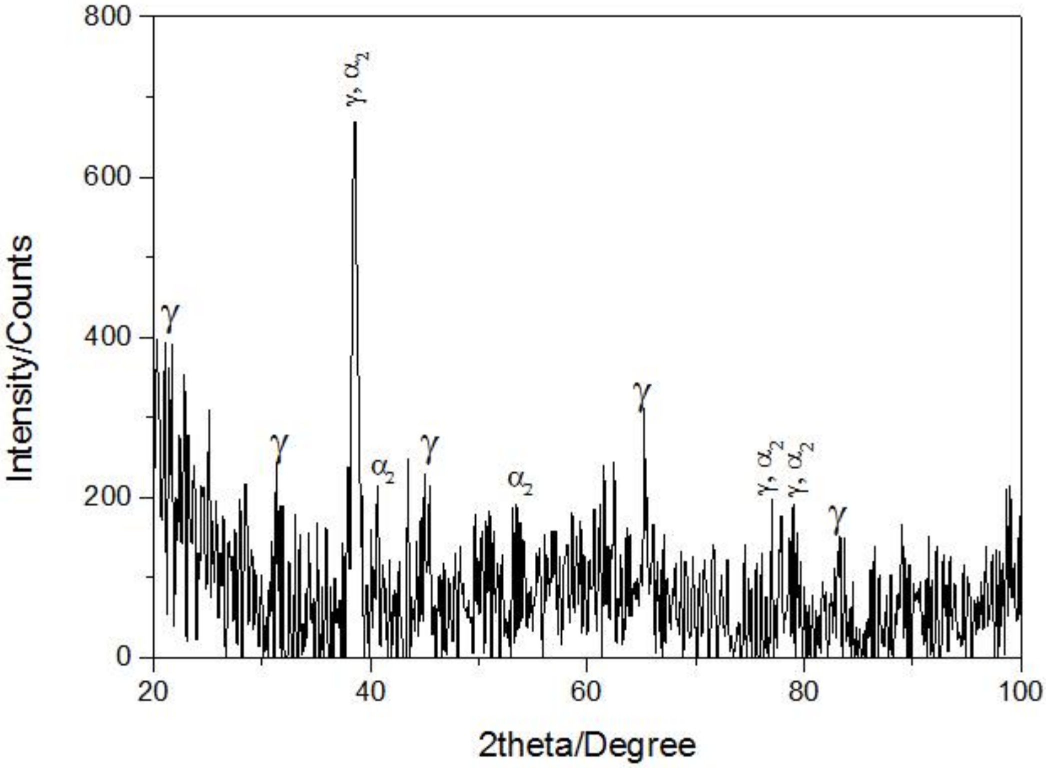

Figure 5.12 Transmission X-ray diffraction patterns of SDA Ti-46Al-8Nb

5.3.3. Mechanical properties

The SDA Ti-46Al-8Nb sample was built to a height of 50 mm, with a diameter of about 15 mm. This was large enough to cut two of the ETMT tensile samples. The sample was HIP processed prior to cutting. In Figure 5.13, two SDA Ti-46Al-8Nb samples ETMT test results are shown. These two curves are quite different. One of the samples (SDA

Ti-46Al-8Nb-1) failed at the beginning, and its ultimate tensile strength (UTS) was even below 50 MPa. However the other sample has a UTS of 443 MPa and ductility of 0.48%.

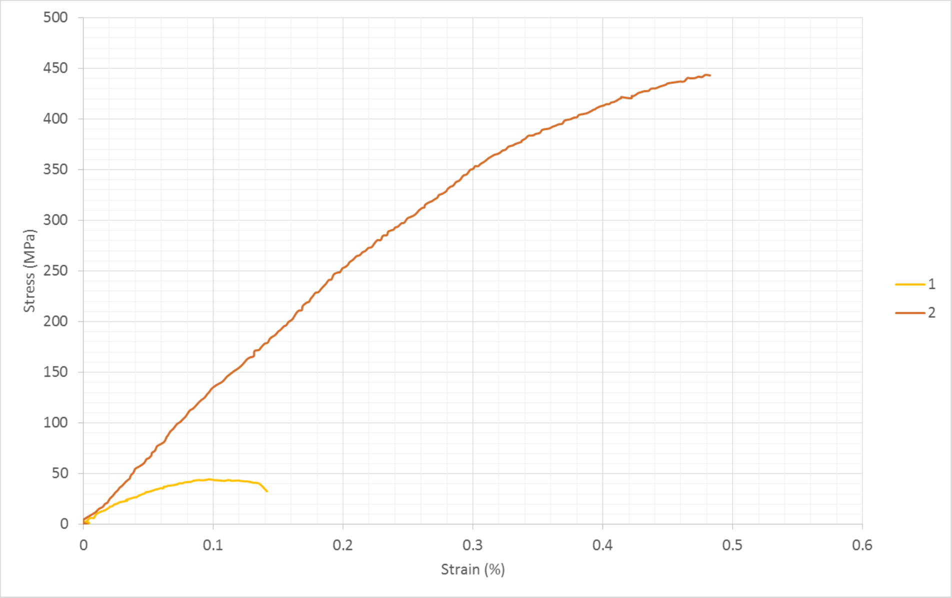

Figure 5.13 The tensile stress-strain curves of SDA Ti-46Al-8Nb

Table 5.4 The tensile properties of two SDA Ti-46Al-8Nb ETMT samples

Sample	**0.2% proof stress (MPa)**	**UTS (MPa)**	**Ductility (%)**
SDA Ti-46Al-8Nb-1	-	43.7	0.14
SDA Ti-46Al-8Nb-2	253.82	443.5	0.48

By observing the fracture surface, it is known that SDA Ti-46Al-8Nb-1 failed so early because in one half of the sample was Nb-rich particle. As Figure 5.14-a shows, the bottom brighter part is the Nb-rich region which has a Nb content of 40-60 at.%. The upper part of SDA Ti-46Al-8Nb-1 has typical cleavage planes due to lamellar microstructure while the bottom Nb-rich part has a relatively flat fracture surface.

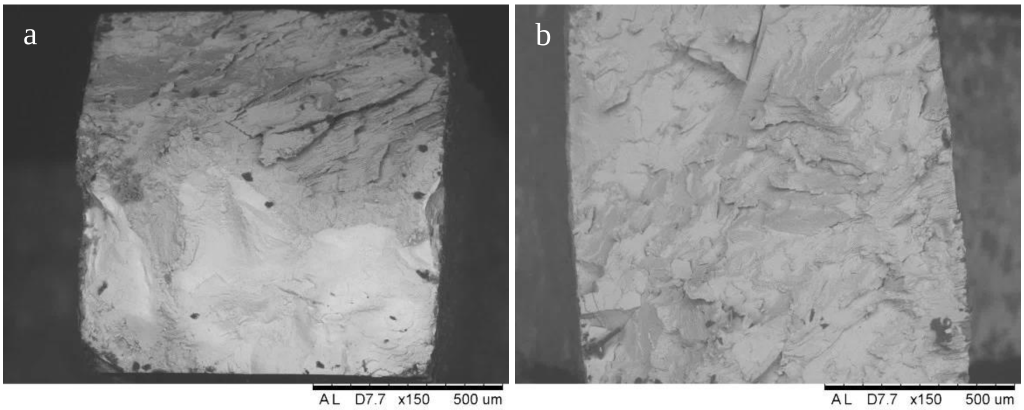

Figure 5.14 Back-scattered images of the fracture surface of two SDA Ti-46Al-8Nb ETMT samples, a is SDA Ti-46Al-8Nb-1 and b is SDA Ti-46Al-8Nb-2.

Because Nb-rich particles are only a small part of the SDA Ti-46Al-8Nb sample, and several ETMT samples were cut from the whole sample, some tensile samples may have the Nb-rich part while some of them may be homogeneous. SDA Ti-46Al-8Nb-2 is such a homogeneous sample confirmed by its fracture surface showed in Figure 5.14-b. Therefore the tensile result of SDA Ti-46Al-8Nb-2 is more representative of Ti-46Al-8Nb. The tensile properties of SDA Ti-46Al-8Nb are listed in Table 5.4.

5.4. Characterization of Ti-46Al-4Nb-4V

5.4.1. Microstructure

Based on SDA Ti-46Al-8Nb, 4 at.% V was added to replace Nb. A new sample was built with the formulation of 46 at.% Ti, 46 at.% Al, 4 at.% Nb and 4 at.% V. Ti-46Al-4Nb-4V was quite homogeneous, and with no observable inherited Nb particles. The composition of the Ti-46Al-4Nb-4V is 48.66 at.% Ti, 43.02 at.% Al, 3.77 at.% Nb and 4.54 at.%. It is fully lamellar microstructure all around the sample except the edge's oxidized layer. Ti-46Al-4Nb-4V's lamellar microstructure is shown in Figure 5.15, and it can be seen in Figure 5.15-b that the spacing of the lamellae is about 1 µm. Figure 5.16 is the edge of the Ti-46Al-4Nb-4V sample. The dark particles in the diffused layer are aluminum oxide (Al_2O_3) according to the EDX results.

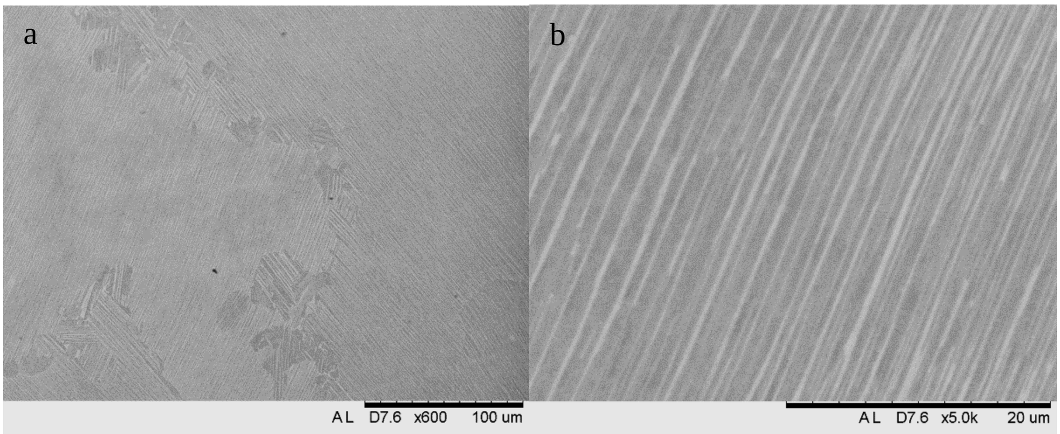

Figure 5.15 Back-scattered images of Ti-46Al-4Nb-4V, a has a magnification of 600 times and b has a magnification of 5000 times.

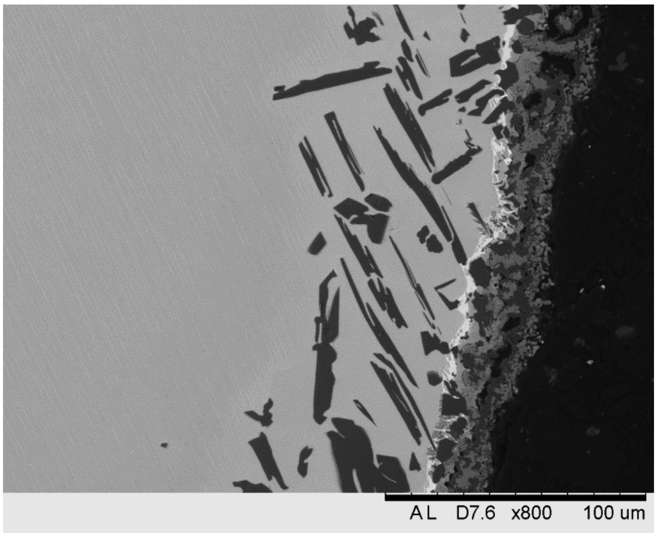

Figure 5.16 Back-scattered images of Ti-46Al-4Nb-4V

5.4.2. Phases

Figure 5.17 is the transmission X-ray diffraction patterns of Ti-46Al-4Nb-4V, and it also has a lot of background signals. α_2 and γ's peaks can be distinguished in the pattern. Combined with Ti-46Al-4Nb-4V's fully lamellar microstructure, α_2 and γ phases in Ti-46Al-4Nb-4V can be confirmed.

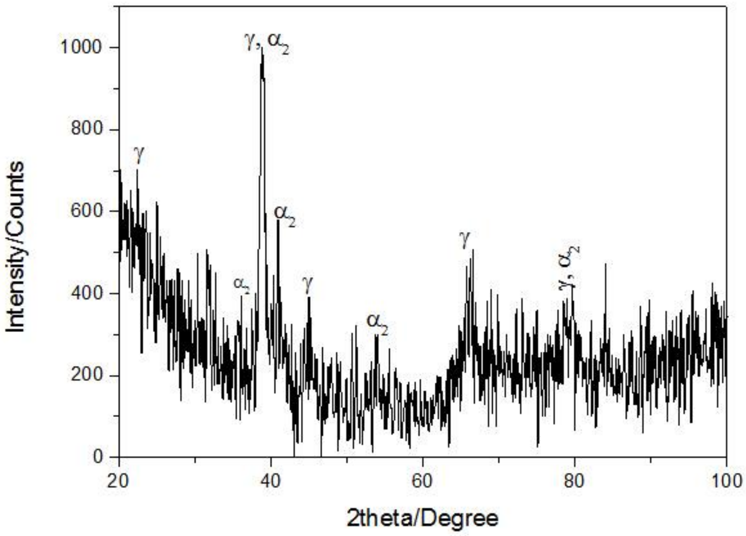

Figure 5.17 Transmission X-ray diffraction patterns of Ti-46Al-4Nb-4V

5.4.3. Mechanical properties

The two Ti-46Al-4Nb-4V ETMT samples exhibited different mechanical performances. Ti-46Al-4Nb-4V-1 had a similar tensile stress-strain curve as Ti-46Al-4Nb-4V-2 before it failed, see Figure 5.18. However, Ti-46Al-4Nb-4V-1's ductility is only 0.48, while Ti-46Al-4Nb-4V-2 has a ductility of 1.18. The UTS of Ti-46Al-4Nb-4V-1 and 2 are 303.8 MPa and 343.2 MPa respectively.

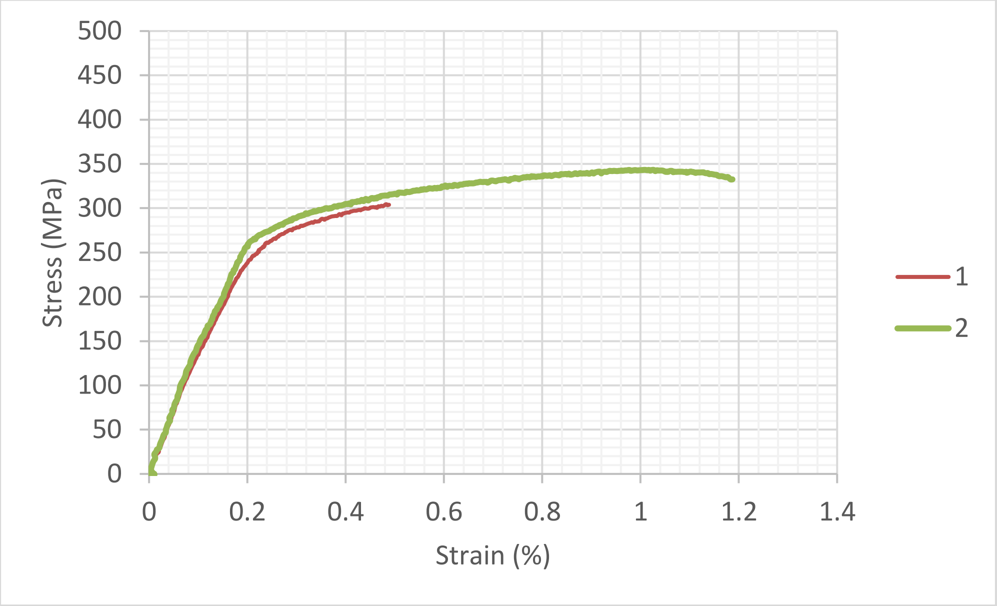

Figure 5.18 The tensile stress-strain curves of Ti-46Al-4Nb-4V

Table 5.5 The tensile properties of two Ti-46Al-4Nb-4V ETMT samples

Sample	0.2% proof stress (MPa)	UTS (MPa)	Ductility (%)
Ti-46Al-4Nb-4V-1	238.3	303.8	0.49
Ti-46Al-4Nb-4V-2	256.7	343.2	1.18

From the fracture surface it is clear that Ti-46Al-4Nb-4V-1 has a much lower ductility than Ti-46Al-4Nb-4V-2 due an Nb-rich particle in sample 1. On the fracture surface of Ti-46Al-4Nb-4V-1, there was a spindle shape hole left by an Nb-rich particle. The Nb-rich particle was about 300-500 µm diameter, and has broken away from the sample completely. The surface of the remaining hole was quite smooth as Figure 5.19-d shows. Figure 5.19-b is the Nb diffusion zone after HIP with a Nb content of 14 at.%, and the dark phase in it has more cleavage planes than the surrounding. SDA Ti-46Al-8Nb-1 was also failed because of the Nb-rich particles, however unlike SDA Ti-46Al-8Nb-1, Ti-46Al-4Nb-4V-1 did not fail easily at the beginning. The Nb particle in SDA Ti-46Al-8Nb-1 is larger than the one in Ti-46Al-4Nb-4V-1. Ti-46Al-4Nb-4V-1 behaved normally like Ti-46Al-4Nb-4V-2 before it failed. Unlike SDA Ti-46Al-8Nb-1's relatively flat fracture surface, the size of the Nb-rich particle and the microstructure of the diffusion zone in Ti-46Al-4Nb-4V-1 might be the reason that it did not fail so early.

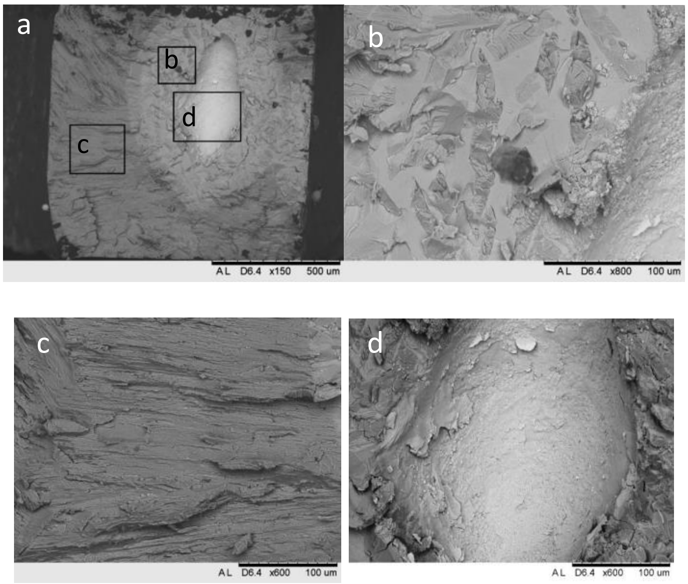

Figure 5.19 Back-scattered images of the fracture surfaces of Ti-46Al-4Nb-4V-1 ETMT sample, a is the overall view under the magnification of 150 times, and b, c, d are the zoom in parts of a.

The Ti-46Al-4Nb-4V sample had been checked for homogeneity by metallography/SEM so it was disappointing that an Nb-rich particle was found in the Ti-46Al-4Nb-4V-1 ETMT sample. However this can happen as the Nb-rich particles are distributed randomly in the Ti-46Al-4Nb-4V sample, and the SEM checked sample and ETMT samples were cut from the Ti-46Al-4Nb-4V sample in different parts as illustrated in Figure 5.20. The bottom part was cut out from the Ti-46Al-4Nb-4V sample along the dotted line (cut plane shown as Figure 5.20-1) for SEM checking. There are no Nb-rich particles on this plane, therefore the sample showed completely homogeneous when checking. ETMT samples were cut from the upper part. Nb-rich particles may lay in the gauge area of tensile sample like Figure 5.20 shows (ETMT sample 3 in the diagram would be the Ti-46Al-4Nb-4V-1 sample).

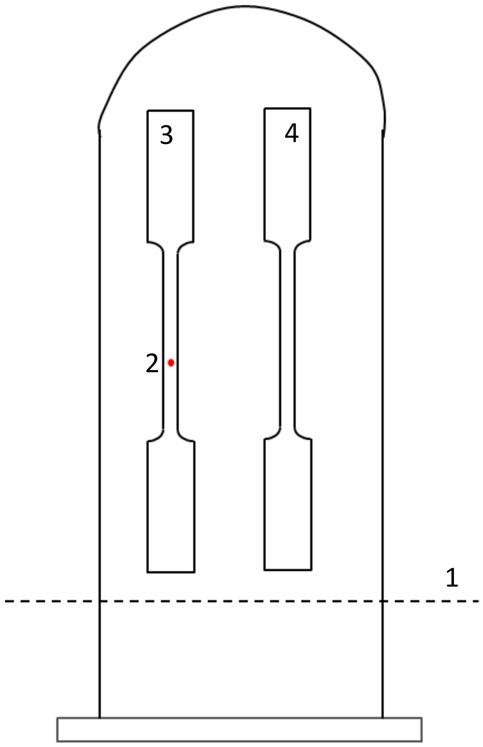

Figure 5.20 Schematic diagram of the Ti-46Al-4Nb-4V sample's cutting works, 1 is cutting plane, 2 is the Nb-rich particle, 3 and 4 are ETMT samples.

Ti-46Al-4Nb-4V-2 sample is a homogeneous sample without Nb-rich particles. Its fracture surface has many cleavage planes as shown in Figure 5.21, and many layers are almost perpendicular to the tensile force direction. As a result, Ti-46Al-4Nb-4V-2 showed quite a good ductility of 1.18.

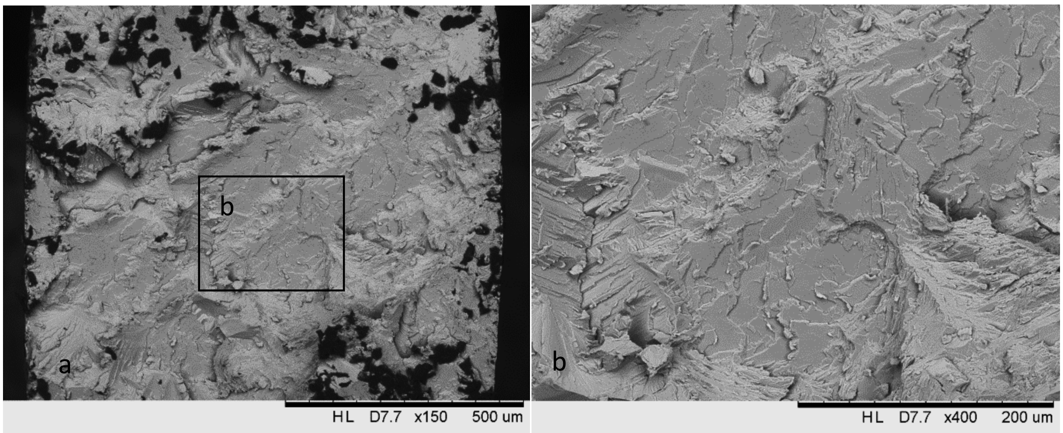

Figure 5.21 Back-scattered images of the fracture surfaces of Ti-46Al-4Nb-4V-2 ETMT sample, b is the zoom in region in a.

5.5. Characterization of Ti-46Al-4Nb-4Zr

5.5.1. Microstructure

Ti-46Al-4Nb-4Zr was also found to have Nb-rich particles as shown in Figure 5.22. The particles have 46-95 at.% Nb mixed with Al and Ti. The diffusion layer of these particles is about 0.3 mm thick generally and diffused further in some directions like Area 2 in Figure 5.22. There are many needle-like rods in the diffusion layer. According to the EDX and XRD results, these rods are γ precipitates with a content of 45.43 at.% Al, 41.92 at.% Ti and 12.66 at.% Nb. Area 1 (shown in Figure 5.22) is close to the Nb-rich particle, and has a composition of 35.71 at.% Al, 44.45 at.% Ti, 3.79 at.% Zr and 16.05 at.% Nb. The needle-like rods were small when it close to the Nb-rich particles, and became bigger when the Nb content is decreased like Area 2 with a composition of 37.29 at.% Al, 51.9 at.% Ti, 3.77 at.% Zr and 7.04 at.% Nb.

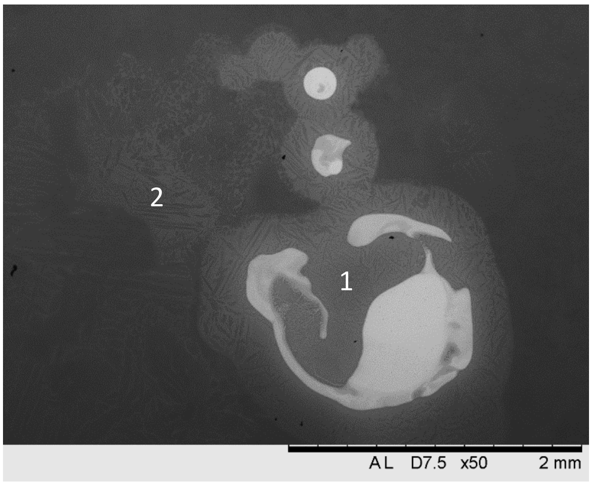

Figure 5.22 Back-scattered image of Ti-46Al-4Nb-4Zr showing the Nb-rich particles in it.

Like SDA Ti-46Al-8Nb, Ti-46Al-4Nb-4Zr also shows some Ti segregation as seen in Figure 5.23. The Ti segregation area (1 in Figure 5.23) has 36.14 at.% Al, 57.18 at.% Ti, 3.12 at.% Nb and 3.56 at.% Zr. The matrix (2 in Figure 5.23) has 45.04 at.% Al, 46 at.% Ti, 4.36 at.% Nb and 4.6 at.% Zr.

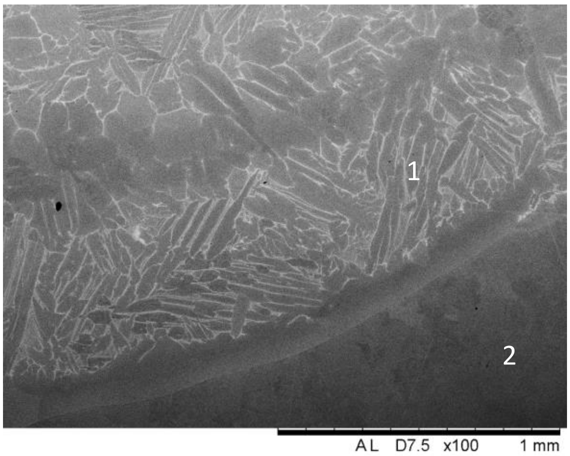

Figure 5.23 Back-scattered image of Ti-46Al-4Nb-4Zr showing the Ti segregations.

Despite the Nb-rich particles and Ti segregations, the matrix of Ti-46Al-4Nb-4Zr is fully lamellar as seen in Figure 5.24-a. The composition of the matrix is 42.98 at.% Al, 49.13 at.% Ti, 3.37 at.% Nb and 4.52 at.% Zr. The spacing of lamellar is about 1 µm according to Figure 5.24-b.

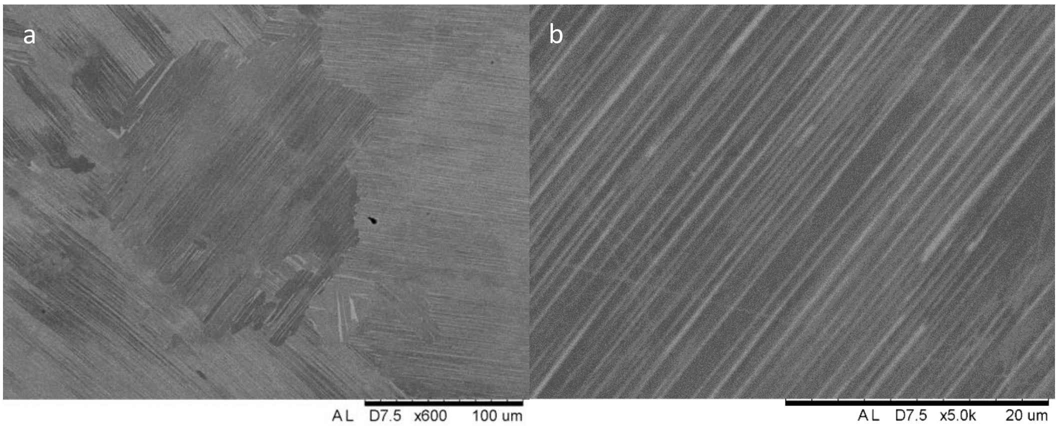

Figure 5.24 Back-scattered images of Ti-46Al-4Nb-4Zr showing the matrix lamellar.

Ti-46Al-4Nb-4Zr sample has a 70 µm thick oxidized layer after HIP shown in Figure 5.25. There are two kinds of oxides dispersed in the oxidized layer. The bright particles are aluminum oxides (Al_2O_3), and the dark particles are zirconium oxides (ZrO) according to the EDX results.

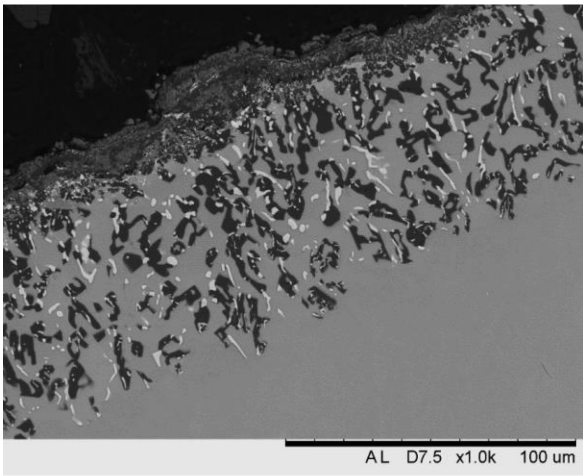

Figure 5.25 Back-scattered image of Ti-46Al-4Nb-4Zr's edge

HIP was undertaken in order to homogenize the microstructure and remove defects like cracks and pores. However, in Ti-46Al-4Nb-4Zr some cracks and pores were observed (see in Figure 5.26). The cracks were not closed completely after being HIPped at 1260 ^{0}C and 150 MPa for 4 hours suggesting a more severe heat treatment may be required to densify this alloy.

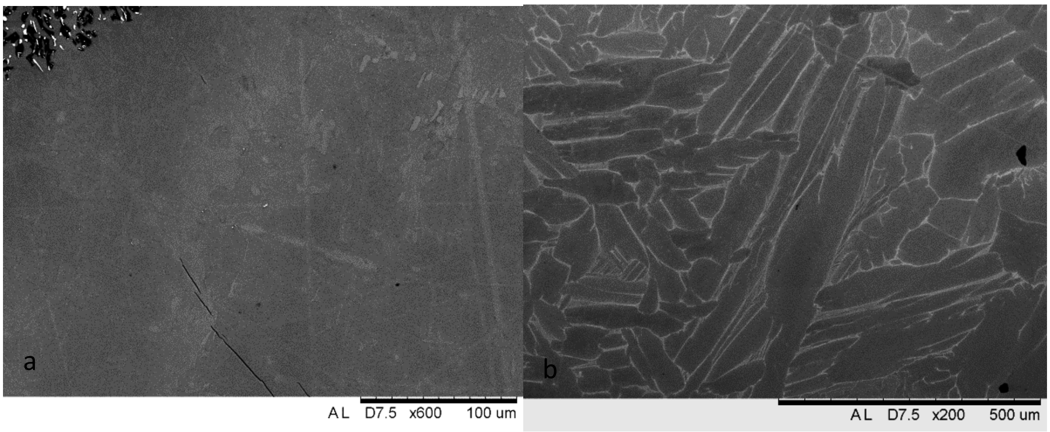

Figure 5.26 Back-scattered images of Ti-46Al-4Nb-4Zr

5.5.2. Phases

According to the transmission X-ray diffraction patterns of Ti-46Al-4Nb-4Zr, there are two phases in Ti-46Al-4Nb-4Zr, α_2 and γ phases.

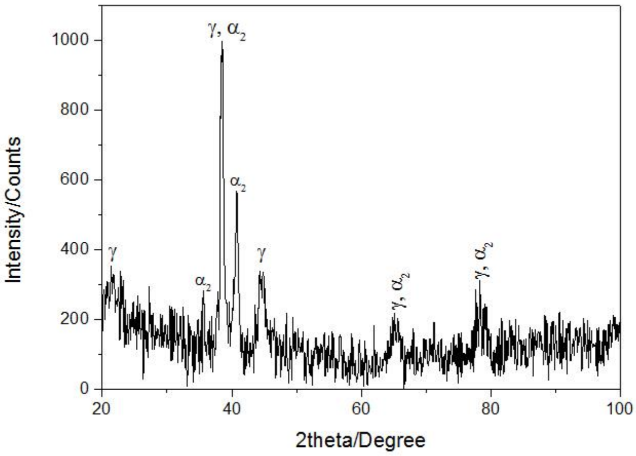

Figure 5.27 Transmission X-ray diffraction patterns of Ti-46Al-4Nb-4Zr

5.5.3. Mechanical properties

Two Ti-46Al-4Nb-4Zr ETMT samples behaved the same at the beginning of the tensile tests, and then Ti-46Al-4Nb-4Zr-2 was failed earlier than Ti-46Al-4Nb-4Zr-1. Their tensile stress-strain curves are shown in Figure 5.28, and the detailed tensile properties are listed in Table 5.6.

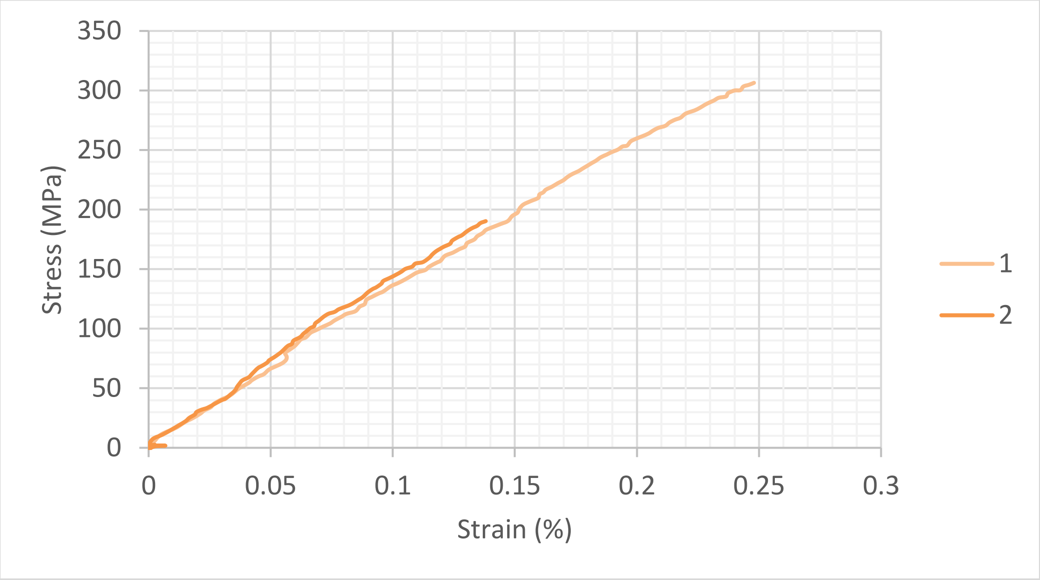

Figure 5.28 The tensile stress-strain curves of Ti-46Al-4Nb-4Zr

Table 5.6 The tensile properties of two Ti-46Al-4Nb-4Zr ETMT samples

Sample	**0.2% proof stress (MPa)**	**UTS (MPa)**	**Ductility (%)**
Ti-46Al-4Nb-4Zr-1	261.7	306.4	0.25
Ti-46Al-4Nb-4Zr-2	-	190.3	0.14

Both Ti-46Al-4Nb-4Zr ETMT sample are homogeneous according to their fracture surfaces. There is no Nb-rich particles been observed at their fracture surfaces. However, there is a crack at the fracture surface of Ti-46Al-4Nb-4Zr-2 shown in Figure 5.29-c. Ti-46Al-4Nb-4Zr-2 has cracks within its gauge length, and this may be the reason Ti-46Al-4Nb-4Zr-2 failed earlier than Ti-46Al-4Nb-4Zr-1.

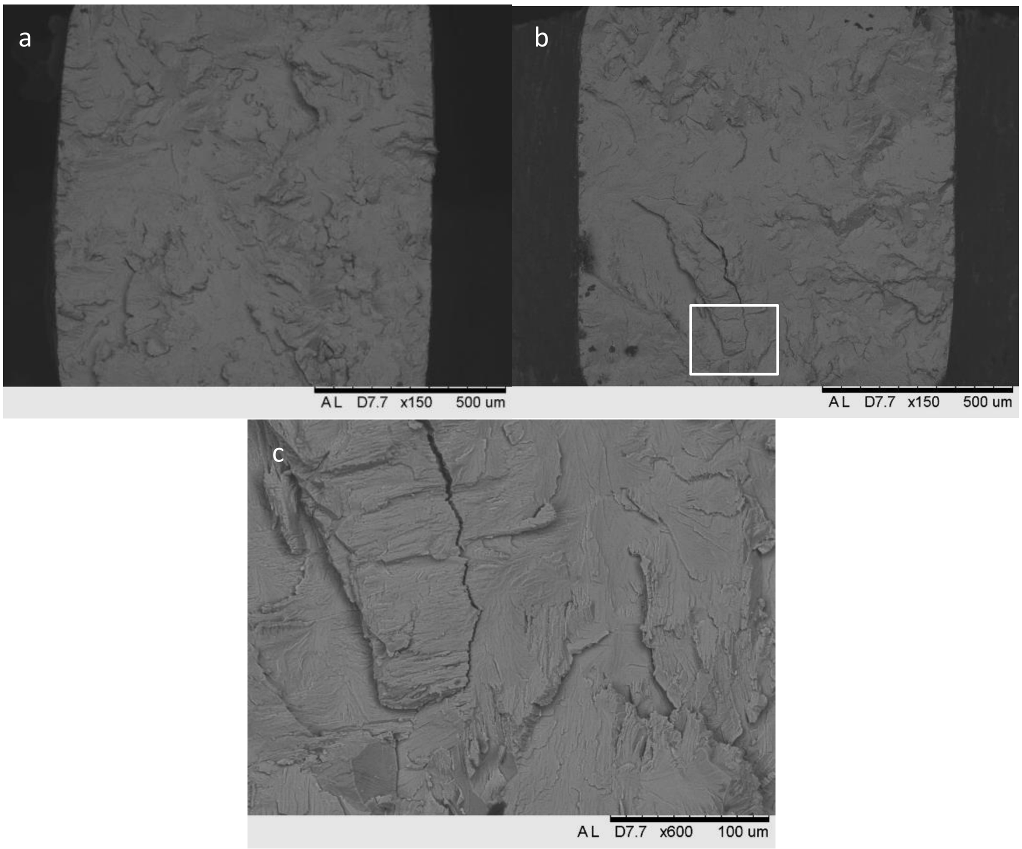

Figure 5.29 Back-scattered images of fracture surfaces of Ti-46Al-4Nb-4Zr ETMT samples, a is Ti-46Al-4Nb-4Zr-1, b is Ti-46Al-4Nb-4Zr-2, and c is the zoom in part of b.

5.6. Characterization of Ti-46Al-4Nb-4Co

5.6.1. Microstructure

Ti-46Al-4Nb-4Co sample was found to have a large Nb-rich ball with a diameter of 1mm shown in Figure 5.30. The chemical compositions around the Nb-rich ball are listed in Table 5.7. The Nb-rich ball has 72.59 at.% Nb mixed with Al, Ti and even a little Co in it. In the diffusion layer, Ti, Al and Co's contents are basically stable while Nb's content decreases as move outwards from the Nb-rich ball. The needle shape rods in the diffusion zone also get bigger at outer areas.

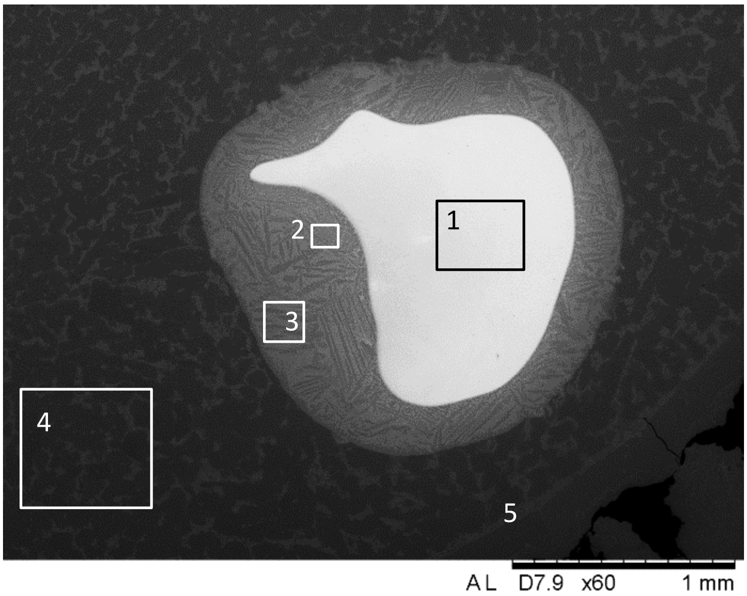

Figure 5.30 Back-scattered images of Ti-46Al-4Nb-4Co showing Nb-rich particle

Table 5.7 Chemical compositions around the Nb-rich particle in the Ti-46Al-4Nb-4Co

Position (shown in Figure 5.30)	Al (at.%)	Ti (at.%)	Nb (at.%)	Co (at.%)
1	12.47	13.27	72.59	1.67
2	37.33	40.02	20.59	2.06
3	37.75	44.52	15.05	2.69
4	44.52	47.39	3.89	4.19

Unlike other HIPped SDA samples, Ti-46Al-4Nb-4Co does not have an oxidized layer. Instead, there are three parts at the edge of Ti-46Al-4Nb-4Co. Firstly there are many small balls with high Co content aggregated at the edge. Then a low Co content band with a width of 140 µm lies next to the round high Co content balls. Between the band and the matrix of the sample, there is still a ring like bright phase (3 in Figure 5.31 and 5 in Figure 5.30) with a high Co content again.

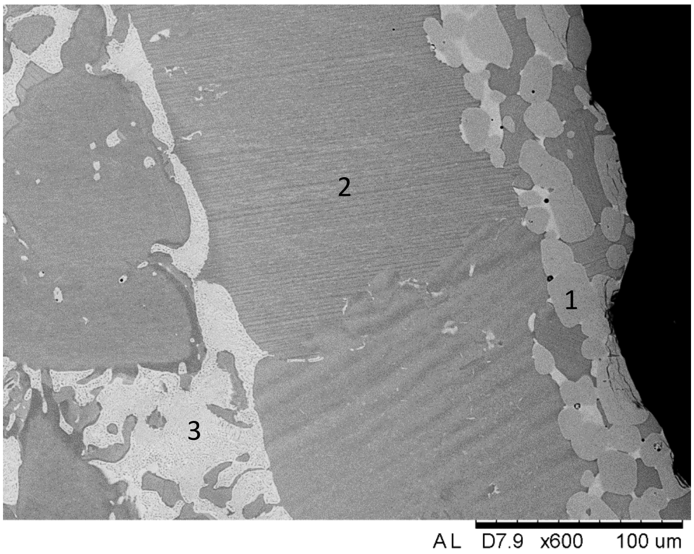

Figure 5.31 Back-scattered images of Ti-46Al-4Nb-4Co's edge

Table 5.8 Chemical compositions at the edge of Ti-46Al-4Nb-4Co

Position (shown in Figure 5.31)	Al (at.%)	Ti (at.%)	Nb (at.%)	Co (at.%)
1	32.18	50.7	1.26	15.87
2	39.22	55.85	3.84	1.09
3	41.16	36.4	3.16	19.28

The matrix of Ti-46Al-4Nb-4Co is quite different compared to other TiAlNb-X samples. Instead of a lamellar microstructure, high Co content precipitates are distributed uniformly in the matrix like Figure 5.32 shows. According to the EDX results (see in Table 5.9), the precipitates may be $AlCo_2Ti$.

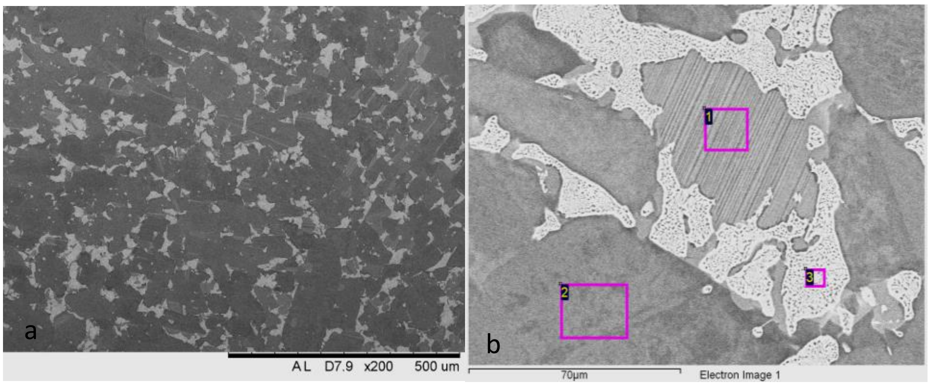

Figure 5.32 Back-scattered images of Ti-46Al-4Nb-4Co's matrix with different magnifications

Table 5.9 Chemical composition of the matrix of Ti-46Al-4Nb-4Co

Position (shown in Figure 5.32)	Al (at.%)	Ti (at.%)	Nb (at.%)	Co (at.%)
1	40.16	54.9	3.97	0.97
2	46.23	48.41	4.32	1.04
3	39.98	37.54	2.92	19.56

5.6.2. Phases

The transmission X-ray diffraction patterns of Ti-46Al-4Nb-4Co have a lot of confused background signals and make the peaks inconspicuous. However, Ti-46Al-4Nb-4Co has α_2 and γ phases as marked in Figure 5.33. There may be peaks from $AlCo_2Ti$ that are immerged in the background signals.

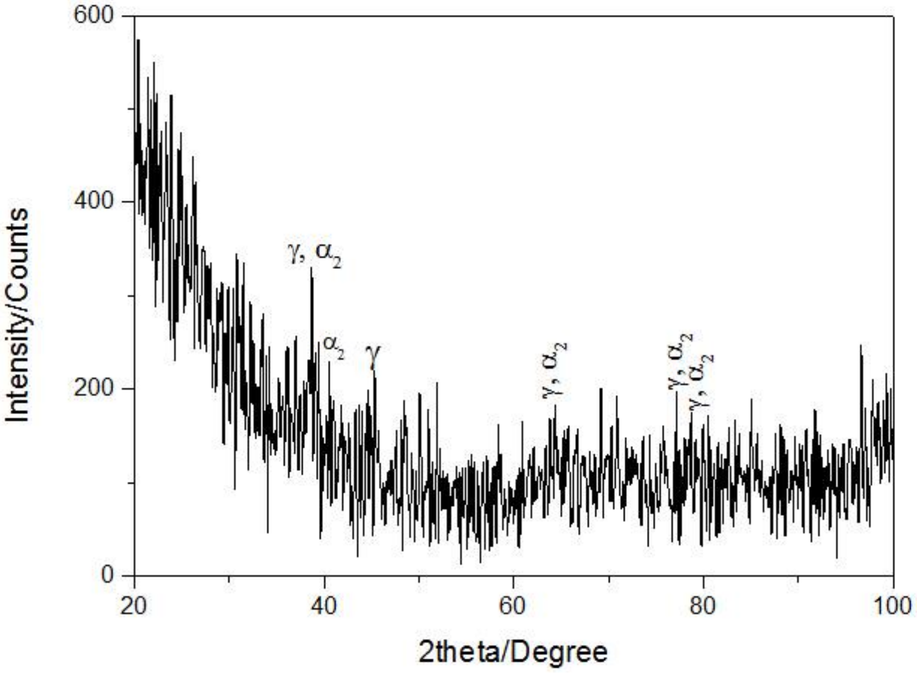

Figure 5.33 Transmission X-ray diffraction patterns of Ti-46Al-4Nb-4Co

5.6.3. Mechanical properties

Ti-46Al-4Nb-4Co was so brittle that it broke into pieces when the ETMT samples were cut from the sample and there are therefore no mechanical properties results.

5.7. Characterization of Ti-46Al-8Hf

5.7.1. Microstructure

Nb was completely replaced by Hf in the Ti-46Al-8Hf sample. The Hf wire melted more easily than the Nb wire, and no Hf-rich particles were observed in the sample. Figure 5.34-b shows the microstructure of Ti-46Al-8Hf before HIP. The matrix has a lamellar microstructure. Moreover, there is some light dendrite phase in the matrix. Some tiny Hf precipitates and even some pores with diameters of 2-3 µm are dispersed around the light dendrite phase. After HIP, the Hf precipitates, the pores disappear, and the light dendrite phase has diffused into the matrix. The diffusion is not quite complete and a blurry dendritic phase became can still be observed in Figure 5.34-a. These areas have a composition of 47.17 at.% Al, 48.06 at.% Ti and 4.77 at.% Hf, while the matrix has a composition of 44.36 at.% Al, 52.24 at.% Ti and 3.41 at.% Hf.

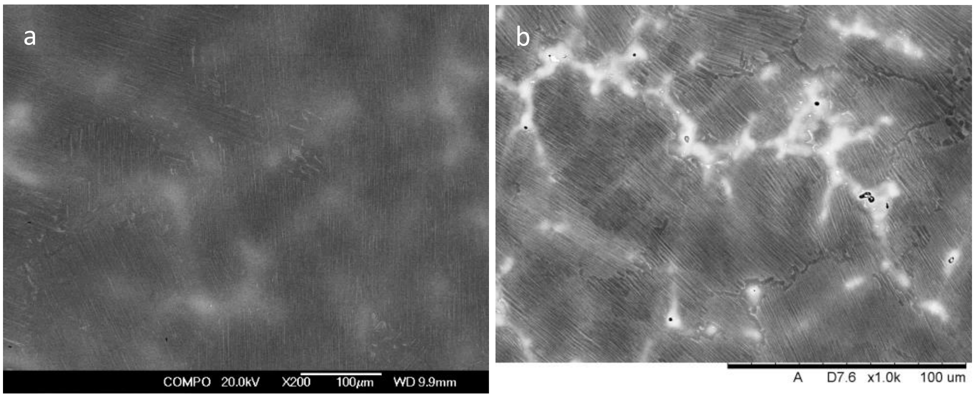

Figure 5.34 Back-scattered images of Ti-46Al-8Hf, a is after HIP and b is before HIP.

At the edge of Ti-46Al-8Hf sample, there are lots of Hf oxides (HfO) as shown in Figure 5.35. Some of these oxides are round, and some of them are needlelike. The size of the oxides is 2-10 µm.

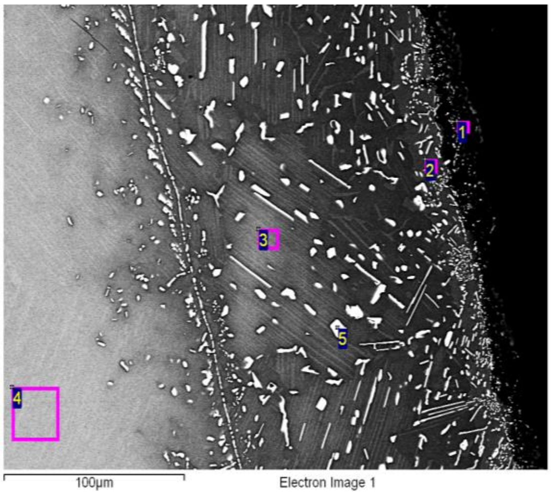

Figure 5.35 Back-scattered images of Ti-46Al-8Hf showing the edge of the sample

5.7.2. Phases

According to the XRD results of Ti-46Al-8Hf as shown in Figure 5.36, there are two phases in Ti-46Al-8Hf: α_2 and γ.

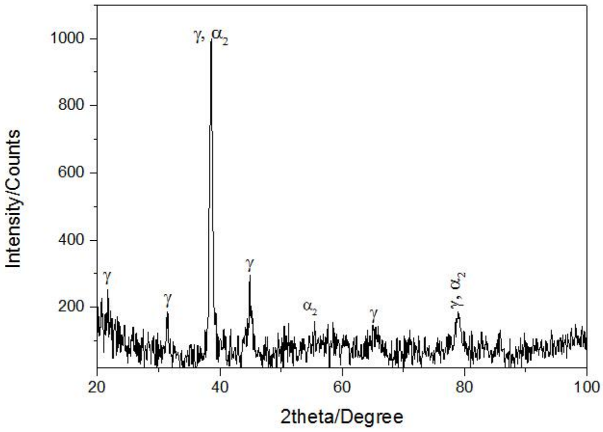

Figure 5.36 Transmission X-ray diffraction patterns of Ti-46Al-8Hf

5.7.3. Mechanical properties

Ti-46Al-8Hf-1 and Ti-46Al-8Hf-2 are two HIPped ETMT samples cut from the Ti-46Al-8Hf sample. The tensile stress-strain curves are similar for the two samples (see in Figure 5.37). Ti-46Al-8Hf-2 has a higher UTS of 320.5 MPa than Ti-46Al-8Hf-1. Their ductilities are close to each other. The tensile properties of two Ti-46Al-8Hf samples are listed in Table 5.10.

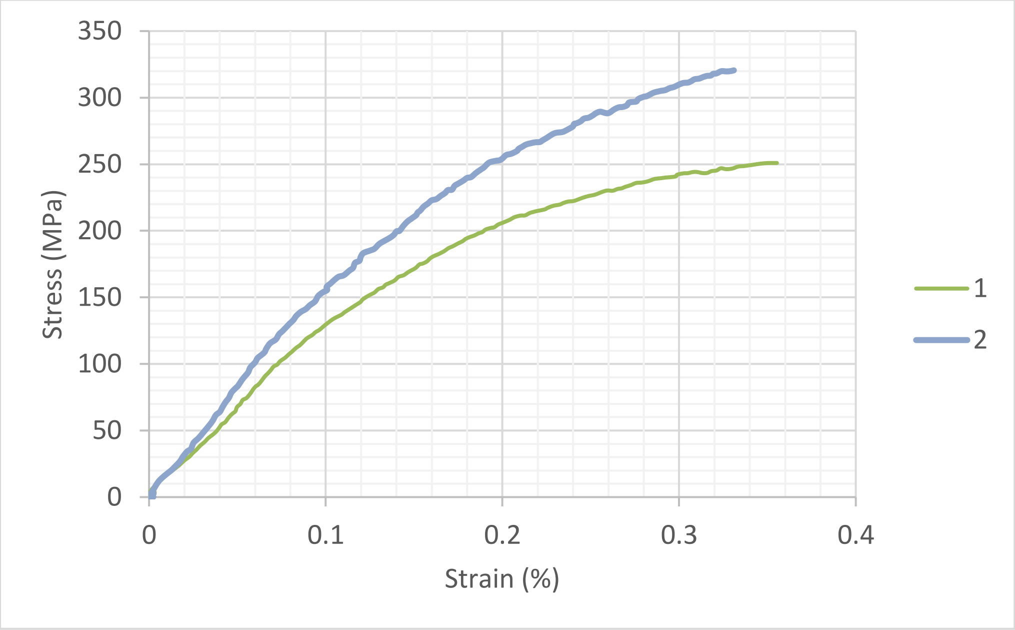

Figure 5.37 The tensile stress-strain curves of Ti-46Al-8Hf

Table 5.10 The tensile properties of two Ti-46Al-8Hf ETMT samples

Sample	**0.2% proof stress (MPa)**	**UTS (MPa)**	**Ductility (%)**
Ti-46Al-8Hf-1	207.1	250.9	0.35
Ti-46Al-8Hf-2	256.9	320.5	0.33

These two ETMT samples have no macro-segregations in their fracture surface and both seem homogeneous (as Figure 5.38 shows). Small but plentiful cleavage planes due to the lamellar microstructure can be observed on the fracture surfaces of both Ti-46Al-8Hf-1 and 2.

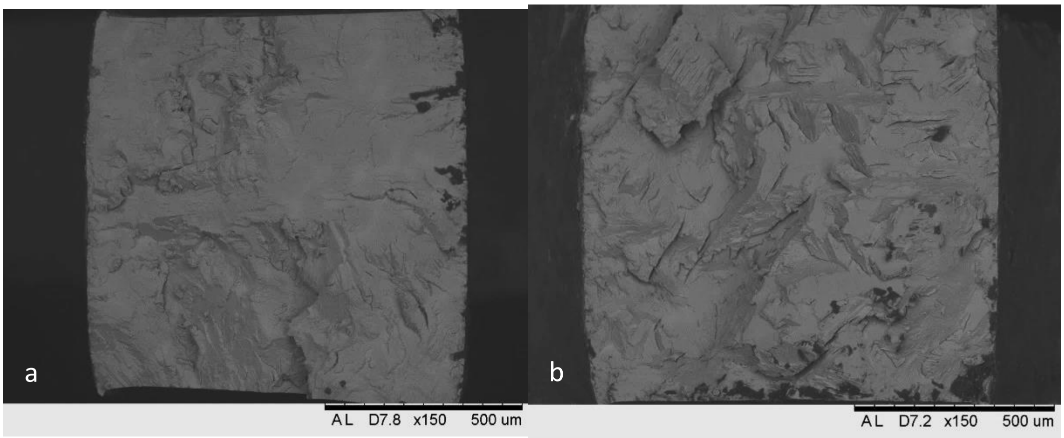

Figure 5.38 Back-scattered images of the fracture surfaces of a) Ti-46Al-8Hf-1 and b) Ti-46Al-8Hf-2 ETMT sample

5.8. Characterization of Ti-46Al-4Nb-4Hf

5.8.1. Microstructure

When Hf replaces half of Nb, the Nb-rich particles are again observed. The Ti-46Al-4Nb-4Hf sample is shown in Figure 5.39. According to the EDX results, there is no Hf in the Nb-rich balls. The larger ball is pure Nb. The smaller Nb-rich ball has a composition of 23.7 at.% Al, 21.81 at.% Ti and 54.48 at.% Nb.

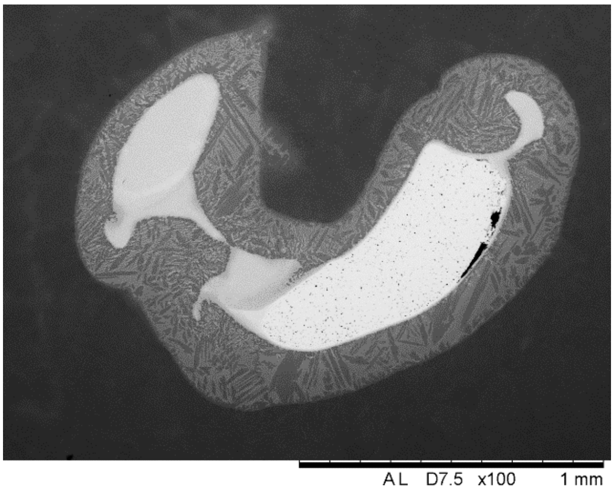

Figure 5.39 Back-scattered image of Ti-46Al-4Nb-4Hf showing Nb-rich balls

At the edge of Ti-46Al-4Nb-4Hf sample (see in Figure 5.40), there is no oxidized layer like other Ti-Al-Nb-X samples, and it only has several Hf oxides particles gathered at the edge. The amount of HfO particles in Ti-46Al-4Nb-4Hf are less than HfO particles in Ti-46Al-8Hf, since it only has half of Hf content. The matrix close to the edge only has 0.82 at.% Hf in it. Almost all the Hf has been oxidized and appeared as HfO oxides.

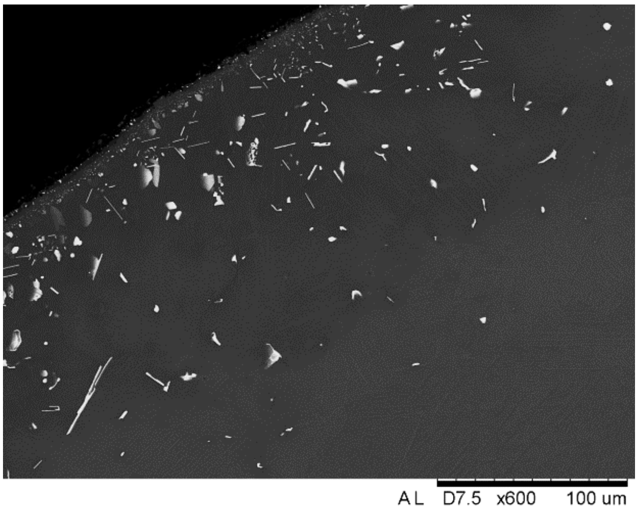

Figure 5.40 Back-scattered image of Ti-46Al-4Nb-4Hf showing the edge of the sample

In the matrix of Ti-46Al-4Nb-4Hf the diffused light phase after HIP can also be observed as it was in Ti-46Al-8Hf. The spacing of lamellar microstructure in Ti-46Al-4Nb-4Hf is about 5 µm which is wider than other Ti-Al-Nb-X samples.

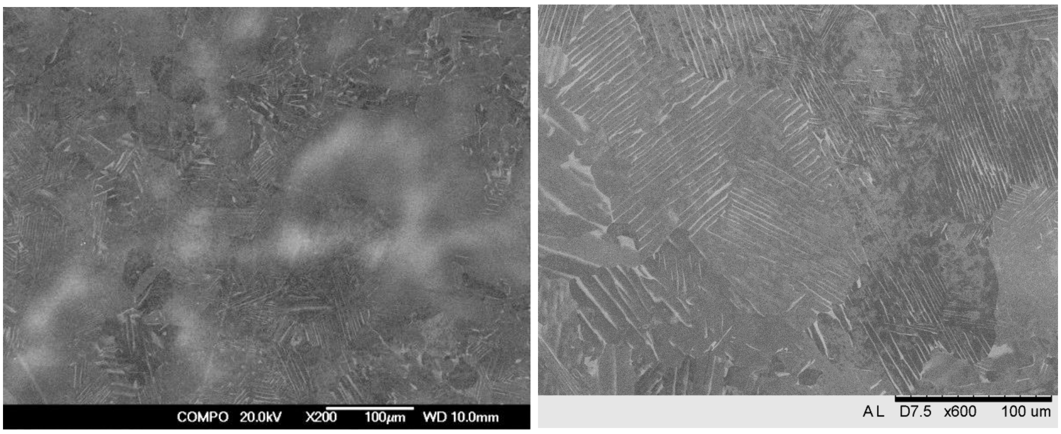

Figure 5.41 Back-scattered images of Ti-46Al-4Nb-4Hf showing the matrix of the sample

5.8.2. Phases

Ti-46Al-4Nb-4Hf's transmission X-ray diffraction patterns look almost the same as Ti-46Al-8Hf's. They all have the same peaks from α_2 and γ phases as labeled in Figure 5.36 and 5.42.

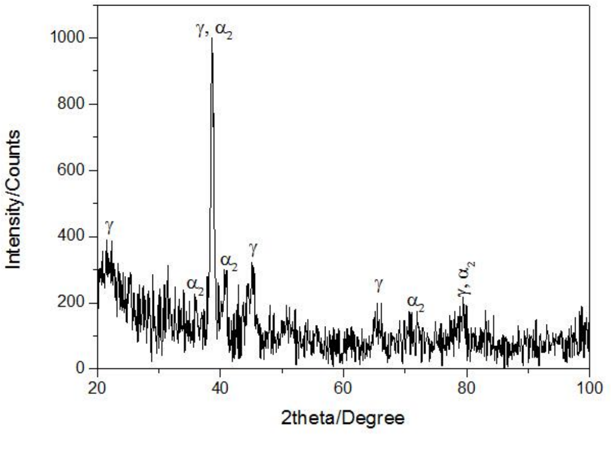

Figure 5.42 Transmission X-ray diffraction patterns of Ti-46Al-4Nb-4Hf

5.8.3. Mechanical properties

Figure 5.43 shows the tensile stress-strain curves from the two Ti-46Al-4Nb-4Hf ETMT samples. The behaviors of these two samples are similar. Their UTS are 275.0 MPa and 230.7 MPa respectively, and their ductility is only about 0.14 (listed in Table 5.11).

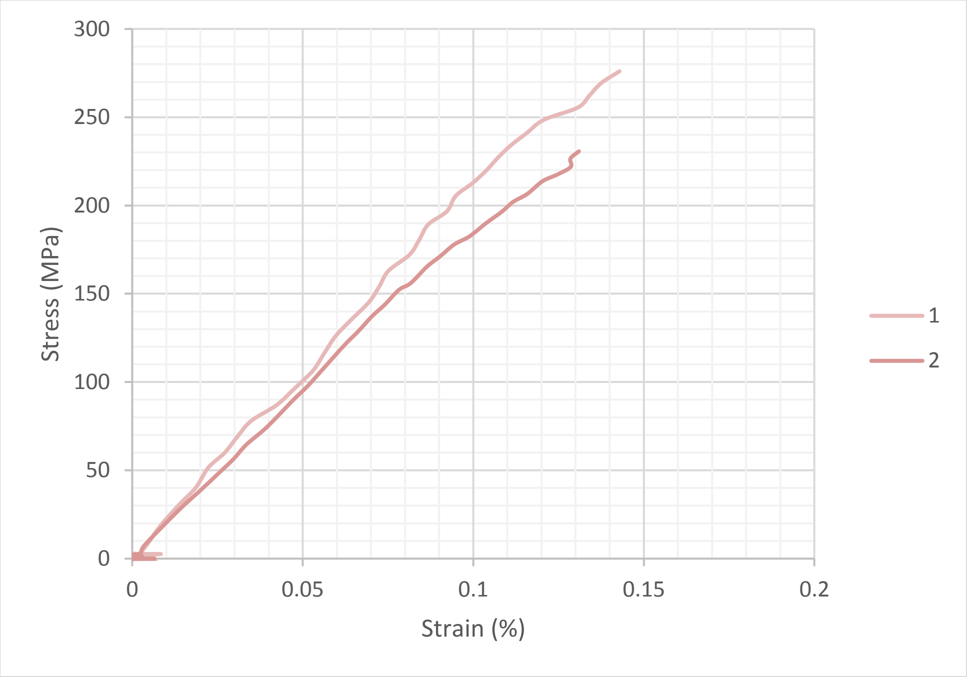

Figure 5.43 The tensile stress-strain curves of Ti-46Al-4Nb-4Hf

Table 5.11 The tensile properties of two Ti-46Al-4Nb-4Hf ETMT samples

Sample	UTS (MPa)	Ductility (%)
Ti-46Al-4Nb-4Hf-1	275.0	0.14
Ti-46Al-4Nb-4Hf-2	230.7	0.13

One of Ti-46Al-4Nb-4 sample, Ti-46Al-4Nb-4-1's fracture surface is shown in Figure 5.44. There are no macro-segregations in the ETMT sample, and the typical cleavage planes introduced by lamellar microstructure can be seen like other Ti-Al-Nb-X samples.

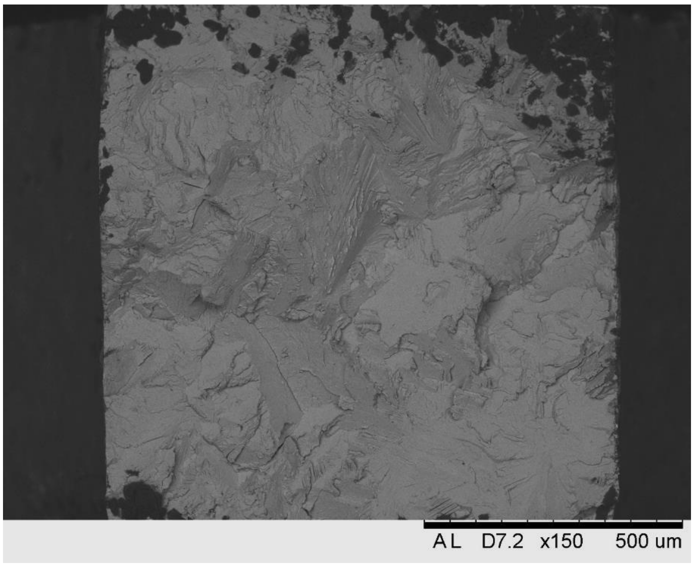

Figure 5.44 Back-scattered image of Ti-46Al-4Nb-4Hf's fracture surface

5.9. Discussion

5.9.1. Comparison of Cast and SDA Ti-46Al-8Nb

Wu has summarized that there are three typical microstructures in TiAl based alloys: fully lamellar, duplex and near fully lamellar (Wu 2006). The cast Ti-46Al-8Nb in this research has a near fully lamellar microstructure which was determined by the heat treatment process (HIPped at 1280 ^{0}C and 150 MPa for 4 hours). There are some massive γ grains among the lamellar in the as-casted Ti-46Al-8Nb. As for SDA Ti-46Al-8Nb, the most significant difference compared to cast sample is the presence of Nb-rich particles. Though SDA has been successfully developed to produce many complex alloys samples it has not been found to melt Nb well and many of the samples produced in the work have been contaminated with pure Nb or Nb rich particles. After HIP processing, the Nb-rich particle in the SDA Ti-46Al-8Nb sample had started to dissolve but is far from homogeneous. Moreover, some Ti segregation was observed after HIP processing. Despite this segregation, the matrix of SDA Ti-46Al-8Nb actually has a fully lamellar microstructure without any γ grains. The matrix of SDA Ti-46Al-8Nb has a close composition to the cast Ti-46Al-8Nb with only a difference of 1-2 at.% (as shown in Table 5.12).

Table 5.12 Chemical composition comparison between as-casted Ti-46Al-8Nb and SDA Ti-46Al-8Nb

Sample	Al (at.%)	Ti (at.%)	Nb (at.%)
As-casted Ti-46Al-8Nb	43.062	49.21	7.726
SDA Ti-46Al-8Nb	43.29	47.92	8.79

It is know that a fully lamellar microstructure is the microstructure expected to provide TiAl alloys with good properties such as high strength, high creep resistance and high fracture toughness (Chan and Kim 1995, Liu, Schneibel et al. 1996, Kim 1998). The lamellar structure’s features like colony size and lamellar spacing can all have an important impact on the material especially mechanical properties. By refining the lamellar colony size, the disadvantage introduced by lamellar structure, the low ductility at room temperature can be improved (Liu and Maziasz 1998, Hu 2002). The lamellar colony sizes of cast Ti-46Al-8Nb and SDA Ti-46Al-8Nb are basically the same, 200-

300 µm, and their lamellar spacing are also similar as 1-2 µm. Therefore, the mechanical properties of as-casted Ti-46Al-8Nb and SDA Ti-46Al-8Nb have no large differences.

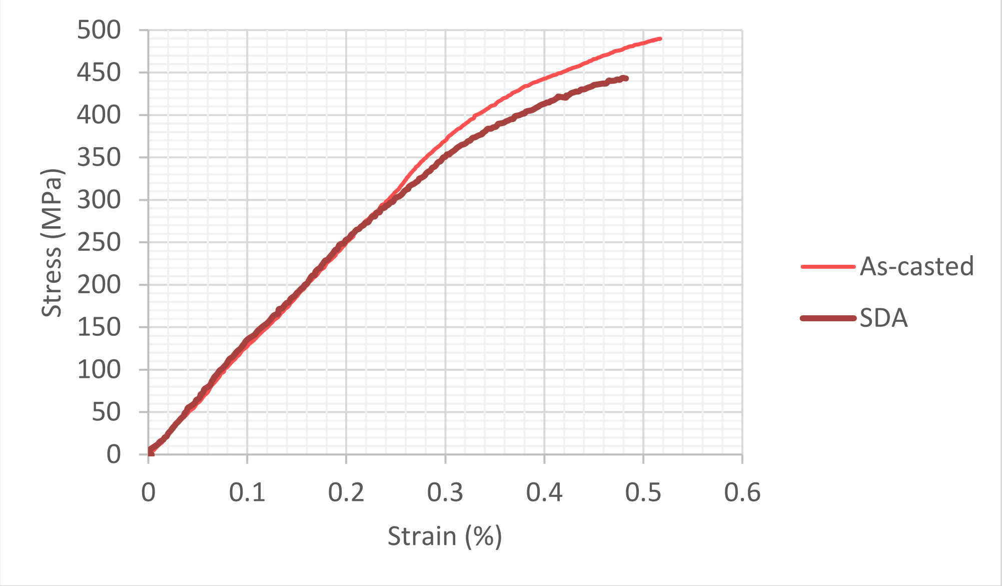

Figure 5.45 Comparison of the tensile stress-strain curves of as-casted Ti-46Al-8Nb and SDA Ti-46Al-8Nb

5.9.2. Influence of HIP on Ti-46Al-Nb-X samples

HIP is a process that can close cavities in the material and homogenizing the microstructure at the same time. In this study, the heat treatment that HIPped at 1280 ^{0}C and 150 MPa for 4 hours was performed on Ti-46Al-X-Y samples (including Ti-46Al-8Nb and Ti-46Al-8Hf).

However the HIP process was not found to improve samples with Nb-rich particles. The Nb-rich particles started to be dissolve but consequently became large Nb-rich balls, which are not desired. HIP was also found to oxidise the samples at the surface. Many Ti-46Al-Nb-X samples like Ti-46Al-8Nb, Ti-46Al-4Nb-4V and so on have diffusion layers at the surfaces of the samples. However, it is acceptable because the oxidized layers are only 50-200 µm thick and have not effected the inside microstructure except for addition of Hf. Ti-46Al-8Hf and Ti-46Al-4Nb-4Hf have Hf oxides precipitated at the edge of the samples. The number of HfO particles increased with the Hf content and leads to the low Hf content in the matrix of the samples. For some samples like Ti-46Al-4Nb-4Zr, the HIP process in this study was not enough to close the cracks in it. However, for Ti-46Al-4Nb-4Hf, not only could HIP close the pores but it also dissolved the Hf precipitates.

The lamellar structure in SDA Ti-46Al-8Nb did not change much after HIP in terms of lamellar colony size and lamellar spacing. SDA Ti-46Al-8Nb was solidified at a relatively slow cooling rate, because the laser beam continuously provides energy into the melting pool on the top of the sample during solidification. Therefore, the as-build SDA sample has a similar microstructure compared to the cast/HIPped sample. Directionally solidified Ti-46Al-8Nb in Liu’s research had a dendritic structure.(Liu, Xin-Zhong et al. 2012)

5.9.3. Effect of fourth element addition in Ti-46Al-8Nb

It is well known that lamellar microstructure is important to the performances of the TiAl gamma alloys, and additions like B and C can refine the lamellar structure and increase the material’s ductility accordingly (Hu 2002). Cr addition like Ti-47Al-2Nb-Cr and Mn addition like Ti-48Al-2Nb-2Mn are widely studied (Crofts, Bowen et al. 1996, Hénaff, Bittar et al. 1996, Liu, Schneibel et al. 1996, Liu and Maziasz 1998, Zghal, Thomas et al. 2005). In this chapter, V, Zr, Co and Hf were studied as the fourth element based on Ti-46Al-8Nb.

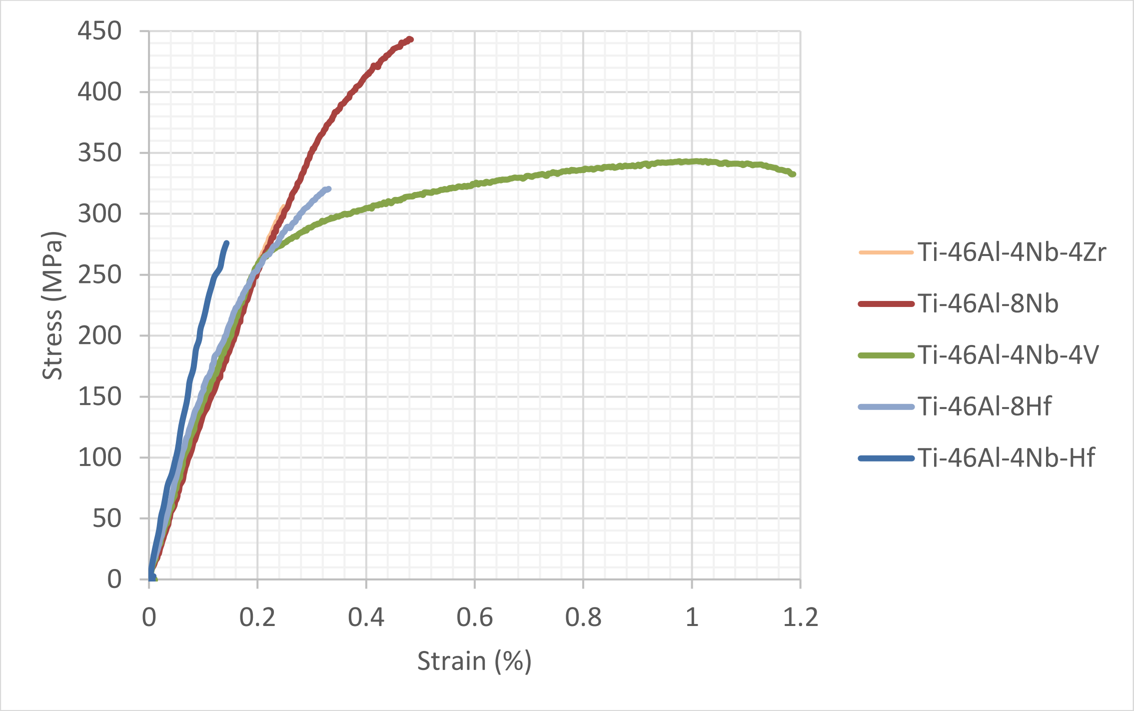

Figure 5.46 Comparison of the tensile stress-strain curves of Ti-Al-Nb-X samples

Addition of Co make the Ti-46Al-4Nb-4Co with little lamellar structure in it, and instead intermetallic phase dispersed in the sample made the sample quite brittle. This material was too brittle to make ETMT samples, thus it has no tensile test results. According to Figure 5.46, Ti-46Al-8Nb has the highest UTS of 454.8 MPa. The addition of V lowered the strength but increased the ductility significantly from 0.52 to 1.18, because the addition of V has refined the lamellar microstructure. The lamellar in Figure 5.15 has a smaller spacing than in Ti-46Al-8Nb as Figure 5.9 shows. The lamellar colony size of Ti-46Al-4Nb-4V may get larger, but at the boundary of each large lamellar colony there are many small lamellar colonies with a size of 200 μm. Ti-46Al-4Nb-4Zr's curve is overlapped by other curves in the figure, and it has a low tensile strength and a low ductility compared to Ti-46Al-8Nb. According to Figure 5.24, Zr's addition also made the lamellar spacing as small as 1 μm, however the lamellar colonies were enlarged. The larger lamellar colonies lead to lower strength and ductility. (Kim 1998) Moreover, there were some small cracks in Ti-46Al-4Nb-4Zr which made the strength and ductility even lower. The addition of Hf, on the contrary, it can refine the lamellar colonies, but enlarge the lamellar spacing. In Figure 5.41, the lamellar colonies of Ti-46Al-4Nb-4Hf is about 100 μm which is much smaller than other Ti-Al-Nb-X samples, and its lamellar spacing is about 5 μm compared to other sample's lamellar spacing with 1 μm. Therefore, although Ti-46Al-4Nb-4Hf has a better performance than Ti-46Al-4Nb-4Zr, it is still not good enough compared to Ti-46Al-8Nb.

According to the oxidized layer of each Ti-Al-Nb-X sample (listed in Table 5.13), the influence of the fourth element on material's oxidation resistance can be indicated. Nb and V have a good oxidation resistance, while Co and Hf will decrease the oxidation resistance.

Table 5.13 The oxidized layer's thickness of Ti-Al-Nb-X samples

	Ti-46Al-8Nb	Ti-46Al-4Nb-4V	Ti-46Al-4Nb-4Zr	Ti-46Al-4Nb-4Co	Ti-46Al-8Hf	Ti-46Al-4Nb-4Hf
oxidized layer's thickness* (μm)	50	50	70	180	200	150

*: All the oxidized layers' thicknesses are estimated roughly according to their back-scattered images.

5.10. Summary

- SDA Ti-46Al-8Nb sample has been produced with a composition close to the target. Despite some Nb-rich particles, SDA Ti-46Al-8Nb also has a similar microstructure compared to cast Ti-46Al-8Nb sample, especially the matrix. The mechanical performance of SDA Ti-46Al-8Nb sample and cast Ti-46Al-8Nb sample are similar.
- HIP does not dissolve the Nb-rich particles in Ti-46Al-8Nb, and enlarges the inhomogeneous area through diffusion. HIPped at 1280 ^{0}C and 150 MPa for 4 hours has a small effect on homogenizing the microstructure of Ti-Al-Nb-X samples and does remove some of defects, however it is not as useful as expected, and the influence is limited.
- The addition of V in Ti-46Al-8Nb alloys can make the material more ductile. It is quite a potent element for improving Ti-Al-Nb alloys' ductility.
- The addition of Co changes Ti-46Al-8Nb alloy's microstructure completely. The typical lamellar structure is gone and replaced by brittle intermetallic phase.
- The addition of Zr and Hf does not improve Ti-46Al-8Nb's mechanical properties, although a finer lamellar microstructure is produced
- Nb and V can provide TiAl alloys with a good oxidation resistance, while Co and Hf decrease the oxidation resistance.
- SDA shows some promise for the development of improved Ti-Al alloys. However Nb is not alloyed by the process perfectly leading to samples contaminated with Nb and Nb-rich particles.

5.11. References

Chan, K. S. and Y. W. Kim (1995). "Effects of lamellae spacing and colony size on the fracture resistance of a fully-lamellar TiAl alloy." Acta Metallurgica Et Materialia **43**(2): 439-451.

Crofts, P. D., et al. (1996). "The effect of lamella thickness on the creep behaviour of Ti-48Al-2Nb-2Mn." Scripta Materialia **35**(12): 1391-1396.

Hénaff, G., et al. (1996). "Fatigue crack propagation resistance of a Ti 48Al 2Mn 2Nb alloy in the as-cast condition." Materials Science & Engineering A **219**(1): 212-220.

Hu, D. (2002). "Effect of boron addition on tensile ductility in lamellar TiAl alloys." Intermetallics **10**(9): 851-858.

Hu, D., et al. (2005). "Advances in optimisation of mechanical properties in cast TiAl alloys." Intermetallics **13**(13): 914-919.

Huang, A., et al. (2007). "The influence of pressure on solid-state transformations in Ti–46Al–8Nb." Scripta Materialia **56**(4): 253-256.

Huang, A., et al. (2007). "The influence of pressure on solid-state transformations in Ti–46Al–8Nb." Scripta Materialia **56**(4): 253-256.

Kim, Y. W. (1998). "Strength and ductility in TiAl alloys." Intermetallics **6**(7–8): 623-628.

Liu, C. T. and P. J. Maziasz (1998). "Microstructural control and mechanical properties of dual-phase TiAl alloys." Intermetallics **6**(7): 653-661.

Liu, C. T., et al. (1996). "Tensile properties and fracture toughness of TiAl alloys with controlled microstructures." Intermetallics **4**(6): 429-440.

Liu, G. H., et al. (2012). "Microstructure and microsegregation in directionally solidified Ti–46Al–8Nb alloy." Transactions of Nonferrous Metals Society of China **22**(6): 1342–1349.

Wu, X. (2006). "Review of alloy and process development of TiAl alloys." Intermetallics **14**(10–11): 1114-1122.

Zghal, S., et al. (2005). "Phase transformations in TiAl based alloys." Acta Materialia **53**(9): 2653-2664.

CHAPTER 6: CONCLUSIONS AND FUTURE WORKS

This chapter summarises the main conclusions in Chapter 4 and 5, including the performance of SDA synthesis and the optimization of SDA process, moreover, the influence of the fourth element on Ti-Al-Nb alloys using SDA technique. The suggestions for future research work are also presented.

6.1. Overall Conclusions and summaries

Chapter 4 shows the homogeneity of Ti-Al-V, Ti-Al-Fe and Ti-Al-Nb ternary alloy systems and optimization of the Suspended Droplet Alloying (SDA) process parameters based on Ti-46Al-8Nb. It shows that SDA is a promising method for alloy exploration. SDA is a combinatorial synthesis method based on Direct Laser Melting. It can produce a bulk specimen with a specific composition in just a few minutes. Like Ti-Al-V and Ti-Al-Fe, many samples have been made successfully in these two ternary alloy systems. There are other more than 1000 alloy samples with different compositions have been recorded as homogeneous SDA samples in the Virtual Alloy Library. All these AccMet samples and their corresponding properties like hardness, power factor, phases and so on are recorded in the Virtual Alloy Library.

Ti-Al-Nb ternary samples are more difficult to make than Ti-Al-V or Ti-Al-Fe samples using SDA. Because Nb’s melting point is as high as Al’s boiling point, and the mixing of three wire is not as smoothly as other Ti-Al-X ternary systems. In the SDA Ti-Al-Nb samples, the inhomogeneous samples are mainly failed because of unmelted Nb particles, and a few of them are failed due to the chemical variation across the whole sample.

The unmelted Nb particles are coming from the Nb wire's tail end that protrude out of the suspended alloyed droplet during the formation of the droplet. High speed photography of the Ti-Al-Nb SDA process captured the Nb particles which were exposed outside the suspended droplet deposited into the melting pool directly. The melting pool didn't have enough energy to melt these Nb particles, so they remained in the samples after solidification. The Nb particles usually form under two situations. First one is the Nb wire feed rate is too high, then the Nb wire would protrude out of the droplet before it gets melted completely in the droplet. The second situation is the intermittent contact of the low melting Al wire can drag the alloyed droplet towards the Al wire as it touches, leading to the exposure of Nb wire outside the alloyed droplet. Actually the Ti wire will be exposed as well, however Ti particles can be well melted in the melting pool, and no Ti particles have been observed in Ti-Al-Nb samples. In order to solve this problem, laser power need to be increased and the Nb feed rate need to slow down.

Another kind of inhomogeneity is the chemical variation across the whole sample. It is because the droplets cannot be produced exactly the same. Due to different feed pattern and different wire feed behaviour, the droplets may have a slight compositional difference between each other. And if the compositional difference was too big and the deposition place was moved a bit, the chemical variation will be shown in the final SDA samples. In fact, with proper process parameters, the compositional consistency of sequential Ti-Al-Nb droplets was found to be quite good. The Nb content was stable, and the Ti and Al content were generally constant with a few chemical variations within

3 at. % compared to the target composition. A standard SDA sample is actually the result of overlapping of deposited droplets. Therefore, in production of a SDA sample the small variations would be further reduced and even eliminated as several neighboring droplets would be further mixed together in the melting pool.

To make a homogeneous SDA sample, a correspondent suitable wire size, feed position, feed rate and laser power are needed for different chemical formulations. Different wire sizes not only have a significant influence on the wire feed rate, but also change the melting pattern and the reaction with the alloyed droplet. A good feed position is needed to make the wires hold the droplet in the middle and take all the wires smoothly. Otherwise, some wires may melt and deposit alone on one side. The relationship between laser power and wire feed rate is the key to the process. The laser power can’t be too small and the wire feed rate can’t be too fast so that wires can get enough energy to be melted. On the other side, the laser power can’t be too high and the wire feed rate can’t be too slow, otherwise the melting pool will be overheated. So the laser power and the wire feed rate should achieve a balance to provide a fit energy to melt the materials without causing any overheat. With a suitable selection of these process parameters homogeneous samples can generally be produced. For Ti-Al-Nb samples, it can achieve the maximum homogeneity with the optimized process parameters.

For some combinatorial investigations the adjusted method can save further time and materials, so another type of AccMet sample is developed as splats. By allowing a single alloyed droplet to impact on a thick copper chill a splat with target composition can be produced. The Ti-46Al-8Nb splat was made in this way and had been checked to have the target composition and a homogeneous microstructure. According to the simulation of splats by Simdrop, the splats will be flatter on the top surface if the impact speed is high. Moreover, the splat simulations indicated that a higher droplet temperature (or a lower substrate temperature) will allow the production of splats which are flatter.

Chapter 5 presents the characterizations of as-casted Ti-46Al-8Nb, SDA Ti-46Al-8Nb, SDA Ti-46Al-4Nb-4V, SDA Ti-46Al-4Nb-4Co, SDA Ti-46Al-4Nb-4Zr, SDA Ti-46Al-4Nb-4Hf and SDA Ti-46Al-8Hf in terms of microstructure and mechanical properties.

Some SDA samples still have some Nb-rich particles in it but with a small amount after the improvement of the process in the previous chapter. The matrix can still provide enough space to investigate and cut the tensile samples out of it.

SDA Ti-46Al-8Nb also has a similar microstructure and mechanical properties compared to cast Ti-46Al-8Nb sample. It means SDA can produce samples that is comparable with as-casted ones but with much shorter time.

The influences of different the forth element based on Ti-46Al-8Nb have been explored. The addition of V in Ti-46Al-8Nb alloys can make the material more ductile. It is quite a potential element to improve Ti-Al-Nb alloys' ductility. The addition of Co changes Ti-46Al-8Nb alloy's microstructure completely. The typical lamellar structure is gone and replaced by brittle intermetallic phase. The addition of Zr and Hf does not improve Ti-46Al-8Nb's mechanical properties, although a finer lamellar microstructure is produced. Moreover, Nb and V can provide TiAl alloys with a good oxidation resistance, while Co and Hf decrease the oxidation resistance.

6.2. Proposed future works

6.2.1. SDA development

The laser source in the SDA system is Triagon CO_2 laser at the moment, and its maximum laser power is 1972 W. Because of the limitation of the absorption of the CO_2 wavelength and the limited laser power, many high temperature wires cannot be melted by the laser, such as Mo, W and Ta. The metal wires stock that is available in the project has: Ti, Al, Fe, V, Nb, Zr, Co, Ni, Cu, Hf, Sn, W, Mo, Ta. There are about 100 alloy systems have been tried so far. With the upgrade of the laser source and the expansion of wire stock, more and more interesting alloy formulations can be investigated using SDA.

6.2.2. Exploration of Ti-Al-Nb alloys

In Chapter 6 it is shown that the addition of V can increase the ductility of Ti-46Al-8Nb. The amount of the V's additions could be further investigated in order to achieve the Ti-Al-Nb-V alloy formulations with balanced and improved properties. Moreover, the effect of other fourth elements, an even fifth element can be investigated in Ti-Al-Nb alloys using SDA technique.

6.2.3. Utilization of AccMet database

Although the AccMet project has now ended, the “Virtual Alloy library” has more than 1000 alloy samples and measured properties in it. Based on the AccMet database, some promising alloy formulations will be further tested, patented and exploited.